

# Fundamental limits on the rate of bacterial cell division

<sup>3</sup> Nathan M. Belliveau<sup>†, 1</sup>, Griffin Chure<sup>†, 2</sup>, Christina L. Hueschen<sup>3</sup>, Hernan G. Garcia<sup>4</sup>, Jane Kondev<sup>5</sup>, Daniel S. Fisher<sup>6</sup>, Julie A. Theriot<sup>1, 7, \*</sup>, Rob Phillips<sup>8, 9, \*</sup>

<sup>5</sup> <sup>1</sup>Department of Biology, University of Washington, Seattle, WA, USA; <sup>2</sup>Department of Applied Physics, California Institute of Technology, Pasadena, CA, USA; <sup>3</sup>Department of Chemical Engineering, Stanford University, Stanford, CA, USA; <sup>4</sup>Department of Molecular Cell Biology and Department of Physics, University of California Berkeley, Berkeley, CA, USA; <sup>5</sup>Department of Physics, Brandeis University, Waltham, MA, USA; <sup>6</sup>Department of Applied Physics, Stanford University, Stanford, CA, USA; <sup>7</sup>Allen Institute for Cell Science, Seattle, WA, USA; <sup>8</sup>Division of Biology and Biological Engineering, California Institute of Technology, Pasadena, CA, USA; <sup>9</sup>Department of Physics, California Institute of Technology, Pasadena, CA, USA; \*Co-corresponding authors. Address correspondence to phillips@pboc.caltech.edu and jtheriot@uw.edu; <sup>†</sup>These authors contributed equally to this work

14

---

<sup>15</sup> **Abstract** Recent years have seen a deluge of experiments dissecting the relationship between bacterial growth rate, cell size, and protein content, quantifying the abundance of proteins across growth conditions with unprecedented resolution. However, we still lack a rigorous understanding of what sets the scale of these quantities and when protein abundances should (or should not) depend on growth rate. Here, we seek to quantitatively understand this relationship across a collection of *Escherichia coli* proteomic data sets covering  $\approx$  4000 proteins and 36 growth rates. We estimate the basic requirements for steady-state growth by considering key processes in nutrient transport, energy generation, cell envelope biogenesis, and the central dogma. From these estimates, ribosome biogenesis emerges as a primary determinant of growth rate. We expand on this assessment by exploring a model of ribosomal regulation as a function of the nutrient supply, revealing a mechanism that ties cell size and growth rate to ribosomal content.

25

---

## 26 Introduction

27 The observed range of bacterial growth rates is enormously diverse. In natural environments, some microbial organisms may double only once per year (*Mikucki et al., 2009*) while in comfortable laboratory conditions, growth 28 can be rapid with several divisions per hour (*Schaechter et al., 1958*). This six order-of-magnitude difference in 29 time scales encompasses different microbial species and lifestyles, yet even for a single species such as *Escherichia* 30 *coli*, the growth rate can be modulated over a comparably large scale by tuning the type and amount of nutrients 31 in the growth medium. This remarkable flexibility in growth rate illustrates the intimate relationship between 32 environmental conditions and the rates at which cells convert nutrients into new cellular material – a relationship 33 that has remained a major topic of inquiry in bacterial physiology for over a century (*Jun et al., 2018*).

35 Jacques Monod once remarked that “the study of the growth of bacterial cultures does not constitute a specialized 36 subject or branch of research, it is the basic method of Microbiology.” Those words ring as true today as 37 they did when they were written 70 years ago (*Monod, 1949*) with the quantitative power of this “method” recently 38 undergoing renaissance. Many of the key questions addressed by the pioneering efforts in the middle of the last 39 century can be revisited by examining them through the lens of the increasingly refined molecular census that is 40 available for bacteria such as the microbial workhorse *E. coli*.

41 Several of the evergreen questions about bacterial growth and physiology that were originally raised by micro-

42 biologists in the middle of the 20th century can now be reframed in light of this newly available data. For example,  
43 what biological processes are the primary determinants for how quickly bacterial cells can grow and reproduce?  
44 How do cells modulate the absolute numbers and relative ratios of their molecular constituents as a function of  
45 changes in growth rate or nutrient availability? In this paper, we begin by considering these two questions from  
46 two distinct angles. First, as a result of an array of high-quality proteome-wide measurements of *E. coli* under  
47 diverse growth conditions, we have a census that allows us to explore how the number of key molecular players  
48 change as a function of growth rate. Here, we have assembled a singular data set using measurements collected  
49 over the past decade via mass spectrometry (*Schmidt et al., 2016; Peebo et al., 2015; Valgepea et al., 2013*) or  
50 ribosomal profiling (*Li et al., 2014*) of the composition of the *E. coli* proteome across 36 unique growth rates (see  
51 Appendix Experimental Details Behind Proteomic Data for further discussion of the data). Second, by compiling  
52 molecular turnover rate measurements for many of the fundamental processes associated with bacterial growth,  
53 we make quantitative estimates of key cellular processes (schematized in *Figure 1*) to determine whether our cur-  
54 rent understanding of the dynamics of these processes are sufficient to explain the magnitude of the observed  
55 protein copy numbers across conditions. The census, combined with these estimates, provide a window into the  
56 question of whether the rates of central processes such as energy generation or DNA synthesis are regulated  
57 systematically as a function of cell growth rate by altering protein copy number.

58 Throughout our estimates, we consider an archetypal growth rate of  $\approx 0.5 \text{ hr}^{-1}$  corresponding to a doubling  
59 time of  $\approx 5000$  seconds, as the data sets examined here heavily sample this growth regime. While we formulate  
60 point estimates for the protein abundances at this division time, we also consider how these values will vary  
61 at other growth rates due to changes in cell size, surface area, and chromosome copy number (*Taheri-Araghi*  
62 *et al., 2015*). Broadly, we find that the protein copy numbers appeared tuned for the task of cell doubling across  
63 a continuum of growth rates for the majority of the processes estimated here. Thus, our understanding of the  
64 kinetics of myriad biological processes is sufficient to quantitatively explain the observed abundances of these  
65 proteins.

66 From these estimates, it emerges that translation, particularly the synthesis of ribosomal proteins, is a plausible  
67 candidate that limits the rate of cell division. We reach this conclusion by considering that ribosome synthesis is  
68 1) a rate limiting step for the *fastest* bacterial division, and 2) a major determinant of bacterial growth across  
69 the nutrient conditions we have considered under steady state, exponential growth. This enables us to suggest  
70 that the long-observed correlation between growth rate and cell size (*Schaechter et al., 1958; Si et al., 2017*)  
71 can be simply attributed to the increased absolute number of ribosomes per cell under conditions supporting  
72 extremely rapid growth. To better understand how the observed alterations in absolute protein abundances,  
73 and in particular, changes in ribosome copy number, influence growth rate across different nutrient conditions  
74 we consider a minimal model of cellular growth. Our conclusions from these analyses provide important insight  
75 into how *E. coli* regulates growth across conditions of differing nutrient availability and identifies fundamental  
76 constraints in bacterial growth more broadly.

## 117 Nutrient Transport

118 We begin by considering the critical transport processes diagrammed in *Figure 1(A)*. In order to build new cellular  
119 mass, the molecular and elemental building blocks must be scavenged from the environment in different forms.  
120 Carbon, for example, is acquired via the transport of carbohydrates and sugar alcohols with some carbon sources  
121 receiving preferential treatment in their consumption (*Monod, 1947*). Phosphorus, sulfur, and nitrogen, on the  
122 other hand, are harvested primarily in the forms of inorganic salts, namely phosphate, sulfate, and ammonia  
123 (*Jun et al., 2018; Assentoft et al., 2016; Stasi et al., 2019; Antonenko et al., 1997; Rosenberg et al., 1977; Willsky*  
124 *et al., 1973*). All of these compounds have different membrane permeabilities (*Phillips, 2018*) and most require  
125 some energetic investment either via ATP hydrolysis or through the proton electrochemical gradient to bring the  
126 material across the hydrophobic cell membrane.

127 The elemental composition of *E. coli* has received much quantitative attention over the past half century (*Nei-*  
128 *dhardt et al., 1991; Taymaz-Nikerel et al., 2010; Heldal et al., 1985; Bauer and Ziv, 1976*), providing us with a  
129 starting point for estimating how many atoms of each element must be scavenged from the environment. A syn-  
130 thesis of these studies presents an approximate dry mass composition of  $\approx 50\%$  carbon (BNID: 100649, see *Box 1*),  
131  $\approx 15\%$  nitrogen (BNID: 106666),  $\approx 3\%$  phosphorus (BNID: 100653), and 1% sulfur (BNID: 100655) with remainder

78

## Box 1. The Rules of Engagement for Order-Of-Magnitude Estimates

79

This work relies heavily on "back-of-the-envelope" estimates to understand the growth-rate dependent abundances of molecular complexes. This moniker arises from the limitation that any estimate should be able to fit on the back of a postage envelope. As such, we must draw a set of rules governing our precision and sources of key values.

80

**The rule of "one, few, and ten".** The philosophy behind order-of-magnitude estimates is to provide an estimate of the appropriate scale, not a prediction with many significant digits. We therefore define three different scales of precision in making estimates. The scale of "one" is reserved for values that range between 1 and 2. For example, If a particular process has been experimentally measured to transport 1.87 protons for a process to occur, we approximate this process to require 2 protons per event. The scale of "few" is reserved for values ranging between 3 and 7. For example, we will often use Avogadro's number to compute the number of molecules in a cell given a concentration and a volume. Rather than using Avogadro's number as  $6.02214 \times 10^{23}$ , we will approximate it as  $5 \times 10^{23}$ . Finally, the scale of "ten" is reserved for values which we know within an order of magnitude. If a particular protein complex is present at 883 copies per cell, we say that it is present in approximately  $10^3$  copies per cell. These different scales will be used to arrive at simple estimates that report the expected scale of the observed data. Therefore, the estimates presented here should not be viewed as hard-and-fast predictions of precise copy numbers, but as approximate lower (or upper) bounds for the number of complexes that may be needed to satisfy some cellular requirement.

81

Furthermore, we use equality symbols (=) sparingly and frequently defer to approximation ( $\approx$ ) or scaling ( $\sim$ ) symbols when reporting an estimate. When  $\approx$  is used, we are implicitly stating that we are confident in this estimate within a factor of a few. When a scaling symbol  $\sim$  is used, we are stating that we are confident in our estimate to within an order of magnitude.

82

**The BioNumbers Database as a source for values.** In making our estimates, we often require approximate values for key cellular properties, such as the elemental composition of the cell, the average dry mass, or approximate rates of synthesis. We rely heavily on the BioNumbers Database ([bionumbers.hms.harvard.edu](http://bionumbers.hms.harvard.edu), *Milo et al. (2010)*) as a repository for such information. Every value we draw from this database has an associated BioNumbers ID number, abbreviated as BNID, and we provide this reference in grey-boxes in each figure.

83

**Uncertainty in the data sets and the accuracy of an estimate.** The data sets presented in this work are the products of careful experimentation with the aim to report, to the best of their ability, the absolute copy numbers of proteins in the cell. These data, collected over the span of a few years, come from different labs and use different internal standards, controls, and even techniques (discussed further in Appendix Experimental Details Behind Proteomic Data). As a result, there is notable disagreement in the measured copy numbers for some complexes across data sets. In assessing whether our estimates could explain the observed scales and growth-rate dependencies, we also considered the degree of variation between the different data sets. For example, say a particular estimate undercuts the observed data by an order of magnitude. If all data sets agree within a factor of a few of each other, we revisit our estimate and consider what we may have missed. However, if the data sets themselves disagree by an order of magnitude, we determine that our estimate is appropriate given the variation in the data.

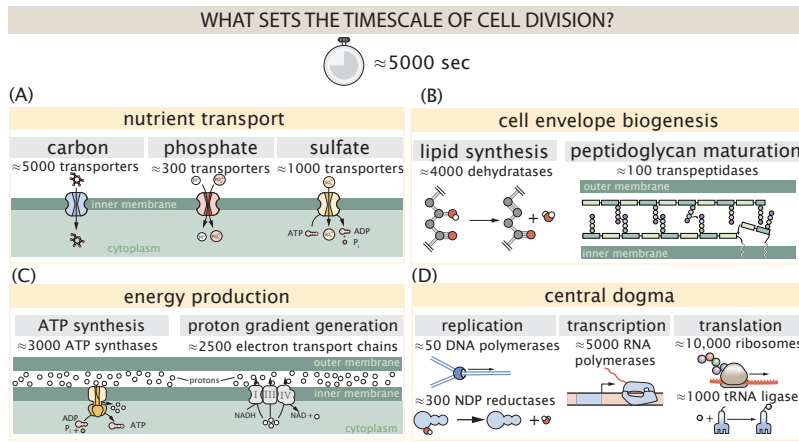


**Figure 1. Transport and synthesis processes necessary for cell division.** We consider an array of processes necessary for a cell to double its molecular components, broadly grouped into four classes. These categories are (A) nutrient transport across the cell membrane, (B) cell envelope biogenesis, (C) energy production (namely, ATP synthesis), and (D) processes associated with the central dogma. Numbers shown are the approximate number of complexes of each type observed at a growth rate of  $0.5 \text{ hr}^{-1}$ , or a cell doubling time of  $\approx 5000 \text{ s}$ .

132 being attributable to oxygen, hydrogen, and various transition metals. We use this stoichiometric breakdown to  
 133 estimate the abundance and growth rate dependence of a variety of transporters responsible for carbon uptake,  
 134 and provide more extensive investigation of the other critical elements – phosphorus, sulfur, and nitrogen – in the  
 135 Appendix ??.

136 Using  $\approx 0.3 \text{ pg}$  as the typical *E. coli* dry mass at a growth rate of  $\approx 0.5 \text{ hr}^{-1}$  (BNID: 103904), coupled with an  
 137 approximation that  $\approx 50\%$  of this mass is carbon, we estimate that  $\sim 10^{10}$  carbon atoms must be brought into  
 138 the cell in order to double all of the carbon-containing molecules (Figure 2(A), top). Typical laboratory growth  
 139 conditions provide carbon as a single class of sugar (such as glucose, galactose, or xylose) often transported cross  
 140 the cell membrane by a transporter complex specific to that particular sugar. One such mechanism of transport  
 141 is via the PTS system which is a highly modular system capable of transporting a diverse range of sugars with  
 142 high specificity (Escalante *et al.*, 2012). The glucose-specific component of this system transports  $\approx 200$  glucose  
 143 molecules ( $\approx 1200$  carbon atoms) per second per transporter (BNID: 114686). Making the assumption that this  
 144 is a typical sugar transport rate for the PTS system, coupled with the need to transport  $\sim 10^{10}$  carbon atoms, we  
 145 then expect on the order of  $\approx 1000$  transporters must be expressed per cell in order to bring in enough carbon  
 146 atoms (Figure 2(A), top).

147 However, we find this estimate to be exceeded by several fold by experimental measurements (Figure 2(A),  
 148 bottom), implying that the cell is capable of transporting more carbon atoms than strictly needed for biosynthesis.  
 149 While we estimate  $\approx 1000$  transporters are needed with a 5000 second division time, we can abstract this  
 150 calculation to consider any particular growth rate given knowledge of the cell density and volume as a function  
 151 of growth rate and direct the reader to the Appendix Extending Estimates to a Continuum of Growth Rates for  
 152 more information. This abstraction, shown as a grey line in Figure 2(A), reveals an excess of transporters even at  
 153 faster growth rates. This contrasts with our observations for uptake of phosphorus and sulfur, which align well  
 154 with our expectations across different growth conditions (Figure 2–Figure Supplement 1 and discussed further in  
 155 Appendix ??).

156 It is important to note, however, that this estimate neglects any specifics of the regulation of the carbon trans-  
 157 port system. Using the diverse array of growth conditions available in the data, we can explore how individual  
 158 carbon transport systems depend on specific carbon availability. In Figure 2(B), we show the total number of  
 159 carbohydrate transporters specific to different carbon sources. A striking observation, shown in the top-left plot  
 160 of Figure 2(B), is the constancy in the expression of the glucose-specific transport systems, an observation that  
 161 stands in contrast with other species of transporters. Additionally, we note that the total number of glucose-  
 162 specific transporters is tightly distributed at  $\approx 10^4$  per cell, the approximate number of transporters needed to  
 163 sustain rapid growth of several divisions per hour. This illustrates that *E. coli* maintains a substantial number of

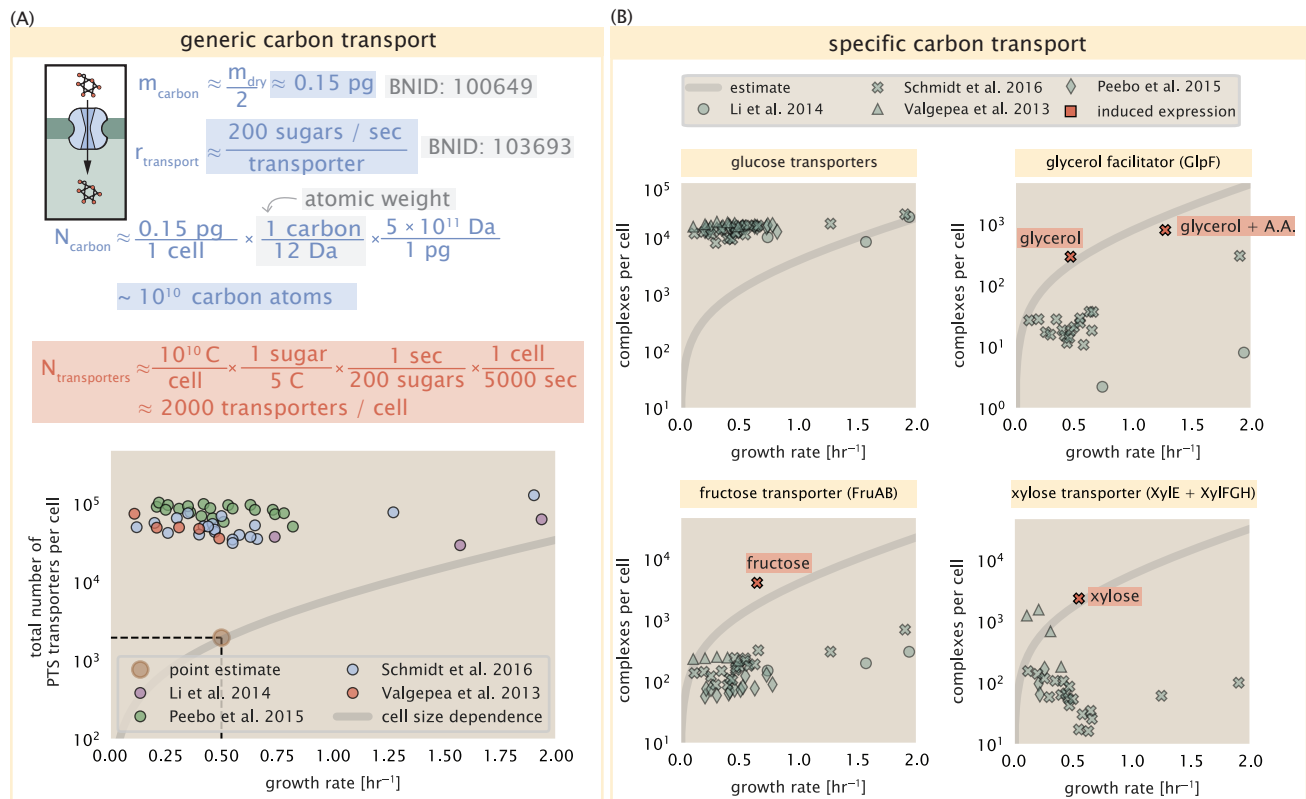


**Figure 2. The abundance of carbon transport systems across growth rates.** (A) A simple estimate for the minimum number of generic carbohydrate transport systems (top) assumes  $\sim 10^{10}$  C are needed to complete division, each transported sugar contains  $\approx 5$  C, and each transporter conducts sugar molecules at a rate of  $\approx 200$  per second. Bottom plot shows the estimated number of transporters needed at a growth rate of  $\approx 0.5$  per hr (light-brown point and dashed lines). Colored points correspond to the mean number of complexes involved in carbohydrate import (complexes annotated with the Gene Ontology terms GO:0009401 and GO:0098704) for different growth conditions across different published datasets. (B) The abundance of various specific carbon transport systems plotted as a function of the population growth rate. The rates of substrate transport differ between these transporter species. To compute the continuum growth rate estimate (grey line), we used the following transport rates for each transporter species: 200 glucose- $s^{-1}$  (BNID: 103693), 2000 glycerol- $s^{-1}$  (**Lu et al., 2003**), 200 fructose- $s^{-1}$  (assumed to be similar to PtsI, BNID: 103693), and 50 xylose- $s^{-1}$  (assumed to be comparable to LacY, BNID: 103159). Red points and highlighted text indicate conditions in which the only source of carbon in the growth medium induces expression of the transport system. Grey lines in (A) and (B) represent the estimated number of transporters per cell at a continuum of growth rates.

**Figure 2-Figure supplement 1.** Estimates and observed abundances of phosphate and sulfate transporters.

**164** complexes present for transporting glucose regardless of growth condition, which is known to be the preferential  
**165** carbon source (*Monod, 1947; Liu et al., 2005; Aidelberg et al., 2014*).

**166** Many metabolic operons are regulated with dual-input logic gates that are only expressed when glucose con-  
**167** centrations are low and the concentration of other carbon sources are elevated (*Gama-Castro et al., 2016; Zhang*  
**168** *et al., 2014; Gama-Castro et al., 2016; Belliveau et al., 2018; Ireland et al., 2020*). Points colored in red in *Fig-*  
**169** *ure 2(B)* (labeled by red text-boxes) correspond to growth conditions in which the specific carbon source (glycerol,  
**170** xylose, or fructose) is present as the sole source of carbon. The grey lines in *Figure 2(B)* show the estimated  
**171** number of transporters needed at each growth rate to satisfy the cellular carbon requirement, adjusted for the  
**172** specific carbon source in terms of number of carbon atoms per molecule and the rate of transport for the par-  
**173** ticular transporter species. These plots show that, in the absence of the particular carbon source, expression of  
**174** the transporters is maintained on the order of  $\sim 10^2$  per cell. The low but non-zero abundances may reflect the  
**175** specific regulatory logic involved, requiring that cells are able to transport some minimal amount of an alternative  
**176** carbon source in order to induce expression of these alternative carbon-source systems.

### **177** **Limits on Transporter Expression**

**178** If acquisition of nutrients was a limiting process in cell division under the typical growth conditions explored here,  
**179** the growth rate could be theoretically increased simply by expressing more transporters, but is this feasible at  
**180** a physiological level? A way to approach this question is to compute the amount of space in the bacterial mem-  
**181** brane that could be occupied by nutrient transporters. Considering a rule-of-thumb for the surface area of *E.*  
**182** *coli* of about  $5 \mu\text{m}^2$  (BNID: 101792), we expect an areal density for 1000 transporters to be approximately 200  
**183** transporters/  $\mu\text{m}^2$ . For a typical transporter occupying about  $50 \text{ nm}^2$ , this amounts to about only  $\approx 1\%$  of the  
**184** total inner membrane area (*Szenk et al., 2017*). Additionally, bacterial cell membranes typically have densities  
**185** of  $10^5$  proteins/ $\mu\text{m}^2$  (*Phillips, 2018*), implying that the cell could accommodate more membrane and this places  
**186** additional limitations on cell size and surface area that we will consider further in the coming sections.

### **187** **Cell Envelope Biogenesis**

**188** In contrast to nutrient transporters, which support the synthesis of biomolecules throughout the cell and therefore  
**189** need to scale with the cell size, here we must consider the synthesis of components that will need to scale with the  
**190** surface area of the cell. *E. coli* is a rod-shaped bacterium with a remarkably robust length-to-width aspect ratio of  
**191**  $\approx 4:1$  (*Harris and Theriot, 2018; Ojkic et al., 2019*). At modest growth rates, the total cell surface area is  $\approx 5 \mu\text{m}^2$   
**192** (BNID: 101792). Assuming this surface area is approximately the same between the inner and outer membranes  
**193** of *E. coli*, and the fact that each membrane is itself a lipid bilayer, cells have a the total membrane surface area of  
**194**  $\approx 20 \mu\text{m}^2$  (see Appendix Estimation of Cell Size and Surface Area for a description of the calculation of cell surface  
**195** area as a function of cell size). In this section, we will estimate the number of protein complexes needed to  
**196** produce this membrane surface area as well as the complexes involved in assembling the peptidoglycan scaffold  
**197** it encapsulates.

### **198** **Lipid Synthesis**

**199** The dense packing of the membrane with proteins means that the cell membranes are not composed entirely  
**200** of lipid molecules, with only  $\approx 40\%$  of the membrane area is occupied by lipids (BNID: 100078). Using a rule-of-  
**201** thumb of  $0.5 \text{ nm}^2$  as the surface area of the typical lipid (BNID: 106993), we can estimate  $\sim 2 \times 10^7$  lipids per cell,  
**202** which is in close agreement with experimental measurements (BNID: 100071, 102996).

**203** The membranes of *E. coli* are composed of a variety of different lipids, each of which are unique in their struc-  
**204** tures and biosynthetic pathways (*Sohlenkamp and Geiger, 2016*). Recently, a combination of stochastic kinetic  
**205** modeling (*Ruppe and Fox, 2018*) and *in vitro* kinetic measurements (*Ranganathan et al., 2012; Yu et al., 2011*)  
**206** have revealed remarkably slow steps in the fatty acid synthesis pathways which may serve as the rate limiting  
**207** reactions for making new membrane phospholipids. One such step is the removal of hydroxyl groups from the  
**208** fatty-acid chain by ACP dehydratase that leads to the formation of carbon-carbon double bonds. This reaction,  
**209** catalyzed by proteins FabZ and FabA in *E. coli* (*Yu et al., 2011*), have been estimated to have kinetic turnover rates  
**210** of  $\approx 1$  dehydration per second per enzyme (*Ruppe and Fox, 2018*). Thus, given this rate and the need to synthe-  
**211** size  $\approx 2 \times 10^7$  lipids over 5000 seconds, one can estimate that a typical cell requires  $\approx 4000$  ACP dehydratases.

212 This is in reasonable agreement with the experimentally observed copy numbers of FabZ and FabA (*Figure 3(A)*).  
213 Furthermore, we can extend this estimate to account for the change in membrane surface area as a function of  
214 the growth rate (grey line in *Figure 3(A)*), which captures the observed growth rate dependent expression of these  
215 two enzymes.

## 216 Peptidoglycan Synthesis

217 Bacterial cells demonstrate exquisite control over their cell shape. This is primarily due to the cell wall, a stiff, sev-  
218 eral nanometer thick meshwork of polymerized discaccharides. The formation of the peptidoglycan is an intricate  
219 process involving many macromolecular players (*Shi et al., 2018; Morgenstein et al., 2015*), whose coordinated  
220 action maintains cell shape and integrity even in the face of large-scale perturbations (*Harris and Theriot, 2018;*  
221 *Shi et al., 2018*). The peptidoglycan alone comprises  $\approx 3\%$  of the cellular dry mass (BNID: 1019360, making it  
222 the most massive molecule in *E. coli*). The polymerized unit of the peptidoglycan is a N-acetylglucosamine and  
223 N-acetylmuramic acid disaccharide, of which the former is functionalized with a short pentapeptide. With a mass  
224 of  $\approx 1000$  Da, this unit, which we refer to as a murein monomer, it is polymerized to form long strands in the  
225 periplasm which are then attached to each other via their peptide linkers. Together, these quantities provide an  
226 estimate of  $\approx 5 \times 10^6$  murein monomers per cell.

227 The crosslinking of the pentapeptides between adjacent glycan strands is responsible for maintaining the struc-  
228 tural integrity of the cell wall and, in principle, each murein monomer can be involved in such a crosslink. In some  
229 microbes, such as in gram-positive bacterium *Staphylococcus aureus*, the extent of crosslinking can be large with  
230  $> 90\%$  of pentapeptides forming a connection between glycan strands. In *E. coli*, however, a much smaller propor-  
231 tion ( $\approx 20\%$ ) of the peptides are crosslinked, resulting in a weaker and more porous cell wall (*Vollmer et al. (2008);*  
232 *Rogers et al. (1980)*). The formation of these crosslinks occurs primarily during the polymerization of the murein  
233 monomers and is facilitated by a family of enzymes called transpeptidases. The four primary transpeptidases of  
234 *E. coli* have only recently been quantitatively characterized *in vivo* via liquid chromatography mass spectrometry  
235 which revealed a notably slow kinetic turnover rate of  $\approx 2$  crosslinking reactions formed per second per enzyme  
236 (*Catherwood et al., 2020*).

237 Assembling these quantities permits us to make an estimate that on the order of  $\approx 100$  transpeptidases per cell  
238 are needed for complete maturation of the peptidoglycan, given a division time of  $\approx 5000$  seconds; a value that is  
239 comparable to experimental observations (*Figure 3(B)*). Expanding this estimate to account for the changing mass  
240 of the peptidoglycan as a function of growth rate (grey line in *Figure 3(B)*) also qualitatively captures the observed  
241 dependence in the data, though systematic disagreements between the different data sets makes the comparison  
242 more difficult.

## 243 Limits on Cell Wall Biogenesis

244 While the processes we have considered represent only a small portion of proteins devoted to cell envelope bio-  
245 genesis, we find it unlikely that they limit cellular growth in general. The relative amount of mass required for lipid  
246 and peptidoglycan components decrease at faster growth rates due to a decrease in their surface area to volume  
247 (S/V) ratio (*Ojicic et al., 2019*). Furthermore, despite the slow catalytic rate of FabZ and FabA in lipid synthesis, exper-  
248 imental data and recent computational modeling has shown that the rate of fatty-acid synthesis can be drastically  
249 increased by increasing the concentration of FabZ (*Yu et al., 2011; Ruppe and Fox, 2018*). With a proteome size  
250 of  $\approx 3 \times 10^6$  proteins, a hypothetical 10-fold increase in expression from 4000 to 40,000 ACP dehydratases would  
251 result in a paltry  $\approx 1\%$  increase in the size of the proteome. In the context of peptidoglycan synthesis, we note  
252 that our estimate considers only the transpeptidase enzymes that are involved lateral and longitudinal elongation  
253 of the peptidoglycan. This neglects the presence of other transpeptidases that are present in the periplasm and  
254 also involved in remodeling and maturation of the peptidoglycan. It is therefore possible that if this was setting  
255 the speed limit for cell division, the simple expression of more transpeptidases may be sufficient to maintain the  
256 structural integrity of the cell wall.

## 257 Energy Production

258 Cells consume and generate energy predominantly in the form of nucleoside triphosphates (NTPs) in order to  
259 grow. The high-energy phosphodiester bonds of (primarily) ATP power a variety of cellular processes that drive

## CELL ENVELOPE BIOSYNTHESIS

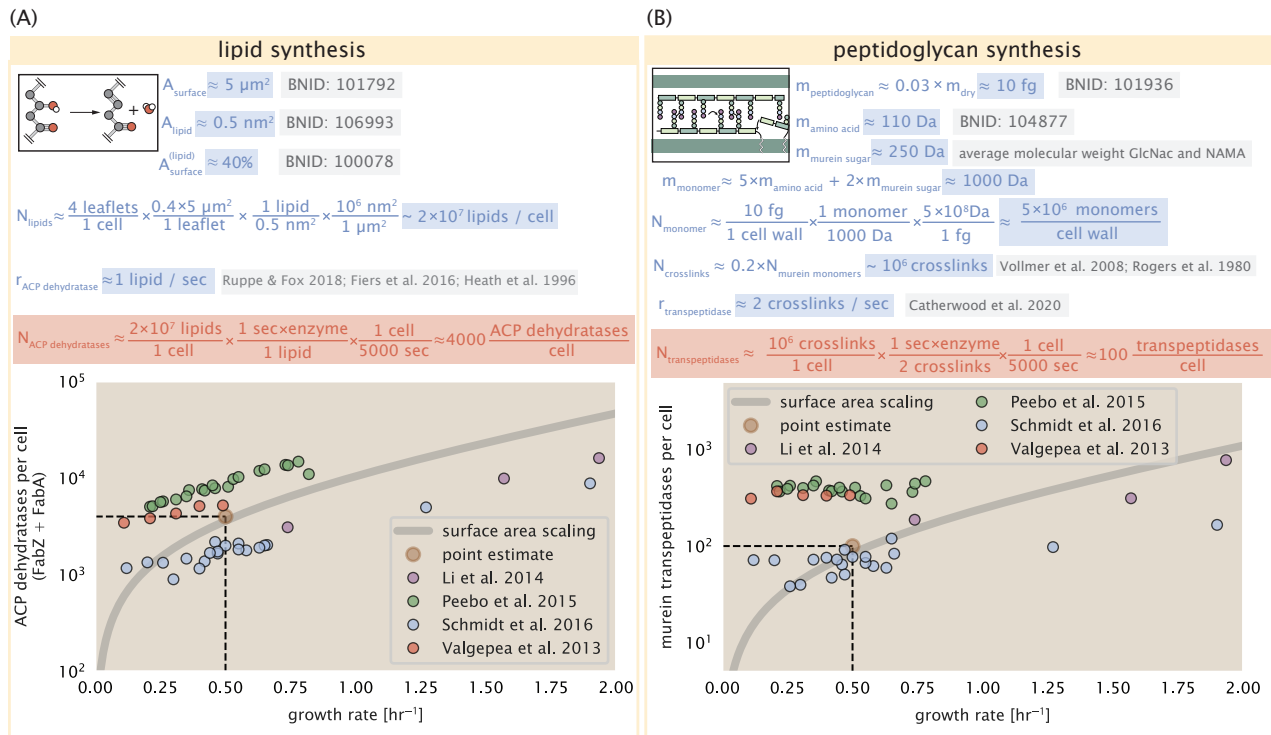


**Figure 3.** (A) Top panel shows an estimation for the number of ACP dehydratases necessary to form functional phospholipids, which is assumed to be a rate-limiting step on lipid synthesis. The rate of ACP dehydratases was inferred from experimental measurements via a stochastic kinetic model described in [Ruppe and Fox \(2018\)](#). Bottom panel shows the experimentally observed complex copy numbers using the stoichiometries  $[\text{FabA}]_2$  and  $[\text{FabZ}]_2$ . (B) An estimate for the number of peptidoglycan transpeptidases needed to complete maturation of the peptidoglycan. The mass of the murein monomer was estimated by approximating each amino acid in the pentapeptide chain as having a mass of 110 Da and each sugar in the disaccharide having a mass of 250 Da. The *in vivo* rate of transpeptidation in *E. coli* was taken from recent analysis by [Catherwood et al. \(2020\)](#). The bottom panel shows experimental measurements of the transpeptidase complexes in *E. coli* following the stoichiometries  $[\text{MrcA}]_2$ ,  $[\text{MrcB}]_2$ ,  $[\text{MrdA}]_1$ , and  $[\text{MrdB}]_1$ . Grey curves in each plot show the estimated number of complexes needed to satisfy the synthesis requirements scaled by the surface area as a function of growth rate.

260 biological systems away from thermodynamic equilibrium. We next turn to the synthesis of ATP as a potential  
261 process that may limit growth, which also requires us to consider the maintenance of the electrochemical proton  
262 gradient which powers it.

### 263 **ATP Synthesis**

264 Hydrolysis of the terminal phosphodiester bond of ATP into ADP (or alternatively GTP and GDP) and an inorganic  
265 phosphate provides the thermodynamic driving force in a wide array of biochemical reactions. One such reaction  
266 is the formation of peptide bonds during translation, which requires  $\approx 2$  ATPs for the charging of an amino acid  
267 to the tRNA and  $\approx 2$  GTP for the formation of each peptide bond. Assuming the ATP costs associated with error  
268 correction and post-translational modifications of proteins are negligible, we can make the approximation that  
269 each peptide bond has a net cost of  $\approx 4$  ATP (BNID: 101442, *Milo et al. (2010)*). Formation of GTP from ATP is  
270 achieved via the action of nucleoside diphosphate kinase, which catalyzes this reaction without an energy invest-  
271 ment (*Lascu and Gonin, 2000*) and therefore consider all NTP requirements of the cell to be functionally equivalent  
272 to being exclusively ATP. In total, the energetic costs of peptide bond formation consume  $\approx 80\%$  of the cells ATP  
273 budget (BNID: 107782; 106158; 101637; 111918, *Lynch and Marinov (2015); Stouthamer (1973)*). The pool of ATP  
274 is produced by the F<sub>1</sub>-F<sub>0</sub> ATP synthase – a membrane-bound rotary motor which under ideal conditions can yield  
275  $\approx 300$  ATP per second (BNID: 114701; *Weber and Senior (2003)*).

276 To estimate the total number of ATP equivalents consumed during a cell cycle, we will make the approximation  
277 that there are  $\approx 3 \times 10^6$  proteins per cell with an average protein length of  $\approx 300$  peptide bonds (BNID: 115702;  
278 108986; 104877). Taking these values together, coupled with an estimate of  $\approx 4$  ATP equivalents per peptide bond,  
279 we find that the typical *E. coli* cell consumes  $\sim 5 \times 10^9$  ATP per cell cycle on protein synthesis alone. Assuming that  
280 each ATP synthases operates at its maximal speed (300 ATP per second per synthase),  $\approx 3000$  ATP synthases  
281 are needed to keep up with the energy demands of the cell. This estimate is comparable with the experimental  
282 observations, shown in *Figure 4* (A). We note that this estimate assumes all ATP is synthesized via ATP synthase  
283 and neglects synthesis via fermentative metabolism. This assumption may explain why at the fastest growth rates  
284 ( $\approx 2$  hr<sup>-1</sup>), our continuum estimate predicts more synthase than is experimentally observed (gray line in *Figure 4*).  
285 At rapid growth rates, *E. coli* enters a type of overflow metabolism where fermentative metabolism becomes  
286 pronounced (*Szenk et al., 2017*).

### 287 **Generating the Proton Electrochemical Gradient**

288 In order to produce ATP, the F<sub>1</sub>-F<sub>0</sub> ATP synthase itself must consume energy. Rather than burning through its own  
289 product (and violating thermodynamics), this intricate macromolecular machine has evolved to exploit the elec-  
290 trochemical potential established across the inner membrane through cellular respiration. This electrochemical  
291 gradient is manifest by the pumping of protons into the intermembrane space via the electron transport chains  
292 as they reduce NADH. In *E. coli*, this potential difference is  $\approx -200$  mV (BNID: 102120). A simple estimate of the  
293 inner membrane as a capacitor with a working voltage of -200 mV reveals that  $\approx 2 \times 10^4$  protons must be present  
294 in the intermembrane space. However, each rotation of an ATP synthase shuttles  $\approx 4$  protons into the cytosol  
295 (BNID: 103390). With a few thousand ATP synthases producing ATP at their maximal rate, the potential difference  
296 would be rapidly abolished in a few milliseconds if it were not being actively maintained.

297 The electrochemistry of the electron transport complexes of *E. coli* have been the subject of intense biochemical  
298 and biophysical study (*Ingledew and Poole, 1984; Khademian and Imlay, 2017; Cox et al., 1970; Henkel et al., 2014*).  
299 A recent work (*Szenk et al., 2017*) examined the respiratory capacity of the *E. coli* electron transport complexes  
300 using structural and biochemical data, revealing that each electron transport chain rapidly pumps protons into  
301 the intermembrane space at a rate of  $\approx 1500$  protons per second (BIND: 114704; 114687). Using our estimate  
302 of the number of ATP synthases required per cell [*Figure 4(A)*], coupled with these recent measurements, we  
303 estimate that  $\approx 3000$  electron transport complexes would be necessary to facilitate the  $\sim 5 \times 10^6$  protons per  
304 second diet of the cellular ATP synthases. This estimate is in agreement with the number of complexes identified  
305 in the proteomic datasets (plot in *Figure 4(B)*). This suggests that every ATP synthase must be accompanied by  $\approx$   
306 1 functional electron transport chain.

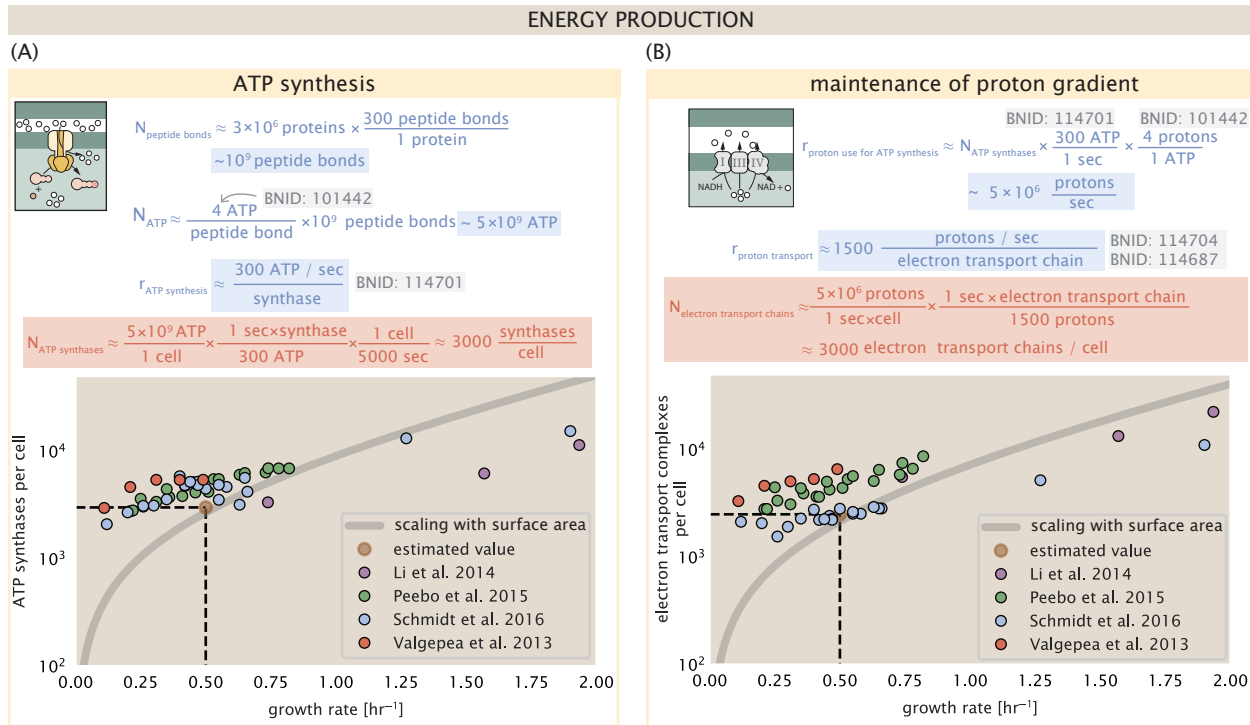


**Figure 4. The abundance of F<sub>1</sub>-F<sub>0</sub> ATP synthases and electron transport chain complexes as a function of growth rate.**

(A) Estimate of the number of F<sub>1</sub>-F<sub>0</sub> ATP synthase complexes needed to accommodate peptide bond formation and other NTP dependent processes. Points in plot correspond to the mean number of complete F<sub>1</sub>-F<sub>0</sub> ATP synthase complexes that can be formed given proteomic measurements and the subunit stoichiometry [AtpE]<sub>10</sub>[AtpF]<sub>2</sub>[AtpB][AtpC][AtpH][AtpA]<sub>3</sub>[AtpG][AtpD]<sub>3</sub>. (B) Estimate of the number of electron transport chain complexes needed to maintain a membrane potential of -200 mV given estimate of number of F<sub>1</sub>-F<sub>0</sub> ATP synthases from (A). Points in plot correspond to the average number of complexes identified as being involved in aerobic respiration by the Gene Ontology identifier GO:0019646 that could be formed given proteomic observations. These complexes include cytochromes *bd1* ([CydA][CydB][CydX][CydH]), *bdII* ([AppC][AppB]), *bo<sub>3</sub>*,([CyoD][CyoA][CyoB][CyoC]) and NADH:quinone oxioreductase I ([NuoA][NuoH][NuoJ][NuoK][NuoL][NuoM][NuoN][NuoB][NuoC][NuoE][NuoF][NuoG][NuoI]) and II ([Ndh]). Grey lines in both (A) and (B) correspond to the estimate procedure described, but applied to a continuum of growth rates. We direct the reader to the Supporting Information for a more thorough description of this approach.

307 Limits on Biosynthesis in a Crowded Membrane

308 Our estimates thus far have focused on biochemistry at the periphery of the cell and have generally been con-  
309 cordant with the abundances predicted by our estimates. However, as surface area and volume do not scale  
310 identically, it is necessary to consider the physical limits for transport and energy production given the S/V ratio,  
311 which as we've noted will decrease at faster growth rates.

312 In our estimate of ATP production above we found that a cell demands about  $5 \times 10^9$  ATP per cell cycle or  $10^6$   
313 ATP/s. With a cell volume of roughly 1 fL (BNID: 100004), this corresponds to about  $2 \times 10^{10}$  ATP per fL of cell  
314 volume, in line with previous estimates (*Stouthamer and Bettenhausen, 1977; Szenk et al., 2017*). In *Figure 5* (A)  
315 we plot this ATP demand as a function of the S/V ratio in green, where we have considered a range of cell shapes  
316 from spherical to rod-shaped with an aspect ratio (length/width) equal to 4. In order to consider the maximum  
317 ATP that could be produced, we consider the amount of ATP that can be generated by a membrane filled with ATP  
318 synthase and electron transport complexes, which provides a maximal production of about 3 ATP / (nm<sup>2</sup>·s) (*Szenk*  
319 *et al., 2017*). This is shown in blue in *Figure 5*(A), which shows that at least for the growth rates observed (right  
320 column in plot), the energy demand is roughly an order of magnitude less. Interestingly, *Szenk et al. (2017)* also  
321 found that ATP production by respiration is less efficient than by fermentation per membrane area occupied due  
322 to the additional proteins of the electron transport chain. This suggests that, even under anaerobic growth, there  
323 will be sufficient membrane space for ATP production.

324 The analysis highlights the diminishing capacity to provide resources as the cell increases in size. However,  
325 the maximum energy production in *Figure 5*(A) does represents a somewhat unachievable limit since the inner  
326 membrane must also include other proteins including those required for lipid and membrane synthesis. To bet-  
327 ter understand the overall proteomic makeup of the inner membrane, we therefore used Gene Ontology (GO)  
328 annotations (*Ashburner et al., 2000; The Gene Ontology Consortium, 2018*) to identify all proteins embedded  
329 or peripheral to the inner membrane (GO term: 0005886). Those associated but not membrane-bound include  
330 proteins like MreB and FtsZ and must nonetheless be considered as a vital component occupying space on the  
331 membrane. In *Figure 5*(B), we find that the total protein mass per  $\mu\text{m}^2$  is nearly constant across growth rates. In-  
332 terestingly, when we consider the distribution of proteins grouped by their Clusters of Orthologous Groups (COG)  
333 (*Tatusov et al., 2000*), the relative abundance for those in metabolism (including ATP synthesis via respiration) is  
334 also relatively constant across growth rates, suggesting that no one process (energy production, nutrient uptake,  
335 etc.) is particularly dominating even at fast growth rates *Figure 5*(C).

336 **Processes of the Central Dogma**

337 Up to this point, we have considered a variety of transport and biosynthetic processes that are critical to acquiring  
338 and generating new cell mass. While there are of course many other metabolic processes we could consider, we  
339 now turn our focus to some of the most central processes which *must* be undertaken irrespective of the growth  
340 conditions – those of the central dogma.

341 **DNA Replication**

342 Most bacteria (including *E. coli*) harbor a single, circular chromosome and can have extra-chromosomal plasmids  
343 up to  $\sim 100$  kbp in length. While we consider the starting material dNTPs in *Figure 6–Figure Supplement 1* and  
344 discussed further in Appendix ??, here we focus our quantitative thinking on the chromosome of *E. coli* which  
345 harbors  $\approx 5000$  genes and  $\approx 5 \times 10^6$  base pairs.

346 To successfully divide and produce viable progeny, this chromosome must be faithfully replicated and segre-  
347 gated into each nascent cell. Replication is initiated at a single region of the chromosome termed the *oriC* locus  
348 at which a pair of replisomes, each consisting of two DNA polymerase III, begin their high-fidelity replication of  
349 the genome in opposite directions (*Fijalkowska et al., 2012*). *In vitro* measurements have shown that DNA Poly-  
350 merase III copies DNA at a rate of  $\approx 600$  nucleotides per second (BNID: 104120). Therefore, to replicate a single  
351 chromosome, two replisomes moving at their maximal rate would copy the entire genome in  $\approx 4000$  s. Thus, with  
352 a division time of 5000 s, there is sufficient time for a pair of replisomes complexes to replicate the entire genome.

353 In rapidly growing cultures, bacteria like *E. coli* can initiate as many as 10 - 12 replication forks at a given time  
354 (*Bremer and Dennis, 2008; Si et al., 2017*), we expect only a few DNA polymerases ( $\approx 10$ ) are needed. However,

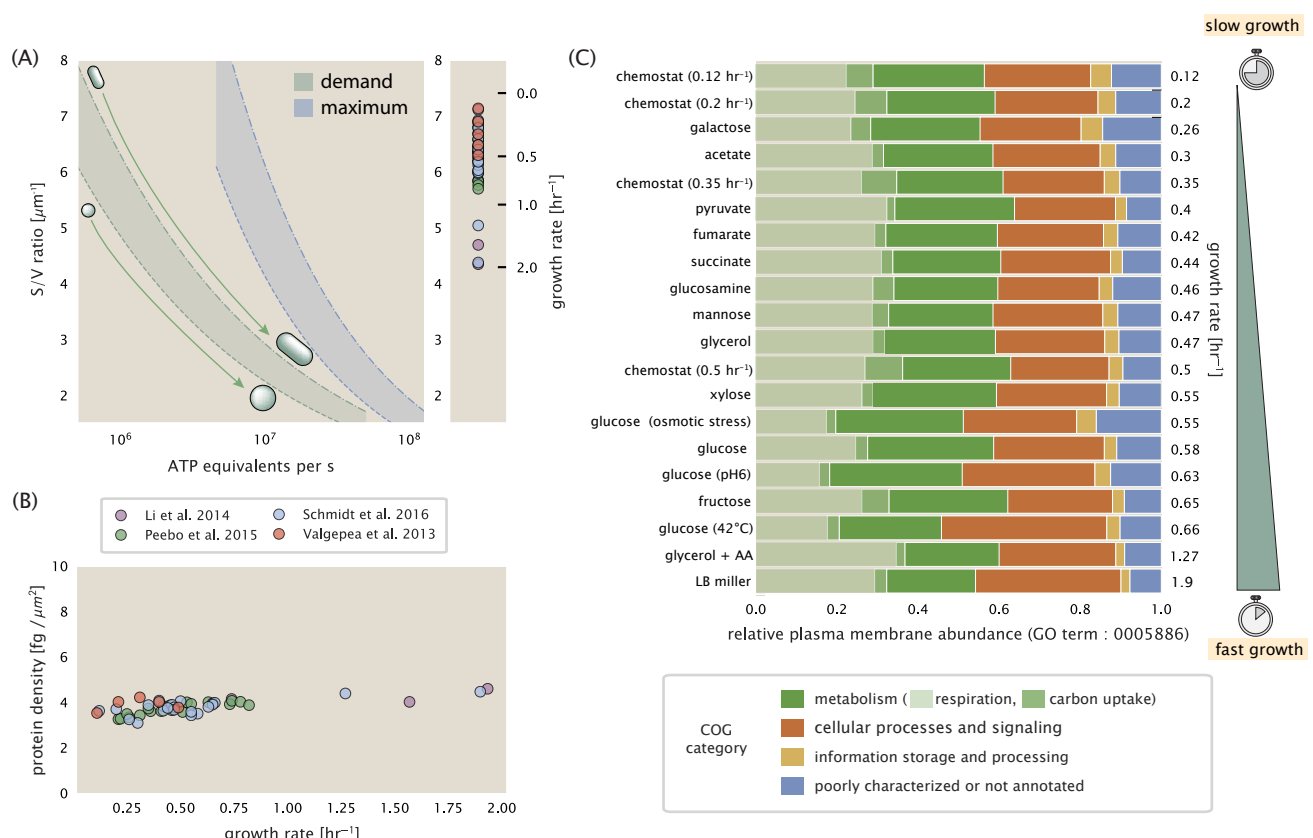


**Figure 5. Influence of cell size and S/V ratio on ATP production and inner membrane composition.** (A) Scaling of ATP demand and maximum ATP production as a function of S/V ratio. Cell volumes of 0.5 fL to 50 fL were considered, with the dashed (—) line corresponding to a sphere and the dash-dot line (---) reflecting a rod-shaped bacterium like *E. coli* with a typical aspect ratio (length / width) of 4 (Shi et al., 2018). Approximately 50% of the bacterial inner membrane is assumed to be protein, with the remainder lipid. The right plot shows the measured growth rates, and their estimated S/V ratio using growth rate dependent size measurements from Si et al. (2017) (See Appendix Estimation of Cell Size and Surface Area on calculation). (B) Total protein mass per  $\mu\text{m}^2$  calculated for proteins with inner membrane annotation (GO term: 0005886). (C) Relative protein abundances by mass based on COG annotation. Metabolic proteins are further separated into respiration ( $F_1$ - $F_0$  ATP synthase, NADH dehydrogenase I, succinate:quinone oxidoreductase, cytochrome  $bo_3$  ubiquinol oxidase, cytochrome bd-ubiquinol oxidase) and carbohydrate transport (GO term: GO:0008643). Note that the elongation factor EF-Tu can also associate with the inner membrane, but was excluded in this analysis due to its high relative abundance (roughly identical to the summed protein shown in part (B)).

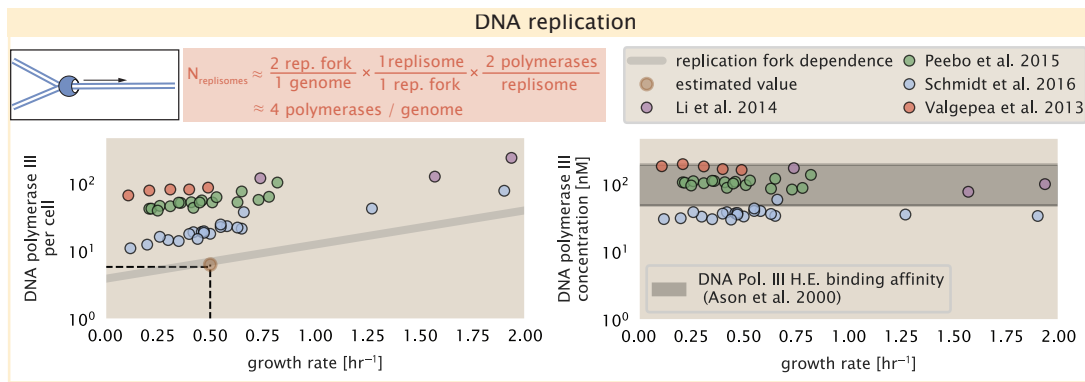


**Figure 6. Complex abundance estimates for dNTP synthesis and DNA replication.** An estimate for the minimum number of DNA polymerase holoenzyme complexes needed to facilitate replication of a single genome. Points in the left-hand plot correspond to the total number of DNA polymerase III holoenzyme complexes ( $[\text{DnaE}]_3[\text{DnaQ}]_3[\text{HolE}]_3[\text{DnaX}]_5[\text{HolB}][\text{HolA}][\text{DnaN}]_4[\text{HolC}]_4[\text{Hold}]_4$ ) per cell. Right-hand plot shows the effective concentration of DNA polymerase III holoenzyme (See Appendix Estimation of Cell Size and Surface Area for calculation of cell size). Grey lines in left-hand panel show the estimated number of complexes needed as a function of growth, the details of which are described in the Supplemental Information.

**Figure 6-Figure supplement 1.** Estimate and observations of the abundance of ribonucleotide reductase, a key component in dNTP synthesis.

as shown in **Figure 6** DNA polymerase III is nearly an order of magnitude more abundant. This discrepancy can be understood by considering its binding constant to DNA. *In vitro* characterization has quantified the  $K_D$  of DNA polymerase III holoenzyme to single-stranded and double-stranded DNA to be 50 and 200 nM, respectively (Ason et al., 2000). The right-hand plot in **Figure 6** shows that the concentration of DNA polymerase III across all data sets is within this range. Thus, its copy number appears to vary such that its concentration is approximately equal to the dissociation constant to the DNA. While the processes regulating the initiation of DNA replication are complex and involve more than just the holoenzyme, these data indicate that the kinetics of replication rather than the explicit copy number of the DNA polymerase III holoenzyme is the more relevant feature of DNA replication to consider. In light of this, the data in **Figure 6** suggests that for bacteria like *E. coli*, DNA replication does not represent a rate-limiting step in cell division. However, it is worth noting that for bacterium like *C. crescentus* whose chromosomal replication is initiated only once per cell cycle (Jensen et al., 2001), the time to double their chromosome indeed represents an upper limit to their growth rate.

## RNA Synthesis

We now turn our attention to the next stage of the central dogma – the transcription of DNA to form RNA. We consider three major groupings of RNA, namely the RNA associated with ribosomes (rRNA), the RNA encoding the amino-acid sequence of proteins (mRNA), and the RNA which links codon sequence to amino-acid identity during translation (tRNA).

rRNA serves as the catalytic and structural component of the ribosome, comprising approximately 2/3 of the total ribosomal mass, and is decorated with  $\approx 50$  ribosomal proteins. Each ribosome contains three rRNA molecules of lengths 120, 1542, and 2904 nucleotides (BNID: 108093), meaning each ribosome contains  $\approx 4500$  nucleotides overall. *In vivo* measurements of the kinetics of rRNA transcription have revealed that RNA polymerases are loaded onto the promoter of an rRNA gene at a rate of  $\approx 1$  per second (BNID: 111997, 102362). If RNA polymerases are constantly loaded at this rate, then we can assume that  $\approx 1$  functional rRNA unit is synthesized per second per rRNA operon. While *E. coli* possesses 7 of these operons per chromosome, the fact that chromosome replication can be parallelized means that the average dosage of rRNA genes can be substantially higher (up to  $\approx 70$  copies) at fast growth rates. At a growth rate of  $\approx 0.5 \text{ hr}^{-1}$ , however, the average cell has  $\approx 1$  copy of its chromosome and therefore approximately  $\approx 7$  copies of the rRNA operons, therefore producing  $\approx 7$  rRNA units per second. With a 5000 second division time, this means the cell is able to generate around  $3 \times 10^4$  functional rRNA units, comparable within an order of magnitude to the number of ribosomes per cell.

384 How many RNA polymerases are then needed to constantly transcribe the required rRNA? If one polymerase is  
385 loaded per second, and the transcription rate is  $\approx$  40 nucleotides per second (BNID: 101094), then the typical  
386 spacing between polymerases will be  $\approx$  40 nucleotides. However, we must note that the polymerase itself has a  
387 footprint of  $\approx$  40 nucleotides (BNID: 107873), meaning that one could expect to find one RNA polymerase per 80  
388 nucleotide stretch of an rRNA gene. With a total length of  $\approx$  4500 nucleotides per operon and 7 operons per cell,  
389 the number of RNA polymerases transcribing rRNA at any given time is then  $\approx$  500 per cell.

390 As outlined in *Figure 7*, and discussed further the Appendix ??, synthesis of mRNA and tRNA together require  
391 on the order of  $\approx$  400 RNAP. Thus, in total, one would expect the typical cell to require  $\approx$  1000 RNAP to satisfy  
392 its transcriptional demands. As is revealed in *Figure 7(B)*, this estimate is about an order of magnitude below the  
393 observed number of RNA polymerase complexes per cell ( $\approx$  5000 - 7000). The difference between the estimated  
394 number of RNA polymerase needed for transcription and these observations, however, are consistent with recent  
395 literature revealing that  $\approx$  80 % of RNA polymerases in *E. coli* are not transcriptionally active (Patrick et al., 2015).

396 Our estimates also neglect other mechanistic features of transcription and transcriptional initiation more  
397 broadly. For example, we acknowledge that some fraction of the RNAP pool is nonspecifically bound to DNA  
398 during its search for promoters from which to begin transcription. Furthermore, we ignore the obstacles that RNA  
399 polymerase and DNA polymerase present to each other as they move along the DNA (Finkelstein and Greene,  
400 2013). Finally, we neglect the fact that RNA polymerase also require  $\sigma$ -factors for promoter recognition and tran-  
401 scription initiation (Browning and Busby, 2016).

402 While they are the machinery for transcription, RNA polymerase is not sufficient to initiate transcription. Pro-  
403 moter recognition and initiation of transcription is dependent on the presence of  $\sigma$ -factors, protein cofactors  
404 which bind directly to the polymerase (Browning and Busby, 2016). In *Figure 7-Figure Supplement 1*, we show  
405 that the predicted RNA polymerase copy number indeed is more comparable with the abundance of  $\sigma$ -70 (RpoD),  
406 the primary sigma factor in *E. coli*. There therefore remains more to be investigated as to what sets the observed  
407 abundance of RNA polymerase in these proteomic data sets. However, we conclude that our the observed excess  
408 in abundance for RNA polymerase abundances are generally in excess of what appears to be needed for growth,  
409 suggesting that the abundance of RNA polymerase itself is not particularly limiting.

## 410 Protein Synthesis

411 We conclude our dialogue between back-of-the-envelope estimates and comparison with the proteomic data by  
412 examining the final process in the central dogma – translation. In doing so, we will begin with an estimate of the  
413 number of ribosomes needed to replicate the cellular proteome. While the rate at which ribosomes translate is  
414 well known to be dependent on the growth rate (Dai et al. (2018), phenomenon we consider later in this work) we  
415 will make the approximation that translation occurs at a modest rate of  $\approx$  15 amino acids per second per ribosome  
416 (BNID: 100233) Under this approximation and our previous estimate of  $10^9$  peptide bonds per cell at a growth rate  
417 of  $0.5 \text{ hr}^{-1}$ , we can easily arrive at an estimate of  $\approx 10^4$  ribosomes needed per cell to replicate the entire protein  
418 mass (*Figure 8(A)*, top). This point estimate, as well as the corresponding estimate across a continuum of growth  
419 rates, proves to be notably comparable to the experimental observations, shown in the bottom panel of *Figure 8(A)*.  
420 While the ribosome is responsible for the formation of peptide bonds, we do not diminish the importance of  
421 charging tRNAs with their appropriate amino acid, a process with occurs with remarkable fidelity. In the Appendix  
422 and in *Figure 8-Figure Supplement 1*, we consider the process of ligating tRNAs to their corresponding amino acid  
423 and again find notable comparability with the data.

424 Having completed our circuit through key processes of cellular growth outlined in *Figure 1*, we can now take  
425 stock on our understanding of the observed growth rate dependence and abundances of various protein com-  
426 plexes. We note that, broadly speaking, these simple estimates have been reasonably successful in quantitatively  
427 describing the observations in the proteomic data, suggesting that the proteome is tuned in composition and  
428 absolute abundance to match the growth rate requirements without any one process representing a singular bot-  
429 tleneck or rate limiting step in division. However, in our effort to identify key limitations on growth, there are two  
430 notable observations that we wish to emphasize.

431 The first is a recurring theme throughout our estimates. Of those investigated here, any inherent biochemical  
432 rate limitation can be overcome by expressing more proteins. We can view this as a parallelization of each biosyn-  
433 thesis task, which helps explain why bacteria tend to increase their protein content (and cell size) as growth rate

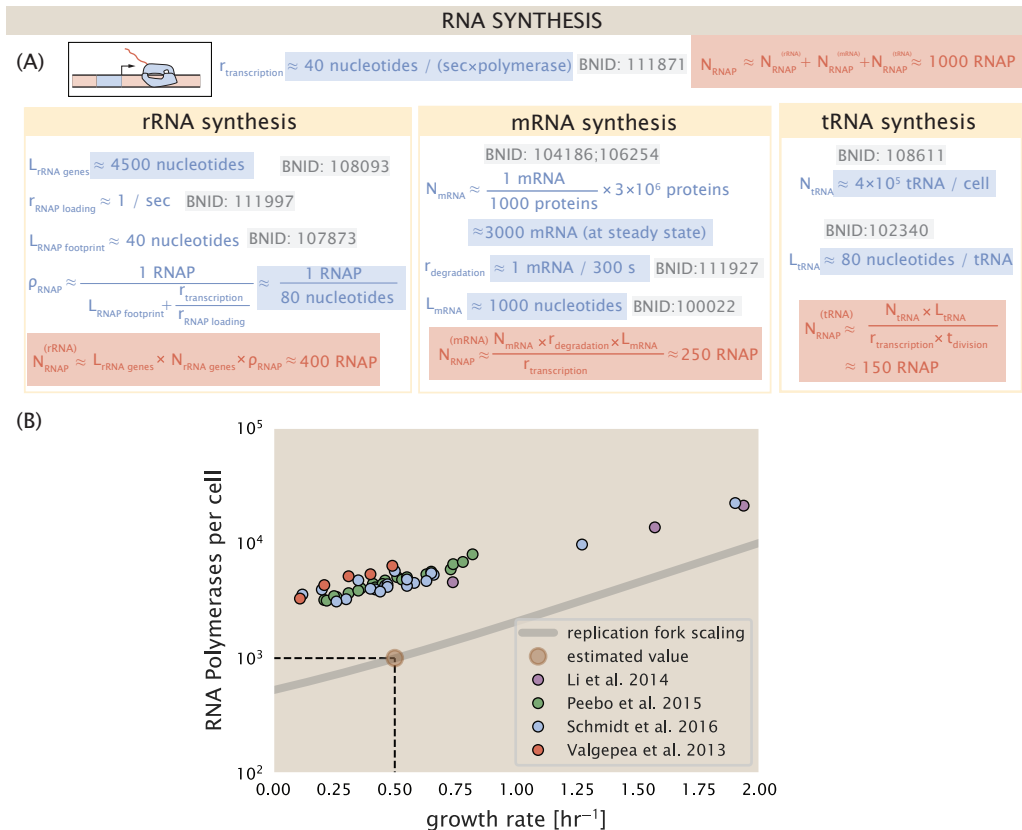


**Figure 7. Estimation of the RNA polymerase demand and comparison with experimental data.** (A) Estimations for the number of RNA polymerase needed to synthesize sufficient quantities of rRNA, mRNA, and tRNA from left to right, respectively.(B) The RNA polymerase core enzyme copy number as a function of growth rate. Colored points correspond to the average number RNA polymerase core enzymes that could be formed given a subunit stoichiometry of  $[RpoA]_2[RpoC][RpoB]$ .

**Figure 7-Figure supplement 1.** Abundance and growth rate dependence of  $\sigma$ -70.

434 increases (*Ojkic et al., 2019*). The second, and ultimately the most significant in defining the cellular growth rate, is  
 435 that the synthesis of ribosomal proteins presents a special case where parallelization is *not* possible and thereby  
 436 imposes a limit on the fastest possible growth rate. Each ribosome has  $\approx 7500$  amino acids across all of its pro-  
 437 tein components which must be strung together as peptide bonds through the action of another ribosome. Once  
 438 again using a modest elongation rate of  $\approx 15$  amino acids per second, we arrive at an estimate of  $\approx 500$  seconds or  
 439  $\approx 7$  minutes to replicate a single ribosome. This limit, as remarked upon by others (*Dill et al., 2011*), serves as a  
 440 hard theoretical boundary for how quickly *E. coli* could replicate. As each ribosome would therefore need to copy  
 441 itself, this 7 minute speed limit is independent of the number of ribosomes per cell (*Figure 8(B)*), yet assumes that  
 442 the only proteins that need to be replicated for division to occur are ribosomal proteins, an unrealistic regime not  
 443 met in biological reality. This poses an optimization problem for the cell – how are the translational demands of  
 444 the entire proteome met without investing resources in the production of an excess of ribosomes?

445 This question, more frequently presented as a question of optimal resource allocation, has been the target of  
 446 an extensive dialogue between experiment and theory over the past decade. In a now seminal work, *Scott et al.*  
 447 (*2010*) presents an elegant treatment of resource allocation through partitioning of the proteome into sectors –  
 448 one of which being ribosome-associated proteins whose relative size ultimately defines the total cellular growth  
 449 rate. In more recent years, this view has been more thoroughly dissected experimentally (*Klumpp and Hwa, 2014*;  
 450 *Basan et al., 2015; Dai et al., 2018, 2016; Erickson et al., 2017*) and together have led to a paradigm-shift in how we  
 451 think of cellular physiology at the proteomic-level. However, the quantitative description of these observations is  
 452 often couched in terms of phenomenological constants and effective parameters with the key observable features  
 453 of expression often computed in relative, rather than absolute, abundances. Furthermore, these approaches  
 454 often exclude or integrate away effects of cell size and chromosome content, which we have found through our  
 455 estimates to have important connections to the observed cellular growth rate.

456 In the closing sections of this work, we explore how ribosomal content, total protein abundance, and chromo-  
 457 somal replication are intertwined in their control over the cellular growth rate. To do so, we take a more careful  
 458 view of ribosome abundance, exchanging our order-of-magnitude estimates for a minimal mathematical model  
 459 of growth rate control. This is defined by parameters with tangible connections to the biological processes under-  
 460 lying cellular growth and protein synthesis. Using this model, we interrogate how the size of the ribosome pool  
 461 and its corresponding translational capacity enable cells to maintain a balance between the of amino acids via  
 462 metabolism and catabolism and their consumption through the peptide bond formation required for growth.

## 463 Maximum Growth Rate is Determined by the Ribosomal Mass Fraction

464 The 7 minute speed limit shown in *Figure 8(B)* assumes all proteins in the cell are ribosomes. In order to connect  
 465 this to the experimental data (and physiological reality more broadly), we first need to relax this assumption and  
 466 determine a translation-limited growth rate. Here, we will assume that the cell is composed of  $N_{\text{pep}}$  peptide bonds  
 467 and  $R$  ribosomes, whose precise values will depend on the growth rate  $\lambda$ . The protein subunits of each ribosomal  
 468 protein sum to a total of  $\approx 7500$  amino acids as noted earlier, which we denote by  $L_R$ . With an average mass of  
 469 an amino acid of  $m_{\text{AA}} \approx 110$  Da (BNID: 104877), the total ribosomal mass fraction  $\Phi_R$  is given by

$$\Phi_R = \frac{m_{\text{ribosomes}}}{m_{\text{proteome}}} \approx \frac{m_{\text{AA}} \times R \times L_R}{m_{\text{AA}} \times N_{\text{pep}}} = \frac{R \times L_R}{N_{\text{pep}}}. \quad (1)$$

470 For exponentially growing cells (*Godin et al., 2010*), the rate of cellular growth will be related to the rate of protein  
 471 synthesis via

$$\lambda N_{\text{pep}} = r_t \times R \times f_a, \quad (2)$$

472 where  $r_t$  is the translation rate. Here, we've introduced a multiplicative factor  $f_a$  which represents the fraction of  
 473 the ribosomes that are actively translating. This term allows us to account for immature or non-functional ribo-  
 474 somes or active sequestration of ribosomes through the action of the secondary messenger alarmone (p)ppGpp  
 475 in poorer nutrient conditions (*Hauryliuk et al. (2015)*).

476 Combining *Equation 1* and *Equation 2* results in an expression for a translation-limited growth rate, which is  
 477 given by

$$\lambda_{\text{translation-limited}} = \frac{r_t \times \Phi_R \times f_a}{L_R}. \quad (3)$$

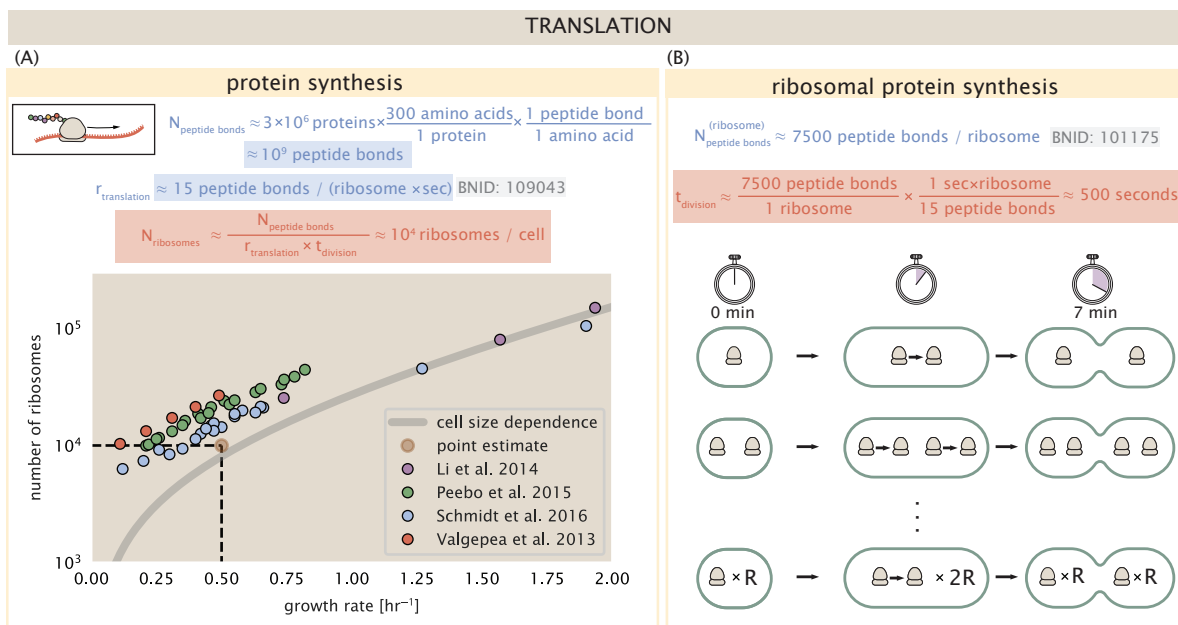


**Figure 8. Estimation of the required number of ribosomes and the speed limit for bacterial replication.** (A) Estimation of the number of ribosomes required to synthesize  $10^9$  peptide bonds with an elongation rate of 15 peptide bonds per second. The average abundance of ribosomes is plotted as a function of growth rate. Our estimated values are shown for a growth rate of  $0.5 \text{ hr}^{-1}$ . Grey lines correspond to the estimated complex abundance calculated at different growth rates. (B) Estimation for the time to replicate a ribosome. This rate is independent of the number of ribosomes  $R$  and instead is limited by the time required to double an individual ribosome.

**Figure 8-Figure supplement 1.** Estimate and observed abundance and growth rate dependence of tRNA ligases.

478 This result, derived in a similar manner in ?, reflects mass-balance under steady state growth and has long provided  
 479 a rationalization of the apparent linear increase in *E. coli*'s ribosomal content as a function growth rate (*Maaløe,*  
 480 *Dennis et al., 2004; Scott et al., 2010*). The left-hand panel of **Figure 9(A)** shows this growth rate plotted as  
 481 a function of the ribosomal mass fraction. In the regime where all ribosomes are active ( $f_a = 1$ ) and the entire  
 482 proteome is composed of ribosomal proteins ( $\Phi_R = 1$ ), indeed, we arrive at the maximum theoretical growth rate  
 483 of  $r_t/L_R$ , and  $\approx 7 \text{ min}$  for *E. coli*.

484 Connecting **Equation 3** to the proteomic data serving as the centerpiece of our work, however, requires knowl-  
 485 edge of  $f_a$  at each growth rate as proteomic measurements only provide a measure of  $\Phi_R$ . Recently, *Dai et al.*  
 486 (2016) determined  $f_a$  as a function of the growth rate (**Figure 9(A)**, right-hand panel, inset), revealing that  $f_a \approx 1$   
 487 at growth rates above  $0.75 \text{ hr}^{-1}$  and  $f_a < 1$  as the growth rate slows. Using these data, we inferred the approx-  
 488 imate active fraction (see Appendix Calculation of active ribosomal fraction) at each growth rate and used this  
 489 to compute  $\Phi_R \times f_a$  (**Figure 9(A)**, colored points in right-hand panel). In general, these data skirt the translation-  
 490 limited growth rate determined using **Equation 3** with  $r_t$ , taken to be the maximal elongation rate of 17 amino acids  
 491 per second measured by *Dai et al. (2016)*. There is a notable discrepancy between the data collected in *Schmidt*  
 492 *et al. (2016)*; *Li et al. (2014)* and that collected from *Valgepeea et al. (2013)*; *Peebo et al. (2015)*. When compared to  
 493 other measurements (non-proteomic with significantly lower resolution) of the active ribosome mass fraction (**Fig-**  
 494 **ure 9(B)**, grey points in right-hand panel), the data from *Valgepeea et al. (2013)* and *Peebo et al. (2015)* are notably  
 495 aberrant, suggesting a systematic error in these data. These additional measurements come from a number of  
 496 recent studies and are determined from measurements of total RNA to total protein mass ratios (**Figure 9-Figure**  
 497 **Supplement 1**).

498 Together, these results illustrate that the growth rates observed across the amalgamated data sets are close  
 499 to the translation-limited growth rate determined through their ribosomal activity, at least for the data reported in  
 500 *Schmidt et al. (2016)* and *Li et al. (2014)*. While this is a useful framework to consider how the relative abundance  
 501 of ribosomes (compared to all other proteins) defines the growth rate, it is worth noting that as growth rate  
 502 increases, so does the cell size and therefore so will the total proteomic mass (*Basan et al., 2015*). With a handle

503 on how elongation rate and the total number of peptide bonds per proteome is related to the growth rate, we  
504 now expand this description to account for the increasing cell size and ribosome copy number at faster growth  
505 rates, enabling us to identify a potential bottleneck in the synthesis of rRNA.

## 506 **rRNA Synthesis Presents a Potential Bottleneck During Rapid Growth**

507 Even under idealized experimental conditions, *E. coli* rarely exhibits growth rates above  $2 \text{ hr}^{-1}$  (*Bremer and Dennis, 2008*), which is still well-below the synthesis rate of a single ribosome, and below the maximum growth rates reported for several other bacteria (*Roller et al., 2016*). While we have considered potential limits imposed by translation of ribosomal proteins, here we consider potential limiting regimes for the production of rRNA.

511 Due to multiple initiations of chromosomal replication per cell doubling, the effective number of rRNA operons  
512 increases with growth rate and will do so in proportion to the average number of origins per cell,  $\langle \# \text{ ori} \rangle$ . This latter  
513 parameter is set by how often replication must be initiated in order to keep up with cell doubling times  $\tau$  whose  
514 time may be shorter than the cell cycle time  $t_{\text{cyc}}$  (referring to the time from replication initiation to cell division)  
515 *Dennis et al. (2004)*. This is quantified by

$$\langle \# \text{ ori} \rangle = 2^{t_{\text{cyc}}/\tau} = 2^{t_{\text{cyc}} \lambda / \log(2)}. \quad (4)$$

516 We used the experimental measurements of  $t_{\text{cyc}}$  (the timescale of chromosome replication and cell division) and  
517  $\tau$  (the timescale of a cell doubling) from *Si et al. (2017)* (*Figure 9–Figure Supplement 1(B)*) to calculate  $\langle \# \text{ ori} \rangle$  with  
518 **Equation 4** as a function of growth rates. For growth rates above about  $0.5 \text{ hr}^{-1}$ ,  $t_{\text{cyc}}$  is approximately constant  
519 at about 70 minutes, implying that  $\langle \# \text{ ori} \rangle$  will grow exponentially with growth rates beyond  $0.5 \text{ hr}^{-1}$ . As the  
520 rRNA operons are predominantly located close to origin of replication (BNID: 100352), we make the simplifying  
521 assumption that that the number of rRNA operons will be directly proportional to  $\langle \# \text{ ori} \rangle$ .

522 Returning to our rule-of-thumb of 1 functional rRNA unit per second per transcribing operon, we estimate the  
523 maximum number of ribosomes that could be made as a function of growth rate (*Figure 9(B)*, blue curve). Although  
524 we expect this estimate to significantly overestimate rRNA abundance at slower growth rates ( $\lambda < 0.5 \text{ hr}^{-1}$ ), this  
525 provides a useful reference alongside the proteomic measurements particularly in the regime of fast growth. For  
526 growth rates above about  $1 \text{ hr}^{-1}$ , for example, we find that cells will need to transcribe rRNA near their maximal  
527 rate. As a counter example, if *E. coli* did not initiate multiple rounds of replication, but managed to replicate their  
528 chromosome within the requisite time limit, they would be unable to make enough rRNA for the observed number  
529 of ribosomes (dashed blue curve in *Figure 9(C)*). The convergence between the maximum rRNA production and  
530 measured ribosome copy number suggests rRNA synthesis may begin to present a bottleneck at the fastest growth  
531 rates due to the still-limited copies of rRNA genes.

## 532 **Rapid Growth Requires *E. coli* to Increase Both Cell Size and Ribosomal Mass Fraction**

533 In *Figure 9(B*, right-hand side) we find that above about  $0.75 \text{ hr}^{-1}$ , the growth rate is determined by the ribosomal  
534 mass fraction  $\Phi_R$ , since  $f_a$  is close to 1, and  $r_f$  is near its maximal rate (*Dai et al., 2016*). While  $\Phi_R$  will need to  
535 increase in order for cells to grow faster, the fractional dependence in ?? gives little insight into how this is actually  
536 achieved in the cell.

537 It is now well-documented that *E. coli* cells add a constant volume per origin of replication, which is robust  
538 to a remarkable array of cellular perturbations (*Si et al., 2017*). Given the proteomic measurements featured in  
539 this work, it becomes apparent that the ribosome copy number is also scaled in proportion to  $\langle \# \text{ ori} \rangle$  *Figure 10(A)*.  
540 Importantly, however, it will only be due to an increase in  $\Phi_R$  at these moderate to fast growth rates that cells  
541 can achieve an increase in their growth rate. Indeed, we find that the deviations in protein expression with  $\langle \# \text{ ori} \rangle$   
542 are largely restricted to regions of ribosomal protein genes *Figure 10(B)*. Here we have calculated the position-  
543 dependent protein expression across the chromosome by a running Gaussian average of protein copy number  
544 (20 kbp st. dev. averaging window) based on each gene's transcriptional start site. These were median-subtracted  
545 to account for the change in total protein abundance with  $\langle \# \text{ ori} \rangle$ . This result suggests that  $\Phi_R$  is also being tuned  
546 in proportion to  $\langle \# \text{ ori} \rangle$  under nutrient-limited growth, and in particular, it is through this additional dependence  
547 on  $\Phi_R$  that *E. coli* exhibits an exponential increase in cell size with growth rate.

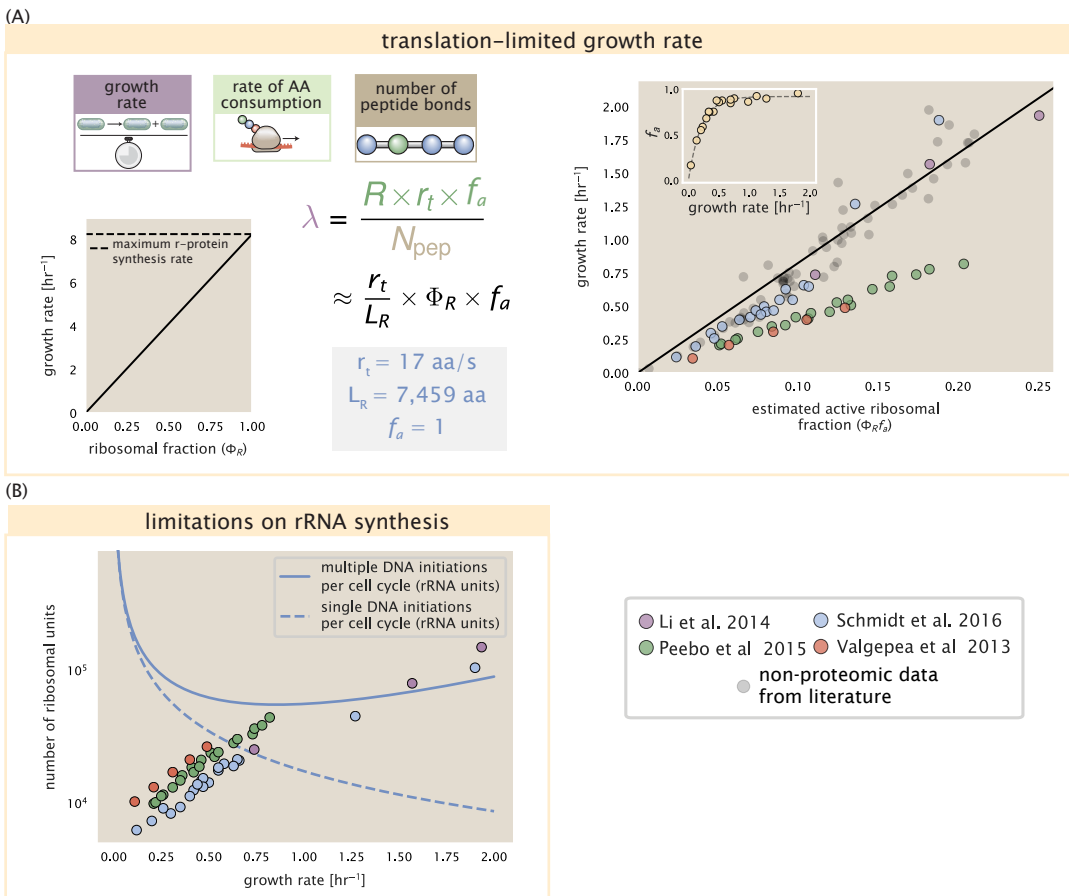


**Figure 9. Translation-limited growth rate.** (A) /left: Translation-limited growth as a function of the ribosomal fraction. The solid line is calculated for an elongation rate of 17 aa per second. The dashed line corresponds to the maximum rate of r-protein synthesis. right: Actively translating ribosomal fraction versus growth rate. The actively translating ribosomal fraction is calculated using the estimated values of  $f_a$  from [Dai et al. \(2016\)](#) (shown in inset; see Appendix Calculation of active ribosomal fraction for additional detail). Gray data points show additional measurements from literature and consider further in [Figure 9–Figure Supplement 1\(A\)](#). (B) Maximum number of rRNA units that can be synthesized as a function of growth rate. Solid curve corresponding to the rRNA copy number is calculated by multiplying the number of rRNA operons by the estimated number of (# ori) at each growth rate. The quantity (# ori) was calculated using Equation 4 and the measurements from [Si et al. \(2017\)](#) that are plotted in [Figure 10\(A\)](#). The dashed line shows the maximal number of functional rRNA units produced from a single chromosomal initiation per cell cycle.

**Figure 9–Figure supplement 1.** Comparison of  $\Phi_R f_a$  with literature and estimation of (# ori).

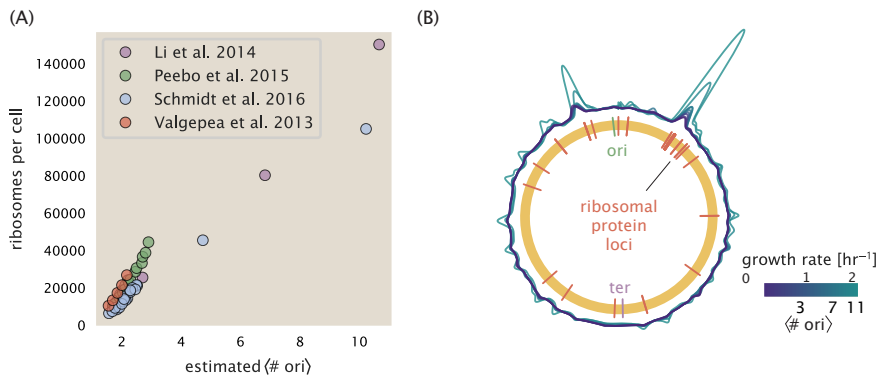


**Figure 10. Cells increase both absolute ribosome abundance and  $\Phi_R$  with (# ori).** (A) Plot of the ribosome copy number estimated from the proteomic data against the estimated (# ori) (see Appendix Estimation of  $\langle \# \text{ori} \rangle / \langle \# \text{ter} \rangle$  and  $\langle \# \text{ori} \rangle$  for additional details). (B) A running Gaussian average (20 kbp st. dev.) of protein copy number is calculated for each growth condition considered by (Schmidt et al., 2016) based on each gene's transcriptional start site. Since total protein abundance increases with growth rate, protein copy numbers are median-subtracted to allow comparison between growth conditions.  $\langle \# \text{ori} \rangle$  are estimated using the data in (A) and Equation 4.

## 548 A Minimal Model of Nutrient-Mediated Growth Rate Control

549 While the preceding subsections highlight a dominant role for ribosomes in setting the growth rate, our analysis  
 550 on the whole emphasizes that the total proteomic content must also change in response to variable growth con-  
 551 ditions and growth rate. In this final section we use a minimal model of growth rate control to better understand  
 552 how this interconnection between ribosomal abundance and total protein influences the observed growth rate.

553 Here we propose that cells modulate their protein abundance in direct response to the availability of nutrients  
 554 in their environment. As noted earlier, bacteria can modulate ribosomal activity through the secondary-messenger  
 555 molecules like (p)ppGpp in poorer nutrient conditions (Figure 9(C) - inset; Dai et al. (2016)). Importantly, these  
 556 secondary-messengers also cause global changes in transcriptional and translational activity (Hauryliuk et al.,  
 557 2015; Zhu and Dai, 2019; Büke et al., 2020). In *E. coli*, amino acid starvation leads to the accumulation of de-  
 558 acylated tRNAs at the ribosome's A-site and a strong increase in (p)ppGpp synthesis activity by the enzyme RelA  
 559 (Hauryliuk et al., 2015). Along with this, there is increasing evidence that (p)ppGpp also acts to inhibit the initiation  
 560 of DNA replication (Kraemer et al., 2019), providing a potential mechanism to lower (# ori) and maintain a smaller  
 561 cell size in poorer growth conditions (Fernández-Coll et al., 2020).

562 To consider this quantitatively, we assume that cells modulate their proteome ( $N_{\text{pep}}$ ,  $R$ ,  $\Phi_R$ ) to better maxi-  
 563 mize their rate of peptide elongation  $r_t$ . The elongation rate  $r_t$  will depend on how quickly the ribosomes can  
 564 match codons with their correct amino-acyl tRNA, along with the subsequent steps of peptide bond formation  
 565 and translocation. This ultimately depends on the cellular concentration amino acids, which we treat as a single  
 566 effective species,  $[AA]_{\text{eff}}$ . In our model, we determine the the rate of peptide elongation  $r_t$  and achievable growth  
 567 rate as simply depending on the supply of amino acids (and, therefore, also amino-acyl tRNAs), through a param-  
 568 eter  $r_{AA}$  in units of AA per second, and the rate of amino acid consumption by protein synthesis ( $r_t \times R \times f_a$ ). This is  
 569 shown schematically in Figure 11(A) and derived in Appendix ???. Given our observation that protein synthesis and  
 570 energy production are not limiting, we assume that other molecular players required by ribosomes like elongation  
 571 factors and GTP are available in sufficient abundance.

572 In Figure 11(B), we illustrate how the elongation rate will depend on the ribosomal copy number. Here, we  
 573 have considered an arbitrarily chosen  $r_{AA} = 5 \times 10^6 \text{ AA} \cdot \text{s}^{-1} \cdot \mu\text{m}^{-3}$  and  $f_a = 1$  for a unit cell volume  $V = 1 \text{ fL}$ .  
 574 At low ribosome copy numbers, the observed elongation rate is dependent primarily on  $[AA]_{\text{eff}}$  through  $r_{AA}$  [as  
 575  $r_t^{\max} \times R \times f_a \ll r_{AA}$ , point (1) in Figure 11(B)]. As the ribosome copy number is increased such that the amino acid  
 576 supply rate and consumption rate are nearly equal [point (2) in Figure 11(B)], the observed elongation rate begins  
 577 to decrease sharply. When the ribosome copy number is increased even further, consumption at the maximum  
 578 elongation rate exceeds the supply rate, yielding a significantly reduced elongation rate [point (3) in Figure 11B)].  
 579 While the elongation rate will always be dominated by the amino acid supply rate at sufficiently low ribosome

(A)

## A MINIMAL MODEL FOR NUTRIENT-LIMITED GROWTH

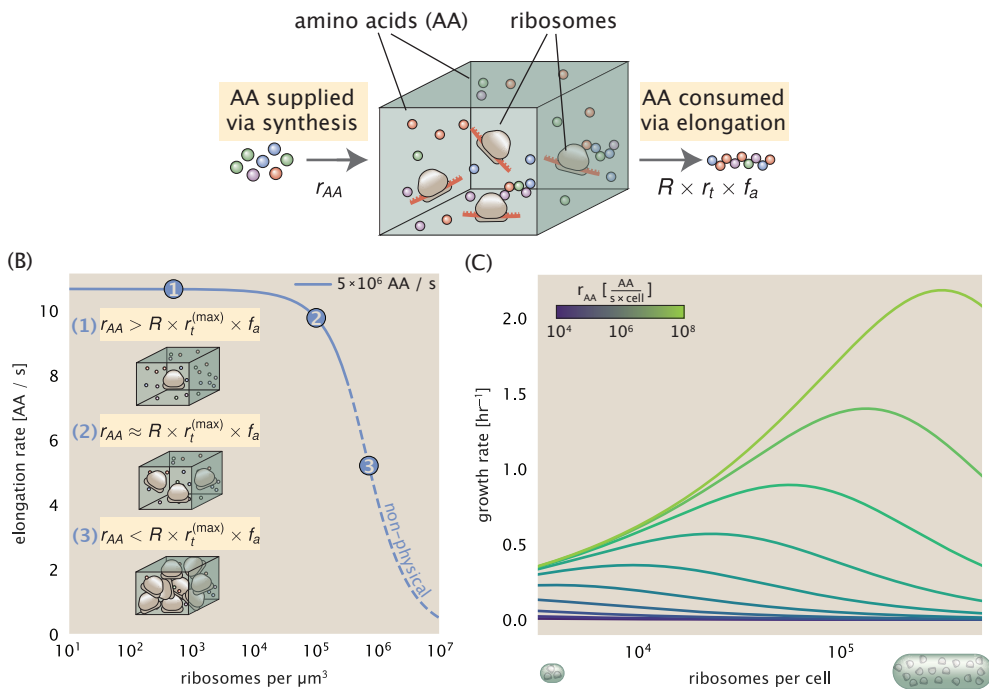


**Figure 11. A minimal model of growth rate control under nutrient limitation.** (A) We consider a unit volume of cellular material composed of amino acids (colored spheres) provided at a supply rate  $r_{AA}$ . These amino acids are polymerized by a pool of ribosomes (brown blobs) at a rate  $r_t \times R \times f_a$ , where  $r_t$  is the elongation rate,  $R$  is the ribosome copy number in the unit volume, and  $f_a$  is the fraction of those ribosomes actively translating. (B) The observed elongation rate is plotted as a function of ribosomes. The three points correspond to three regimes of ribosome copy numbers and are shown schematically on the left-hand side. The region of the curve shown as dashed lines represents a non-physical copy number, but is shown for illustrative purposes. This curve was generated using the parameters  $r_{AA} = 5 \times 10^6 \text{ AA/s}$ ,  $r_t^{(\text{max})} = 17.1 \text{ AA/s}$ ,  $f_a = 1$ , and a unit cell volume of  $V = 1 \mu\text{L}$ . See Appendix ?? for additional model details. (C) The cellular growth rate is plotted as a function of total cellular ribosome copy number for different cellular amino acid supply rates, with blue and green curves corresponding to low and high supply rates, respectively. As the ribosome copy number is increased, so too is the cell size and total protein abundance  $N_{\text{pep}}$ . We direct the reader to the Suppemental Information for discussion on the inference of the realtionship between cell size, number of peptide bonds, and ribosome copy number.

copy numbers, the elongation rate at larger ribosome abundances can be increased by tuning  $f_a$  such that not all ribosomes are elongating, reducing the total consumption rate.

#### Optimal Ribosomal Content and Cell Size Depend on Nutrient Availability and Metabolic Capacity

To relate elongation rate to growth rate, we constrain the set of parameters based on our available proteomic measurements; namely, we restrict the values of  $R$ ,  $N_{\text{pep}}$ , and cell size to those associated with the amalgamated proteomic data (described in Appendix Estimation of Total Protein Content per Cell). We then consider how changes in the nutrient conditions, through the parameter  $r_{AA}$ , influence the maximum growth rate as determined by ???. **Figure 11(C)** shows how the observed growth rate depends on the rate of amino acid supply  $r_{AA}$  as a function of the cellular ribosome copy number. A feature immediately apparent is the presence of a maximal growth rate whose dependence on  $R$  (and consequently, the cell size) increases with increasing  $r_{AA}$ . Importantly, however, there is an optimum set of  $R$ ,  $N_{\text{pep}}$ , and  $V$  that are strictly dependent on the value of  $r_{AA}$ . Increasing the ribosomal concentration beyond the cell's metabolic capacity has the adverse consequence of depleting the supply of amino acids and a concomitant decrease in the elongation rate  $r_t$  [**Figure 11(B)**].

Also of note is the growth rate profiles shown for low amino acid supply rates [purple and blue lines in **Figure 11(C)**], representing growth in nutrient-poor media. In these conditions, there no longer exists a peak in growth, at least in the range of physiologically-relevant ribosome copy numbers. Instead, cells limit their pool of actively translating ribosomes by decreasing  $f_a$  (Dai et al., 2016), which would help maintain the pool of available

597 amino acids [ $AA$ ]<sub>eff</sub> and increase the achievable elongation rate. This observation is in agreement with the central  
598 premise of the cellular resource allocation principle proposed by *Scott et al. (2010); Klumpp et al. (2009); Klumpp*  
599 *and Hwa (2014)* and *Hui et al. (2015)*.

## 600 Discussion

601 Continued experimental and technological improvements have led to a treasure trove of quantitative biological  
602 data (*Hui et al., 2015; Schmidt et al., 2016; Si et al., 2017; Gallagher et al., 2020; Peebo et al., 2015; Valgepea et al.*  
603 *2013*), and an ever advancing molecular view and mechanistic understanding of the constituents that support  
604 bacterial growth (*Taheri-Araghi et al., 2015; Morgenstein et al., 2015; Si et al., 2019; Karr et al., 2012; Kostinski and*  
605 *Reuveni, 2020*). In this work we have compiled what we believe to be the state-of-the-art knowledge on proteomic  
606 copy number across a broad range of growth conditions in *E. coli*. We have made this data accessible through a  
607 [GitHub repository](#), and an interactive figure that allows exploration of specific protein and protein complex copy  
608 numbers. Through a series of order-of-magnitude estimates that traverse key steps in the bacterial cell cycle, this  
609 proteomic data has been a resource to guide our understanding of two key questions: what biological processes  
610 limit the absolute speed limit of bacterial growth, and how do cells alter their molecular constituents as a function  
611 of changes in growth rate or nutrient availability? While not exhaustive, our series of estimates provide insight  
612 on the scales of macromolecular complex abundance across four classes of cellular processes – the transport of  
613 nutrients, the production of energy, the synthesis of the membrane and cell wall, and the numerous steps of the  
614 central dogma.

615 In general, the copy numbers of the complexes involved in these processes were reasonable agreement with  
616 our order-of-magnitude estimates. Since many of these estimates represent soft lower-bound quantities, this  
617 suggests that cells do not express proteins grossly in excess of what is needed for a particular growth rate. Several  
618 exceptions, however, also highlight the dichotomy between a proteome that appears to "optimize" expression  
619 according to growth rate and one that must be able to quickly adapt to environments of different nutritional quality.  
620 Take, for example, the expression of carbon transporters. Shown in *Figure 2(B)*, we find that cells always express  
621 a similar number of glucose transporters irrespective of growth condition. At the same time, it is interesting to  
622 note that many of the alternative carbon transporters are still expressed in low but non-zero numbers ( $\approx 10$ -  
623 100 copies per cell) across growth conditions. This may relate to the regulatory configuration for many of these  
624 operons, which require the presence of a metabolite signal in order for alternative carbon utilization operons to  
625 be induced (*Monod, 1949; Laxhuber et al., 2020*). Furthermore, upon induction, these transporters are expressed  
626 and present in abundances in close agreement with a simple estimate.

627 Of the processes illustrated in *Figure 1*, we arrive at a ribosome-centric view of cellular growth rate control.  
628 This is in some sense unsurprising given the long-held observation that *E. coli* and many other organisms vary  
629 their ribosomal abundance as a function of growth conditions and growth rate (*Scott et al., 2010; Metzl-Raz et al.*  
630 *2017*). However, through our dialogue with the proteomic data, two additional key points emerge. The first relates  
631 to our question of what process sets the absolute speed limit of bacterial growth. While a cell can parallelize  
632 many of its processes simply by increasing the abundance of specific proteins or firing multiple rounds of DNA  
633 replication, this is not so for synthesis of ribosomes (*Figure 9(A)*). The translation time for each ribosome [ $\approx 7$  min,  
634 *Dill et al. (2011)*] places an inherent limit on the growth rate that can only be surpassed if the cell were to increase  
635 their polypeptide elongation rate, or if they could reduce the total protein and rRNA mass of the ribosome. The  
636 second point relates to the long-observed correlations between growth rate and cell size (*Schaechter et al., 1958; Si*  
637 *et al., 2017*), and between growth rate and ribosomal mass fraction. While both trends have sparked tremendous  
638 curiosity and driven substantial amounts of research in their own regards, these relationships are themselves  
639 intertwined. In particular, it is the need for cells to increase their absolute number of ribosomes under conditions  
640 of rapid growth that require cells to also grow in size. Further experiments are needed to test the validity of this  
641 hypothesis. In particular, we believe that the change in growth rate in response to translation-inhibitory drugs  
642 (such as chloramphenicol) could be quantitatively predicted, given one had precision measurement of the relevant  
643 parameters, including the fraction of actively translating ribosomes  $f_a$  and changes in the metabolic capacity of  
644 the cell (i.e. the parameter  $r_{AA}$  in our minimal model) for a particular growth condition.

645 While the generation of new ribosomes plays a dominant role in growth rate control, there exist other physical  
646 limits to the function of cellular processes. One of the key motivations for considering energy production was

647 the physical constraints on total volume and surface area as cells vary their size (*Harris and Theriot, 2018; Ojkic*  
648 *et al., 2019*). While *E. coli* get larger as it expresses more ribosomes, an additional constraint begins to arise in  
649 energy production due to a relative decrease in total surface area where ATP is predominantly produced (*Szenk*  
650 *et al., 2017*). Specifically, the cell interior requires an amount of energy that scales cubically with cell size, but  
651 the available surface area only grows quadratically (*Figure 5(A)*). While this threshold does not appear to be met  
652 for *E. coli* cells growing at 2 hr<sup>-1</sup> or less, it highlights an additional constraint on growth given the apparent need  
653 to increase in cell size to grow faster. This limit is relevant even to eukaryotic organisms, whose mitochondria  
654 exhibit convoluted membrane structures that nevertheless remain bacteria-sized organelles (*Guo et al., 2018*). In  
655 the context of bacteria growth and energy production more generally, we have limited our analysis to the aerobic  
656 growth conditions associated with the proteomic data and further consideration will be needed for anaerobic  
657 growth.

658 This work is by no means meant to be an exhaustive dissection of bacterial growth rate control, and there are  
659 many aspects of the bacterial proteome and growth that we neglected to consider. For example, other recent work  
660 (*Liebermeister et al., 2014; Hui et al., 2015; Schmidt et al., 2016*) has explored how the proteome is structured  
661 and how that structure depends on growth rate. In the work of *Hui et al. (2015)*, the authors coarse-grained the  
662 proteome into six discrete categories being related to either translation, catabolism, anabolism, and others related  
663 to signaling and core metabolism. The relative mass fraction of the proteome occupied by each sector could be  
664 modulated by external application of drugs or simply by changing the nutritional content of the medium. While we  
665 have explored how the quantities of individual complexes are related to cell growth, we acknowledge that higher-  
666 order interactions between groups of complexes or metabolic networks at a systems-level may reveal additional  
667 insights into how these growth-rate dependences are mechanistically achieved. Furthermore, while we anticipate  
668 the conclusions summarized here are applicable to a wide collection of bacteria with similar lifestyles as *E. coli*,  
669 other bacteria and archaea may have evolved other strategies that were not considered. Further experiments  
670 with the level of rigor now possible in *E. coli* will need to be performed in a variety of microbial organisms to learn  
671 more about how regulation of proteomic composition and growth rate control has evolved over the past 3.5 billion  
672 years.

## 673 Methods

### 674 Data Analysis and Availability

675 All proteomic measurements come from the experimental work of *Schmidt et al. (2016); Peebo et al. (2015); Val-*  
676 *gepea et al. (2013)* (mass spectrometry) and *Li et al. (2014)* (ribosomal profiling). Data curation and analysis was  
677 done programmatically in Python, and compiled data and analysis files are accessible through a [GitHub reposi-  
678 tory] (DOI:XXX) associated with this paper as well as on the associated [paper website](#). An interactive figure that  
679 allows exploration of specific protein and protein complex copy numbers is available at [link].

### 680 Acknowledgements

681 We thank Matthias Heinemann, Alexander Schmidt, and Gene-Wei Li for additional input regarding their data. We  
682 also thank members of the Phillips, Theriot, Kondev, and Garcia labs for useful discussions. R.P. is supported by  
683 La Fondation Pierre-Gilles de Gennes, the Rosen Center at Caltech, and the NIH 1R35 GM118043 (MIRA). J.A.T. is  
684 supported by the Howard Hughes Medical Institute, and NIH Grant R37-AI036929. N.M.B is a HHMI Fellow of The  
685 Jane Coffin Childs Memorial Fund.

### 686 Competing Interests

687 The authors declare no competing interests.

# **688 Appendix for: Fundamental limits on the 689 rate of bacterial cell division**

**690 Nathan M. Belliveau<sup>†, 1</sup>, Griffin Chure<sup>†, 2</sup>, Christina L. Hueschen<sup>3</sup>, Hernan G. Garcia<sup>4</sup>, Jane  
691 Kondev<sup>5</sup>, Daniel S. Fisher<sup>6</sup>, Julie A. Theriot<sup>1, 7, \*</sup>, Rob Phillips<sup>8, 9, \*</sup>**

**692** <sup>1</sup>Department of Biology, University of Washington, Seattle, WA, USA; <sup>2</sup>Department of Applied Physics,  
**693** California Institute of Technology, Pasadena, CA, USA; <sup>3</sup>Department of Chemical Engineering,  
**694** Stanford University, Stanford, CA, USA; <sup>4</sup>Department of Molecular Cell Biology and Department of  
**695** Physics, University of California Berkeley, Berkeley, CA, USA; <sup>5</sup>Department of Physics, Brandeis  
**696** University, Waltham, MA, USA; <sup>6</sup>Department of Applied Physics, Stanford University, Stanford, CA,  
**697** USA; <sup>7</sup>Allen Institute for Cell Science, Seattle, WA, USA; <sup>8</sup>Division of Biology and Biological Engineering,  
**698** California Institute of Technology, Pasadena, CA, USA; <sup>9</sup>Department of Physics, California Institute of  
**699** Technology, Pasadena, CA, USA; \*Co-corresponding authors. Address correspondence to  
**700** phillips@pboc.caltech.edu and jtheriot@uw.edu; <sup>†</sup>These authors contributed equally to this work

<b>701</b>	<b>Contents</b>	
<b>702</b>	<b>Introduction</b>	<b>1</b>
<b>703</b>	<b>Nutrient Transport</b>	<b>2</b>
<b>704</b>	Limits on Transporter Expression . . . . .	6
<b>705</b>	<b>Cell Envelope Biogenesis</b>	<b>6</b>
<b>706</b>	Lipid Synthesis . . . . .	6
<b>707</b>	Peptidoglycan Synthesis . . . . .	7
<b>708</b>	Limits on Cell Wall Biogenesis . . . . .	7
<b>709</b>	<b>Energy Production</b>	<b>7</b>
<b>710</b>	ATP Synthesis . . . . .	9
<b>711</b>	Generating the Proton Electrochemical Gradient . . . . .	9
<b>712</b>	Limits on Biosynthesis in a Crowded Membrane . . . . .	11
<b>713</b>	<b>Processes of the Central Dogma</b>	<b>11</b>
<b>714</b>	DNA Replication . . . . .	11
<b>715</b>	RNA Synthesis . . . . .	13
<b>716</b>	Protein Synthesis . . . . .	14
<b>717</b>	Maximum Growth Rate is Determined by the Ribosomal Mass Fraction . . . . .	16
<b>718</b>	rRNA Synthesis Presents a Potential Bottleneck During Rapid Growth . . . . .	18
<b>719</b>	Rapid Growth Requires <i>E. coli</i> to Increase Both Cell Size and Ribosomal Mass Fraction . . . . .	18
<b>720</b>	<b>A Minimal Model of Nutrient-Mediated Growth Rate Control</b>	<b>20</b>
<b>721</b>	Optimal Ribosomal Content and Cell Size Depend on Nutrient Availability and Metabolic Capacity . . . . .	21
<b>722</b>	<b>Discussion</b>	<b>22</b>
<b>723</b>	<b>Methods</b>	<b>23</b>
<b>724</b>	Data Analysis and Availability . . . . .	23
<b>725</b>	<b>Acknowledgements</b>	<b>23</b>
<b>726</b>	<b>Competing Interests</b>	<b>23</b>
<b>727</b>	<b>Experimental Details Behind Proteomic Data</b>	<b>27</b>
<b>728</b>	Fluorescence based measurements . . . . .	27
<b>729</b>	Ribosomal profiling measurements . . . . .	27
<b>730</b>	Mass spectrometry measurements . . . . .	28
<b>731</b>	<b>Summary of Proteomic Data</b>	<b>28</b>
<b>732</b>	<b>Estimation of Cell Size and Surface Area</b>	<b>29</b>
<b>733</b>	<b>Estimation of Total Protein Content per Cell</b>	<b>31</b>
<b>734</b>	Estimating Volume and Number of Amino Acids from Ribosome Copy Number . . . . .	31
<b>735</b>	<b>Additional Considerations of Schmidt <i>et al.</i> Data Set</b>	<b>31</b>
<b>736</b>	Effect of cell volume on reported absolute protein abundances . . . . .	33
<b>737</b>	Relaxing assumption of constant protein concentration across growth conditions . . . . .	35
<b>738</b>	Comparison with total protein measurements from Basan <i>et al.</i> 2015. . . . .	35
<b>739</b>	<b>Calculation of Complex Abundance</b>	<b>36</b>

<b>740</b>	<b>Extending Estimates to a Continuum of Growth Rates</b>	<b>38</b>
741	Estimation of the total cell mass . . . . .	38
742	Complex Abundance Scaling With Cell Volume . . . . .	38
743	A Relation for Complex Abundance Scaling With Surface Area . . . . .	39
744	Number of Lipids . . . . .	39
745	Number of Murein Monomers . . . . .	39
746	Complex Abundance Scaling With Number of Origins, and rRNA Synthesis . . . . .	40
<b>747</b>	<b>Calculation of active ribosomal fraction.</b>	<b>40</b>
<b>748</b>	<b>Estimation of <math>\langle \#ori \rangle / \langle \#ter \rangle</math> and <math>\langle \#ori \rangle</math>.</b>	<b>40</b>

**Table 1.** Overview of proteomic data sets.

Author	Method	Reported Quantity
Taniguchi <i>et al.</i> (2010)	YFP-fusion, cell fluorescence	fg/copies per cell
Valgepea <i>et al.</i> (2012)	mass spectrometry	fg/copies per cell
Peebo <i>et al.</i> (2014)	mass spectrometry	fg/copies per fl
Li <i>et al.</i> (2014)	ribosomal profiling	fg/copies per cell <sup>a</sup>
Soufi <i>et al.</i> (2015)	mass spectrometry	fg/copies per cell
Schmidt <i>et al.</i> (2016)	mass spectrometry	fg/copies per cell <sup>b</sup>

a. The reported values assume that the proteins are long-lived compared to the generation time but are unable to account for post-translational modifications that may alter absolute protein abundances.

b. This mass spectrometry approach differs substantially from the others since in addition to the relative proteome-wide abundance measurements, the authors performed absolute quantification of 41 proteins across all growth conditions (see Section Additional Considerations of Schmidt *et al.* Data Set for more details on this).

## 749 Experimental Details Behind Proteomic Data

750 Here we provide a brief summary of the experiments behind each proteomic data set. The purpose of this section  
751 is to identify how the authors arrived at absolute protein abundances. In the following section (Section Summary  
752 of Proteomic Data) we will then provide a summary of the final protein abundance measurements that were  
753 used throughout the main text. Table 1 provides an overview of the publications we considered. These are pre-  
754 dominately mass spectrometry-based, with the exception of the work from Li *et al.* (2014) which used ribosomal  
755 profiling, and the fluorescence-based counting done in Taniguchi *et al.* (2010).

## 756 Fluorescence based measurements

757 In the work of Taniguchi *et al.* (2010), the authors used a chromosomal YFP fusion library where individual strains  
758 have a specific gene tagged with a YFP-coding sequence. 1018 of their 1400 attempted strains were used in the  
759 work. A fluorescence microscope was used to collect cellular YFP intensities across all these strains. Through au-  
760 tomated image analysis, the authors normalized intensity measurements by cell size to account for the change  
761 in size and expression variability across the cell cycle. Following correction of YFP intensities for cellular autoflu-  
762 orescence, final absolute protein levels were determined by a calibration curve with single-molecule fluorescence  
763 intensities. This calibration experiment was performed separately using a purified YFP solution.

## 764 Ribosomal profiling measurements

765 The work of Li *et al.* (2014) takes a sequencing based approach to estimate protein abundance. Ribosomal pro-  
766 filing, which refers to the deep sequencing of ribosome-protected mRNA fragments, can provide a quantitative  
767 measurement of the protein synthesis rate. As long as the protein life-time is long relative to the cell doubling  
768 time, it is possible to estimate absolute protein copy numbers. The absolute protein synthesis rate has units of  
769 proteins per generation, and for stable proteins will also correspond to the protein copy number per cell.

770 In the experiments, ribosome-protected mRNA is extracted from cell lysate and selected on a denaturing poly-  
771 acrylamide gel for deep sequencing (15–45 nt long fragments collected and sequenced by using an Illumina HiSeq  
772 2000 in Li *et al.* (2014)). Counts of ribosome footprints from the sequencing data were then corrected empiri-  
773 cally for position-dependent biases in ribosomal density across each gene, as well as dependencies on specific  
774 sequences including the Shine-Dalgarno sequence. These data-corrected ribosome densities represent relative  
775 protein synthesis rates. Absolute protein synthesis rates are obtained by multiplying the relative rates by the total  
776 cellular protein per cell. The total protein per unit volume was determined with the Lowry method to quantify  
777 total protein, calibrated against bovine serum albumin (BSA). By counting colony-forming units following serial  
778 dilution of their cell cultures, they then calculated the total protein per cell.

779 **Mass spectrometry measurements**

780 Perhaps not surprisingly, the data is predominantly mass spectrometry based. This is largely due to tremendous  
781 improvements in the sensitivity of mass spectrometers, as well as improvements in sample preparation and data  
782 analysis pipelines. It is now a relatively routine task to extract protein from a cell and quantify the majority of  
783 proteins present by shotgun proteomics. In general, this involves lysing cells, enzymatically digesting the proteins  
784 into short peptide fragments, and then introducing them into the mass spectrometer (e.g. with liquid chromatog-  
785 raphy and electrospray ionization), which itself can have multiple rounds of detection and further fragmentation  
786 of the peptides.

787 Most quantitative experiments rely on labeling protein with stable isotopes, which allow multiple samples to  
788 be measured together by the mass spectrometer. By measuring samples of known total protein abundance simul-  
789 taneously (i.e. one sample of interest, and one reference), it is possible to determine relative protein abundances.  
790 Absolute protein abundances can be estimated following the same approach used above for ribosomal profil-  
791 ing, which is to multiply each relative abundance measurement by the total cellular protein per cell. This is the  
792 approach taken by *Valgepea et al. (2013)* and *Peebo et al. (2015)*, with relative protein abundances determined  
793 based on the relative peptide intensities (label free quantification 'LFQ' intensities). For the data of *Valgepea et al.*  
794 (*2013*), total protein per cell was determined by measuring total protein by the Lowry method, and counting colony-  
795 forming units following serial dilution. For the data from *Peebo et al. (2015)*, the authors did not determine cell  
796 quantities and instead report the cellular protein abundances in protein per unit volume by assuming a mass  
797 density of 1.1 g/ml, with a 30% dry mass fraction.

798 An alternative way to arrive at absolute protein abundances is to dope in synthetic peptide fragments of known  
799 abundance. These can serve as a direct way to calibrate mass spectrometry signal intensities to absolute mass.  
800 This is the approach taken by *Schmidt et al. (2016)*. In addition to a set of shotgun proteomic measurements to  
801 determine proteome-wide relative abundances, the authors also performed absolute quantification of 41 proteins  
802 covering over four orders of magnitude in cellular abundance. Here, a synthetic peptide was generated for each of  
803 the proteins, doped into each protein sample, and used these to determine absolute protein abundances of the 41  
804 proteins. These absolute measurements, determined for every growth condition, were then used as a calibration  
805 curve to convert proteomic-wide relative abundances into absolute protein abundance per cell. A more extensive  
806 discussion of the *Schmidt et al. (2016)* data set can be found in Section Additional Considerations of Schmidt et al.  
807 Data Set.

808 **Summary of Proteomic Data**

809 In the work of the main text we only used the data from *Valgepea et al. (2013)*; *Li et al. (2014)*; *Peebo et al. (2015)*;  
810 *Schmidt et al. (2016)*. As shown in *Figure 12(A)*, the reported total protein abundances in the work of *Taniguchi*  
811 *et al. (2010)* and *Soufi et al. (2015)* differed quite substantially from the other work. For the work of *Taniguchi*  
812 *et al. (2010)* this is in part due to a lower coverage in total proteomic mass quantified, though we also noticed that  
813 most proteins appear undercounted when compared to the other data.

814 *Figure 12(B)* summarizes the total protein mass for each data point in our final compiled data set. We note that  
815 protein abundances were all scaled so they followed a common growth rate-dependent change in total protein  
816 mass. While our inclination initially was to leave reported copy numbers untouched, a notable discrepancy in the  
817 scaling total protein per cell between *Schmidt et al. (2016)* and the other data sets forced us to dig deeper into  
818 those measurements (compare *Schmidt et al. (2016)* and *Li et al. (2014)* data in *Figure 12(A)*). The particular trend  
819 in *Schmidt et al. (2016)* appears to be due to assumptions of cell size and we provide a more extensive discussion  
820 and analysis of that data set in section Additional Considerations of Schmidt et al. Data Set. As a compromise, and  
821 in an effort to treat all data equally, we instead scaled all protein abundance values to a data-driven estimate of  
822 total protein per cell. Here we used cell size measurements from *Si et al. (2017, 2019)*, and an estimate of total  
823 protein content through expected dry mass. Total protein per cell was estimated using available data on total  
824 DNA, RNA, and protein from *Basan et al. (2015)*; *Dai et al. (2016)*, which account for the majority of dry mass in the  
825 cell. We consider these details in sections Estimation of Cell Size and Surface Area and Estimation of Total Protein  
826 Content per Cell that follows.

827 Lastly, in *Figure 13* we show the total proteomic coverage and overlap of proteins quantified across each data

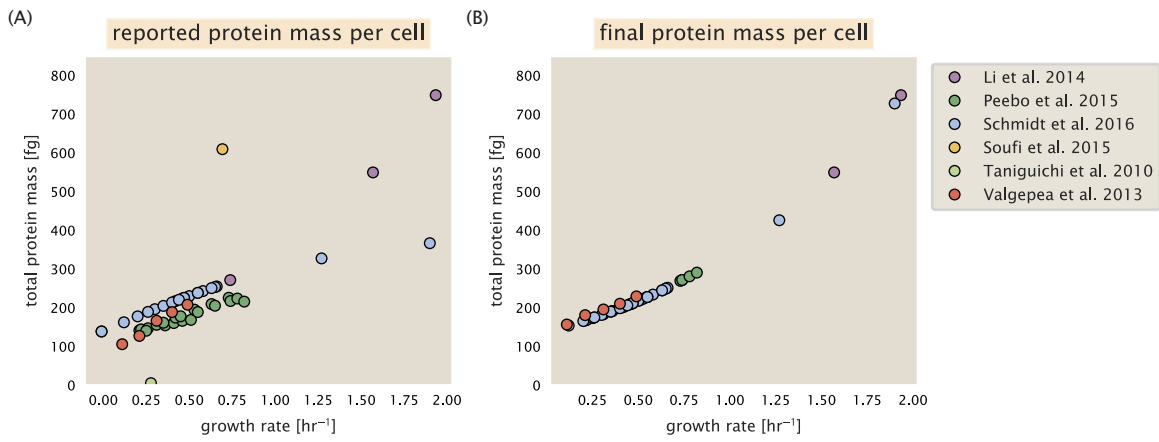


**Figure 12. Summary of the growth-rate dependent total protein abundance for each data set.** (A) Total protein abundance per cell as original reported in the data sets of *Taniguchi et al. (2010)*; *Valgepea et al. (2013)*; *Li et al. (2014)*; *Soufi et al. (2015)*; *Peebo et al. (2015)*; *Schmidt et al. (2016)*. Note that the data from *Peebo et al. (2015)* only reported protein abundances per unit volume and total protein per cell was found by multiplying these by the growth-rate dependent cell size as determined by *Si et al. (2017)*. (B) Adjusted total protein abundances across the proteomic data sets are summarized. Protein abundances were adjusted so that all data shared a common set of growth-rate dependent total protein per cell and cellular protein concentration following the cell size expectations of *Si et al. (2017)* (see section on Estimation of Cell Size and Surface Area for further details).

set. Here we have used an UpSet diagram (*Lex et al., 2014*) to compare the data. Overall, the overlap in quantified proteins is quite high, with 1157 proteins quantified across all data sets. The sequencing based approach of *Li et al. (2014)* has substantially higher coverage compared to the mass spectrometry data sets (3394 genes versus the 2041 genes quantified in the work of *Schmidt et al. (2016)*). However, in terms of total protein mass, the data from *Li et al. (2014)*; *Schmidt et al. (2016)*; *Peebo et al. (2015)* each quantify roughly equivalent total protein mass. An exception to this is in the data from *Valgepea et al. (2013)*, where we find that the total protein quantified in *Valgepea et al. (2013)* is 90-95 % of the total protein mass (when using the data from *Schmidt et al. (2016)* as a reference).

### Estimation of Cell Size and Surface Area

Since most of the proteomic data sets lack cell size (i.e. volume) measurements, we chose instead to use a common estimate of size for any analysis requiring cell size or surface area. Since each of the data sets used either K-12 MG1655 or its derivative, BW25113 (from the lab of Barry L. Wanner; the parent strain of the Keio collection (*Datsenko and Wanner, 2000*; *Baba et al., 2006*)), we fit the MG1655 cell size data from the supplemental material of *Si et al. (2017, 2019)* using the `optimize.curve_fit` function from the Scipy python package (*Virtanen et al., 2020*).

The average size measurements from each of their experiments are shown in Figure *Figure 14*, with cell length and width shown in (A) and (B), respectively. The length data was well described by the exponential function  $0.5 e^{1.09 \cdot \lambda} + 1.76 \mu\text{m}$ , while the width data was well described by  $0.64 e^{0.24 \cdot \lambda} \mu\text{m}$ . In order to estimate cell size we take the cell as a cylinders with two hemispherical ends (*Si et al., 2017*; *Basan et al., 2015*). Specifically, cell size is estimated from,

$$V = \pi \cdot r^2 \cdot (l - 2r/3), \quad (5)$$

where  $r$  is half the cell width. A best fit to the data is described by  $0.533 e^{1.037 \cdot \lambda} \mu\text{m}^3$ . Calculation of the cell surface area is given by,

$$S = \eta \cdot \pi \left( \frac{\eta \cdot \pi}{4} - \frac{\pi}{12} \right)^{-2/3} V^{2/3}, \quad (6)$$

where  $\eta$  is the aspect ratio ( $\eta = l/w$ ) (*Ojkic et al., 2019*).

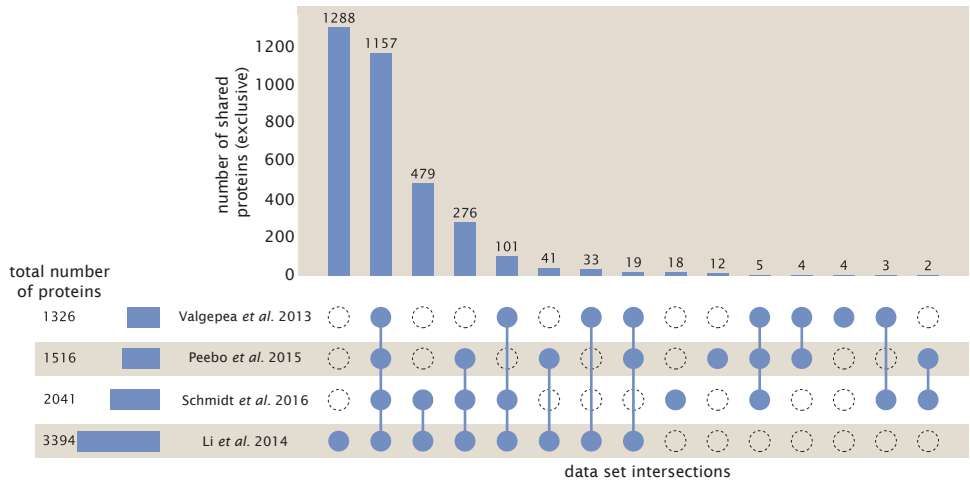


**Figure 13. Comparison of proteomic coverage across different data sets.** An UpSet diagram (*Lex et al., 2014*) summarizes the total number of protein coding genes whose protein abundance was reported in the data sets of *Valgepea et al. (2013); Li et al. (2014); Schmidt et al. (2016); Peebo et al. (2015)*. The total number of genes reported in each individual data set are noted on the bottom left, while their overlap is summarized in the bar chart. Each column here refers to the intersection of a set of data sets identified by blue circles.

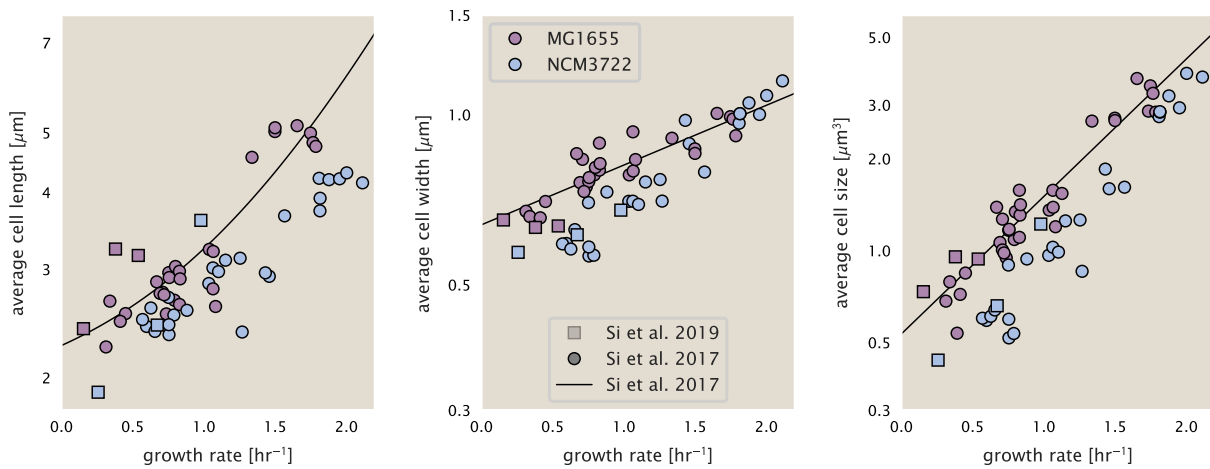


**Figure 14. Summary of size measurements from Si et al. 2017, 2019.** Cell lengths and widths were measured from cell contours obtained from phase contrast images, and refer to the long and short axis respectively. (A) Cell lengths and (B) cell widths show the mean measurements reported (they report 140-300 images and 5,000-30,000 for each set of samples; which likely means about 1,000-5,000 measurements per mean value reported here since they considered about 6 conditions at a time). Fits were made to the MG1655 strain data; length:  $0.5 e^{1.09 \cdot \lambda} + 1.76 \mu\text{m}$ , width:  $0.64 e^{0.24 \cdot \lambda} \mu\text{m}$ . (C) Cell size,  $V$ , was calculated as cylinders with two hemispherical ends (Equation 5). The MG1655 strain data gave a best fit of  $0.533 e^{1.037 \cdot \lambda} \mu\text{m}^3$ .

## 850 Estimation of Total Protein Content per Cell

851 In order to estimate total protein per cell for a particular growth rate, we begin by estimating the cell size from  
852 the fit shown in Figure **Figure 14(C)** ( $0.533 e^{1.037 \cdot \lambda} \mu\text{m}^3$ ). We then estimate the total protein content from the total  
853 dry mass of the cell. Here we begin by noting that for almost the entire range of growth rates considered here,  
854 protein, DNA, and RNA were reported to account for at least 90 % of the dry mass (**Basan et al. (2015)**). The authors  
855 also found that the total dry mass concentration was roughly constant across growth conditions. Under such a  
856 scenario, we can calculate the total dry mass concentration for protein, DNA, and RNA, which is given by 1.1 g/ml  
857  $\times 30\% \times 90\%$  or about  $[M_p] = 300 \text{ fg per fl}$ . Multiplying this by our prediction of cell size gives the total dry mass  
858 per cell.

859 However, even if dry mass concentration is relatively constant across growth conditions, it is not obvious how  
860 protein concentration might vary due to the substantial increase in rRNA at faster growth rates (**Dai et al. (2016)**).  
861 This is a well-documented result that arises from an increase in ribosomal abundance at faster growth rates (**Scott**  
862 **et al. (2010)**). To proceed therefore rely on experimental measurements of total DNA content per cell that also  
863 come from Basan *et al.*, and RNA to protein ratios that were measured in Dai *et al.* (and cover the entire range of  
864 growth conditions considered here). These are reproduced in Figure **Figure 15(A)** and (B), respectively.

865 Assuming that the protein, DNA, and RNA account for 90 % of the total dry mass, the protein mass can then de-  
866 termined by first subtracting the experimentally measured DNA mass, and then using the experimental estimate  
867 of the RNA to protein ratio. The total protein per cell is will be related to the summed RNA and protein mass by,

$$868 M_p = \frac{[M_p + M_{RNA}]}{1 + (RP_{ratio})}. \quad (7)$$

869 ( $RP_{ratio}$  refers to the RNA to protein ratio as measured by Dai *et al.*). In Figure **Figure 15(C)** we plot the estimated  
870 cellular concentrations for protein, DNA, and RNA from these calculations, and in Figure **Figure 15(D)** we plot their  
871 total expected mass per cell. This later quantity is the growth rate-dependent total protein mass that was used to  
872 estimate total protein abundance across all data sets (and summarized in **Figure 12(B)**).

## 872 Estimating Volume and Number of Amino Acids from Ribosome Copy Number

873 Towards the end of the main text, we examine a coarse-grained model of nutrient-limited growth. A key point  
874 in our analysis was to consider how elongation rate  $r_e$  and growth rate  $\lambda$  vary with respect to the experimentally  
875 observed changes in cell size, total number of peptide bonds per cell  $N_{pep}$ , and ribosomal content. In order to  
876 do maintain parameters in line with the experimental data, but otherwise allow us to explore the model, we  
877 performed a phenomenological fit of  $N_{pep}$  and  $V$  as a function of the measured ribosomal copy number  $R$ . As has  
878 been described in the preceding sections of this supplement, we estimate cell volume for each growth condition  
879 using the size measurements from **Si et al. (2017, 2019)**, and  $N_{pep}$  is approximated by taking the total protein mass  
880 and dividing this number by the average mass of an amino acid, 110 Da (BNID: 104877).

881 Given the exponential scaling of  $V$  and  $N_{pep}$  with growth rate, we performed a linear regression of the log trans-  
882 form of these parameters as a function of the log transform of the ribosome copy number. Using optimization  
883 by minimization, we estimated the best-fit values of the intercept and slope for each regression. **Figure 16** shows  
884 the result of each regression as a dashed line.

## 885 Additional Considerations of Schmidt *et al.* Data Set

886 While the data set from **Schmidt et al. (2016)** remains a heroic effort that our labs continue to return to as a  
887 resource, there were steps taken in their calculation of protein copy number that we felt needed further consider-  
888 ation. In particular, the authors made an assumption of constant cellular protein concentration across all growth  
889 conditions and used measurements of cell volume that appear inconsistent with an expected exponential scaling  
890 of cell size with growth rate that is well-documented in *E. coli* (**Schaechter et al. (1958); Taheri-Araghi et al. (2015);**  
891 **Si et al. (2017)**).

892 We begin by looking at their cell volume measurements, which are shown in blue in Figure **Figure 17**. As a  
893 comparison, we also plot cell sizes reported in three other recent papers: measurements from Taheri-Araghi *et*  
894 *al.* and Si *et al.* come from the lab of Suckjoon Jun, while those from Basan *et al.* come from the lab of Terence  
895 Hwa. Each set of measurements used microscopy and cell segmentation to determine the length and width, and

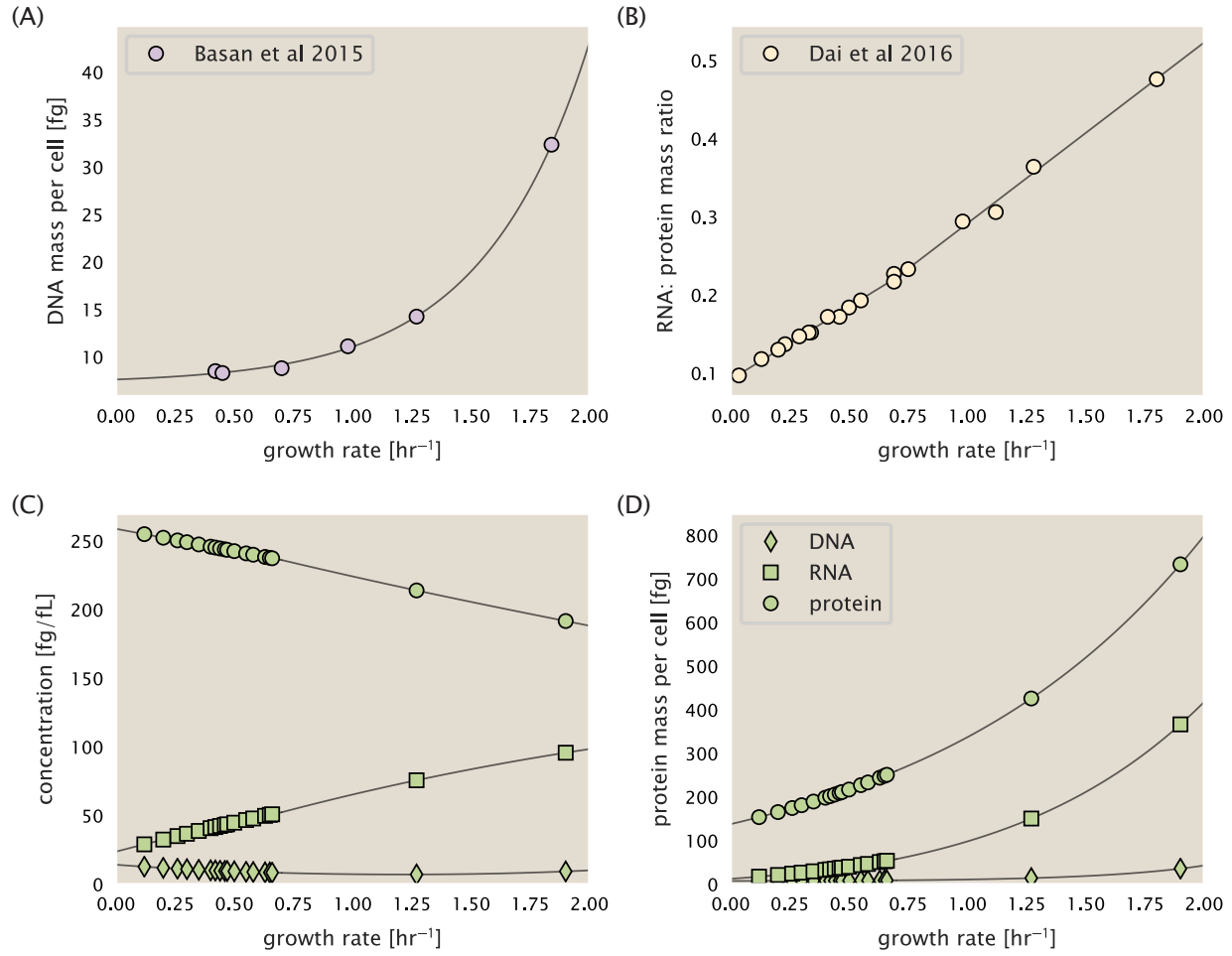


**Figure 15. Empirical estimate of cellular protein, DNA, and RNA as a function of growth rate.** (A) Measured DNA mass per cell as a function of growth rate, reproduced from Basan *et al.* 2015. The data was fit to an exponential curve (DNA mass in fg per cell is given by  $0.42 e^{2.23 \cdot \lambda} + 7.2$  fg per cell, where  $\lambda$  is the growth rate in  $\text{hr}^{-1}$ ). (B) RNA to protein measurements as a function of growth rate. The data was fit to two lines: for growth rates below  $0.7 \text{ hr}^{-1}$ , the RNA/protein ratio is  $0.18 \cdot \lambda + 0.093$ , while for growth rates faster than  $0.7 \text{ hr}^{-1}$  the RNA/protein ratio is given by  $0.25 \cdot \lambda + 0.035$ . For (A) and (B) cells are grown under varying levels of nutrient limitation, with cells grown in minimal media with different carbon sources for the slowest growth conditions, and rich-defined media for fast growth rates. (C) Predictions of cellular protein, DNA, and RNA concentration. (D) Total cellular mass predicted for protein, DNA, and RNA using the cell size predictions from Si *et al.*. Symbols (diamond: DNA, square: RNA, circle: protein) show estimated values of mass concentration and mass per cell for the specific growth rates in Schmidt *et al.* (2016).

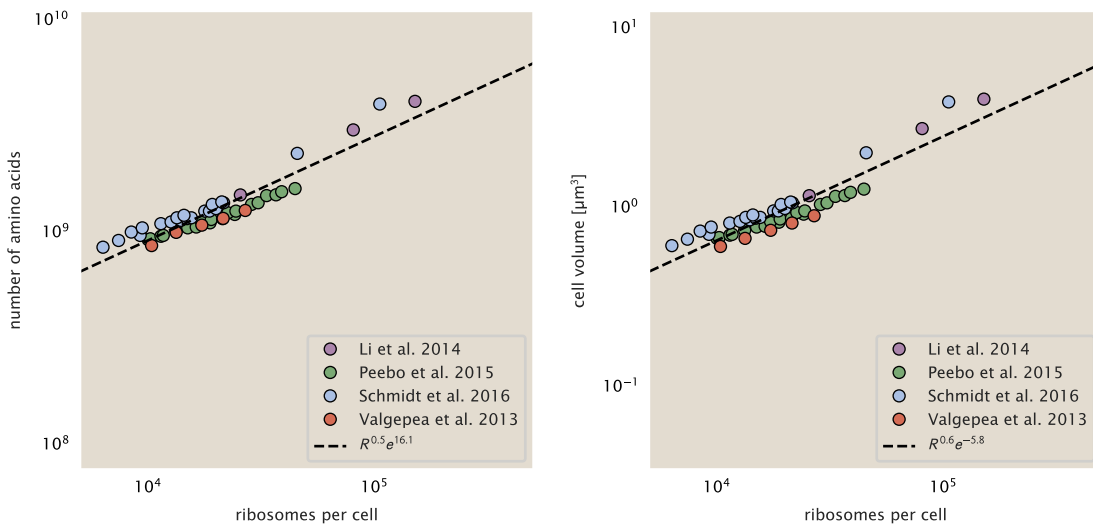


**Figure 16. Phenomenological regression of cell volume and number of amino acids per cell as a function of the ribosome copy number.** Colored points correspond to the measured value (or calculated value in the case of the cell volume) with colors denoting different data sets. The dashed black line shows the result of the fit, with the functional form of the equation given in the legend with  $R$  representing the ribosome copy number.

then calculated cell size by treating the cell as a cylinder with two hemispherical ends, as we considered in the previous section. While there is notable discrepancy between the two research groups, which are both using strain NCM3722, Basan *et al.* found that this came specifically from uncertainty in determining the cell width. This is prone to inaccuracy given the small cell size and optical resolution limits (further described in their supplemental text). Perhaps the more concerning point is that while each of these alternative measurements show an exponential increase in cell size at faster growth rates, the measurements used by Schmidt *et al.* appear to plateau. This resulted in an analogous trend in their final reported total cellular protein per cell as shown in Figure [Figure 18](#) (purple data points), and is in disagreement with other measurements of total protein at these growth rates ([Basan et al., 2015](#)).

Since it is not obvious how measurements of cell size influenced their reported protein abundances, in the following subsections we begin by considering this calculation. We then consider three different approaches to estimate the growth-rate dependent total protein mass to compare with those values reported from Schmidt *et al.* (2016). The results of this are summarized in [Figure 17\(B\)](#), with the original values from both Schmidt *et al.* (2016) and Li *et al.* (2014) shown in [Figure 17\(A\)](#) for reference. For most growth conditions, we find that total protein per cell is still in reasonable agreement. However, for the fastest growth conditions, with glycerol + supplemented amino acids, and LB media, all estimates are substantially higher than those originally reported. This is the main reason why we chose to readjusted protein abundance as shown in [Figure 12\(B\)](#) (with the calculation described in section [Estimation of Total Protein Content per Cell](#)).

#### Effect of cell volume on reported absolute protein abundances

As noted in section [Experimental Details Behind Proteomic Data](#), the authors calculated proteome-wide protein abundances by first determining absolute abundances of 41 pre-selected proteins, which relied on adding synthetic heavy reference peptides into their protein samples at known abundance. This absolute quantitation was performed in replicate for each growth condition. Separately, the authors also performed a more conventional mass spectrometry measurement for samples from each growth condition, which attempted to maximize the number of quantified proteins but only provided relative abundances based on peptide intensities. Finally, using their 41 proteins with absolute abundances already determined, they then created calibration curves with which to relate their relative intensity to absolute protein abundance for each growth condition. This allowed them to estimate absolute protein abundance for all proteins detected in their proteome-wide data set. Combined with

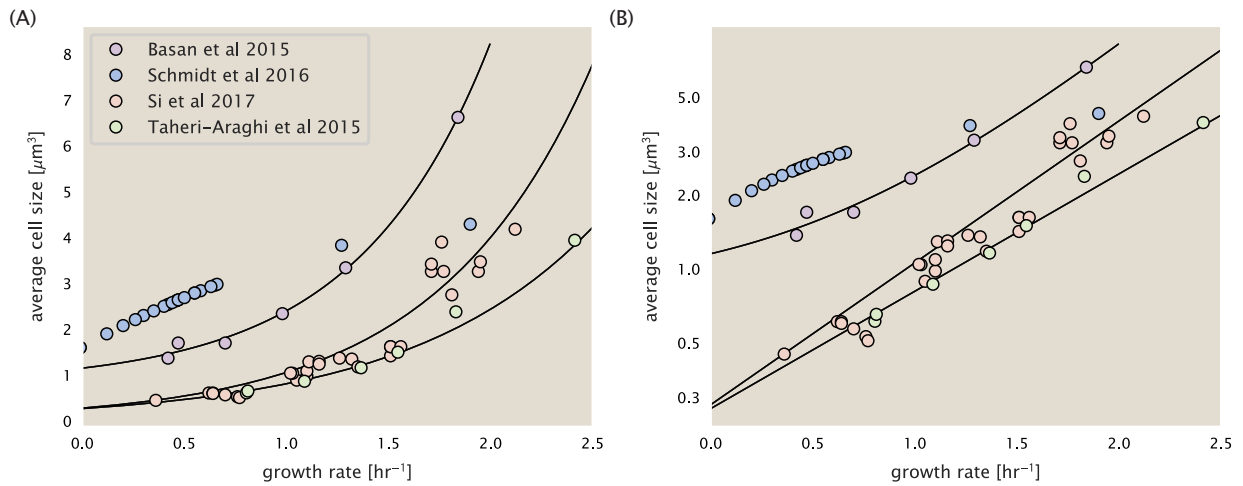


**Figure 17. Measurements of cell size as a function of growth rate.** (A) Plot of the reported cell sizes from several recent papers. The data in blue come from Volkmer and Heinemann, 2011 ([Volkmer and Heinemann \(2011\)](#)) and were used in the work of Schmidt *et al.*. Data from the lab of Terence Hwa are shown in purple ([Basan \*et al.\* \(2015\)](#)), while the two data sets shown in green and red come from the lab of Suckjoon Jun ([Taheri-Araghi \*et al.\* \(2015\); Si \*et al.\* \(2017\)](#)). (B) Same as in (A) but with the data plotted on a logarithmic y-axis to highlight the exponential scaling that is expected for *E. coli*.

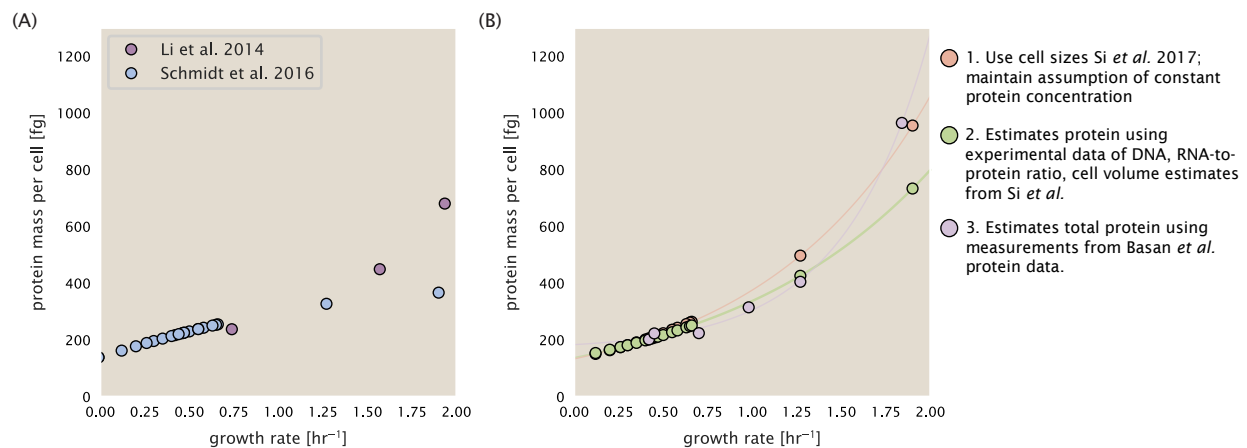


**Figure 18. Alternative estimates of total cellular protein for the growth conditions considered in Schmidt *et al.*** (A) The original protein mass from Schmidt *et al.* and Li *et al.* are shown in purple and blue, respectively. (B) Three alternative estimates of total protein per cell. 1. *light red*: Rescaling of total protein mass assuming a growth rate independent protein concentration and cell volumes estimated from Si *et al.* 2017. 2. *light green*: Rescaling of total protein mass using estimates of growth rate-dependent protein concentrations and cell volumes estimated from Si *et al.* 2017. Total protein per cell is calculated by assuming a 1.1 g/ml cellular mass density, 30% dry mass, with 90% of the dry mass corresponding to DNA, RNA, and protein ([Basan \*et al.\*, 2015](#)). See Estimation of Total Protein Content per Cell for details on calculation. 3. *light purple*: Rescaling of total protein mass using the experimental measurements from Basan *et al.* 2015.

924 their flow cytometry cell counts, they were then able to determine absolute abundance of each protein detected  
925 on a per cell basis.

926 While this approach provided absolute abundances, another necessary step to arrive at total cellular protein  
927 was to account for any protein loss during their various protein extraction steps. Here the authors attempted  
928 to determine total protein separately using a BCA protein assay. In personal communications, it was noted that  
929 determining reasonable total protein abundances by BCA across their array of growth conditions was particularly  
930 troublesome. Instead, they noted confidence in their total protein measurements for cells grown in M9 minimal  
931 media + glucose and used this as a reference point with which to estimate the total protein for all other growth  
932 conditions.

933 For cells grown in M9 minimal media + glucose an average total mass of  $M_p = 240$  fg per cell was measured.  
934 Using their reported cell volume, reported as  $V_{orig} = 2.84$  fl, a cellular protein concentration of  $[M_p]_{orig} = M_p/V_{orig} =$   
935  $85$  fg/fl. Now, taking the assumption that cellular protein concentration is relatively independent of growth rate,  
936 they could then estimate the total protein mass for all other growth conditions from,

$$M_{P\_i} = [M_p]_{orig} \cdot V_i \quad (8)$$

937 where  $M_{P_i}$  represents the total protein mass per cell and  $V_i$  is the cell volume for each growth condition  $i$  as mea-  
938 sured in Volkmer and Heinemann, 2011. Here the thinking is that the values of  $M_{P_i}$  reflects the total cellular protein  
939 for growth condition  $i$ , where any discrepancy from their absolute abundance is assumed to be due to  
940 protein loss during sample preparation. The protein abundances from their absolute abundance measurements  
941 noted above were therefore scaled to their estimates and are shown in Figure **Figure 18** (purple data points).

942 If we instead consider the cell volumes predicted in the work of Si *et al.*, we again need to take growth in M9  
943 minimal media + glucose as a reference with known total mass, but we can follow a similar approach to estimate  
944 total protein mass for all other growth conditions. Letting  $V_{Si\_glu} = 0.6$  fl be the predicted cell volume, the cellular  
945 protein concentration becomes  $[M_p]_{Si} = M_p/V_{Si\_glu} = 400$  fg/fl. The new total protein mass per cell can then be  
946 calculated from,

$$M'_{P\_i} = [M_p]_{Si} \cdot V_{Si\_i} \quad (9)$$

947 where  $M'_{P_i}$  is the new protein mass prediction, and  $V_{Si_i}$  refers to the new volume prediction for each condition  $i$ ,  
948 These are shown as red data points in Figure **Figure 18(B)**.

#### 949 **Relaxing assumption of constant protein concentration across growth conditions**

950 We next relax the assumption that cellular protein concentration is constant and instead, attempt to estimate it  
951 using experimental data. Here we use the estimation of total protein mass per cell detailed in section **Estimation**  
952 of Total Protein Content per Cell for all data points in the **Schmidt *et al.* (2016)** data set. The green data points in  
953 **Figure 18(B)** show this prediction, and this represents the approach used to estimate total protein per cell for all  
954 data sets.

#### 955 **Comparison with total protein measurements from Basan *et al.* 2015.**

956 One of the challenges in our estimates in the preceding sections is the need to estimate protein concentration  
957 and cell volumes. These are inherently difficult to accurately due to the small size of *E. coli*. Indeed, for all  
958 the additional measurements of cell volume included in Figure **Figure 17**, no measurements were performed for  
959 cells growing at rates below  $0.5\text{ hr}^{-1}$ . It therefore remains to be determined whether our extrapolated cell volume  
960 estimates are appropriate, with the possibility that the logarithmic scaling of cell size might break down for slower  
961 growth.

962 In our last approach we therefore attempt to estimate total protein using experimental data that required no  
963 estimates of concentration or cell volume. Specifically, in the work of Basan *et al.*, the authors measured total  
964 protein per cell for a broad range of growth rates (reproduced in Figure **Figure 19**). These were determined by  
965 first measuring bulk protein from cell lysate, measured by the colorimetric Biuret method (**You *et al.* (2013)**), and  
966 then abundance per cell was calculated from cell counts from either plating cells or a Coulter counter. While it  
967 is unclear why Schmidt *et al.* was unable to take a similar approach, the results from Basan *et al* appear more

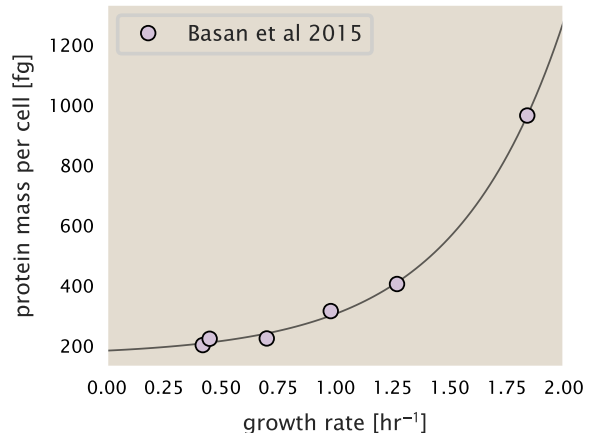


**Figure 19. Total cellular protein reported in Basan et al. 2015.** Measured protein mass as a function of growth rate as reproduced from Basan *et al.* 2015, with cells grown under different levels of nutrient limitation. The data was fit to an exponential curve where protein mass in fg per cell is given by  $14.65 e^{2.180 \cdot \lambda} + 172$  fg per cell, where  $\lambda$  is the growth rate in  $hr^{-1}$ .

consistent with our expectation that cell mass will increase exponentially with faster growth rates. In addition, although they do not consider growth rates below about  $0.5\ hr^{-1}$ , it is interesting to note that the protein mass per cell appears to plateau to a minimum value at slow growth. In contrast, our estimates using cell volume so far have predicted that total protein mass should continue to decrease slightly for slower growing cells. By fitting this data to an exponential function dependent on growth rate, we could then estimate the total protein per cell for each growth condition considered by Schmidt *et al.* (2016). These are plotted as red data points in Figure 18(B).

#### Calculation of Complex Abundance

All protein data quantified the abundance of individual proteins per cell. However, this work requires estimates on the abundance of individual protein *complexes*, rather than the copy number of individual proteins. In this section, we outline the approach we used to annotate proteins as being part of a macromolecular complex and how we computed their absolute abundances per cell.

Protein complexes, and proteins individually, often have a variety of names, both longform and shorthand. As individual proteins can have a variety of different synonyms, we sought to ensure that each protein annotated in the data sets used the same synonym. To do use, we relied heavily on the EcoCyc Genomic Database (Keseler *et al.*, 2017). Each protein in available data sets included an annotation of one of the gene name synonyms as well as an accession ID – either a UniProt or Blattner “b-number”. We programmatically matched up individual accession IDs between the proteins in different data sets. In cases where accession IDs matched but the gene names were different, we manually verified that the gene product was the same between the datasets and chose a single synonym. All code used in the data cleaning and unification procedures can be found on the associated GitHub repository (DOI:XXX) associated with this paper as well as on the associated paper website.

With each protein conforming to a single identification scheme, we then needed to identify the molecular complexes each protein was a member of. Additionally, we needed to identify how many copies of each protein were present in each complex (i.e. the subunit copy number) and compute the estimated abundance complex that accounted for fluctuations in subunit stoichiometry. To map proteins to complexes, we accessed the EcoCyc *E. coli* database Keseler *et al.* (2017) using PathwayTools version 23.0 Karp *et al.* (2019). With a license for PathWay Tools, we mapped each unique protein to its annotated complexes via the BioCyc Python package. As we mapped each protein with *all* of its complex annotations, there was redundancy in the dataset. For example, ribosomal protein L20 (RplT) is annotated to be a component of the 50S ribosome (EcoCyc complex CPLX-03962) as well as a component of the mature 70S ribosome (EcoCyc complex CPLX-03964).

In addition to the annotated complex, we collected information on the stoichiometry of each macromolecular complex. For a complex with  $N_{subunits}$  protein species, for each protein subunit  $i$  we first calculate the number of

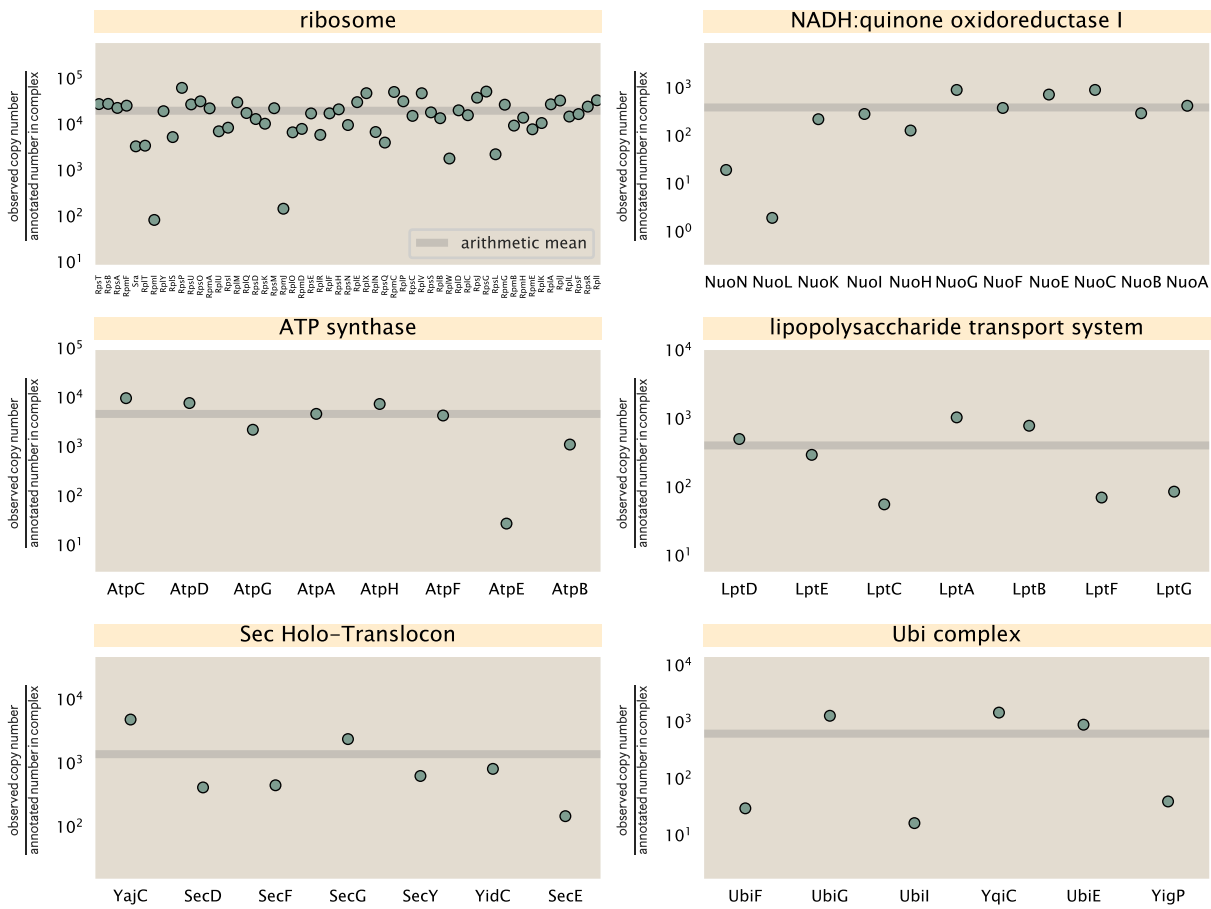


**Figure 20. Calculation of the mean complex abundance from measurements of single subunits.** Six of the largest complexes (by number of subunits) in *E. coli*. Points correspond to the maximum number of complexes that can be formed given measurement of that individual protein. Solid grey line corresponds to the arithmetic mean across all subunits. These data correspond to measurements from Schmidt et al. (2016) in a glucose-supplemented minimal growth medium.

complexes that could be formed given the measured protein copy numbers per cell,

$$N_{\text{complex}}(\text{subunit } i) = \frac{P_{\text{subunit } i}^{(\text{measured})}}{m_{\text{subunit } i}}. \quad (10)$$

Here,  $P_{\text{subunit } i}^{(\text{measured})}$  refers to the measured protein copy number of species  $i$ , and  $m$  refers to the number of monomers present for that protein in the complex. For example, the 70S mature ribosome complex has 55 protein components, all of which are present in a single copy except L4 (RplL), which is present in 4 copies ( $m = 4$ ). For each ribosomal protein, we then calculate the maximum number of complexes that could be formed using Equation 10. This example, along with example from 5 other macromolecular complexes, can be seen in Figure 20.

It is important to note that measurement noise, efficiency of protein extraction, and differences in protein stability will mean that the precise value of each calculation will be different for each component of a given complex. Thus, to report the total complex abundance, we use the arithmetic mean of across all subunits in the complex,

$$\langle N_{\text{complex}} \rangle = \frac{1}{N_{\text{subunits}}} \sum_i^{N_{\text{subunits}}} \frac{P_i^{(\text{measured})}}{m_{\text{subunit } i}}. \quad (11)$$

in Figure 20, we show this mean value as a grey line for a variety of different complexes. Additionally, we have built an interactive figure accessible on the [paper website](#) where the validity of this approach can be examined for any complex with more than two subunits (thus, excluding monomers and dimers).

1011 **Extending Estimates to a Continuum of Growth Rates**

1012 In the main text, we considered a standard stopwatch of 5000 s to estimate the abundance of the various protein  
1013 complexes considered. In addition to point estimates, we also showed the estimate as a function of growth rate  
1014 as transparent grey curves. In this section, we elaborate on this continuum estimate, giving examples of estimates  
1015 that scale with either cell volume, cell surface area, or number of origins of replication.

1016 **Estimation of the total cell mass**

1017 For many of the processes estimated in the main text we relied on a cellular dry mass of  $\approx 300$  fg from which we  
1018 computed elemental and protein fractions using knowledge of fractional composition of the dry mass. At modest  
1019 growth rates, such as the 5000 s doubling time used in the main text, this is a reasonable number to use as the  
1020 typical cell mass is  $\approx 1$  pg and *E. coli* cells can approximated as 70% water by volume. However, as we have shown  
1021 in the preceding sections, the cell size is highly dependent on the growth rate. This means that a dry mass of 300  
1022 fg cannot be used reliably across all growth rates.

1023 Rather, using the phenomenological description of cell volume scaling exponentially with growth rate, and  
1024 using a rule-of-thumb of a cell buoyant density of  $\approx 1.1$  pg / fL (BNID: 103875), we can calculate the cell dry mass  
1025 across a range of physiological growth rates as

$$m_{\text{cell}} \approx \rho V(\lambda) \approx \rho a e^{\lambda * b} \quad (12)$$

1026 where  $a$  and  $b$  are constants with units of  $\mu\text{m}^3$  and hr, respectively. The value of these constants can be estimated  
1027 from the careful volume measurements performed by *Si et al. (2017,?)*, as considered in Appendix Estimation of  
1028 Cell Size and Surface Area earlier.

1029 **Complex Abundance Scaling With Cell Volume**

1030 Several of the estimates performed in the main text are implicitly dependent on the cell volume. This includes  
1031 processes such as ATP utilization and, most prominently, the transport of nutrients, whose demand will be pro-  
1032 portional to the volume of the cell. Of the latter, we estimated the number of transporters that would be needed  
1033 to shuttle enough carbon, phosphorus, and sulfur across the membrane to build new cell mass. To do so, we  
1034 used elemental composition measurements combined with a 300 fg cell dry mass to make the point estimate. As  
1035 we now have a means to estimate the total cell mass as a function of volume, we can generalize these estimates  
1036 across growth rates.

1037 Rather than discussing the particular details of each transport system, we will derive this scaling expression in  
1038 very general terms. Consider that we wish to estimate the number of transporters for some substance  $X$ , which  
1039 has been measured to be made up some fraction of the dry mass,  $\theta_X$ . If we assume that, irrespective of growth  
1040 rate, the cell dry mass is relatively constant (*Basan et al., 2015*) and  $\approx 30\%$  of the total cell mass, we can state that  
1041 the total mass of substance  $X$  as a function of growth rate is

$$m_X \approx 0.3 \times \rho V(\lambda) \theta_X, \quad (13)$$

1042 where we have used  $\rho V(\lambda)$  as an estimate of the total cell mass, defined in *Equation 12*. To convert this to the  
1043 number of units  $N_X$  of substance  $X$  in the cell, we can use the formula weight  $w_X$  of a single unit of  $X$  in conjunction  
1044 with *Equation 13*,

$$N_X \approx \frac{m_X}{w_X}. \quad (14)$$

1045 To estimate the number of transporters needed, we make the approximation that loss of units of  $X$  via diffusion  
1046 through porins or due to the permeability of the membrane is negligible and that a single transporter complex  
1047 can transport substance  $X$  at a rate  $r_X$ . As this rate  $r_X$  is in units of  $X$  per time per transporter, we must provide  
1048 a time window over which the transport process can occur. This is related to the cell doubling time  $\tau$ , which can  
1049 be calculated from the the growth rate  $\lambda$  as  $\tau = \log(2)/\lambda$ . Putting everything together, we arrive at a generalized  
1050 transport scaling relation of

$$N_{\text{transporters}}(\lambda) = \frac{0.3 \times \rho V(\lambda) \theta_X}{w_X r_X \tau}. \quad (15)$$

1051 This function is used to draw the continuum estimates for the number of transporters seen in Figures 2 and  
 1052 3 as transparent grey curves. Occasionally, this continuum scaling relationship will not precisely agree with the  
 1053 point estimate outlined in the main text. This is due to the choice of  $\approx 300$  fg total dry mass per cell for the point  
 1054 estimate, whereas we considered more precise values of cell mass in the continuum estimate. We note, however,  
 1055 that both this scaling relation and the point estimates are meant to describe the order-of-magnitude observed,  
 1056 and not the predict the exact values of the abundances.

1057 **Equation 15** is a very general relation for processes where the cell volume is the "natural variable" of the  
 1058 problem. This means that, as the cell increases in volume, the requirements for substance  $X$  also scale with  
 1059 volume rather than scaling with surface area, for example. So long as the rate of the process, the fraction of the  
 1060 dry mass attributable to the substance, and the formula mass of the substance is known, **Equation 15** can be used  
 1061 to compute the number of complexes needed. For example, to compute the number of ATP synthases per cell,  
 1062 **Equation 15** can be slightly modified to the form

$$N_{\text{ATP synthases}}(\lambda) = \frac{0.3 \times \rho V(\lambda) \theta_{\text{protein}} N_{\text{ATP}}}{w_{AA} r_{\text{ATP}} \tau}, \quad (16)$$

1063 where we have included the term  $N_{\text{ATP}}$  to account for the number of ATP equivalents needed per amino acid for  
 1064 translation ( $\approx 4$ , BNID: 114971), and  $w_{AA}$  is the average mass of an amino acid. The grey curves in Figure 4 o the  
 1065 main text were made using this type of expression.

## 1066 A Relation for Complex Abundance Scaling With Surface Area

1067 In our estimation for the number of complexes needed for lipid synthesis and peptidoglycan maturation, we used  
 1068 a particular estimate for the cell surface area ( $\approx 5 \mu\text{m}$ , BNID: 101792) and the fraction of dry mass attributable to  
 1069 peptidoglycan ( $\approx 3\%$ , BNID: 101936). Both of these values come from glucose-fed *E. coli* in balance growth. As we  
 1070 are interested in describing the scaling as a function of the growth rate, we must also consider how these values  
 1071 scale with cell surface area, which is the natural variable for these types of processes. In the coming paragraphs,  
 1072 we highlight how we incorporate a condition-dependent surface area into our calculation of the number of lipids  
 1073 and murein monomers that need to be synthesized and crosslinked, respectively.

### 1074 Number of Lipids

1075 To compute the number of lipids as a function of growth rate, we make the assumption that some features, such as  
 1076 the surface area of a single lipid ( $A_{\text{lipid}} \approx 0.5 \text{ nm}^2$ , BNID: 106993) and the total fraction of the membrane composed  
 1077 of lipids ( $\approx 40\%$ , BNID: 100078) are independent of the growth rate. Using these approximations combined with  
 1078 **Equation 6**, and recognizing that each membrane is composed of two leaflets, we can compute the number of  
 1079 lipids as a function of growth rate as

$$N_{\text{lipids}}(\lambda) \approx \frac{4 \text{ leaflets} \times 0.4 \times \eta \pi \left( \frac{\eta \pi}{4} - \frac{\pi}{12} \right)^{-2/3} V(\lambda)^{2/3}}{A_{\text{lipid}}} \quad (17)$$

1080 where  $\eta$  is the length-to-width aspect ratio and  $V$  is the cell volume.

### 1081 Number of Murein Monomers

1082 In calculation of the number of transpeptidases needed for maturation of the peptidoglycan, we used an empirical  
 1083 measurement that  $\approx 3\%$  of the dry mass is attributable to peptidoglycan and that a single murien monomer is  
 1084  $m_{\text{murein}} \approx 1000 \text{ Da}$ . While the latter is independent of growth rate, the former is not. As the peptidoglycan exists as  
 1085 a thin shell with a width of  $w \approx 10 \text{ nm}$  encapsulating the cell, one would expect the number of murein monomers  
 1086 scales with the surface area of this shell. In a similar spirit to our calculation of the number of lipids, the total  
 1087 number of murein monomers as a function of growth rate can be calculated as

$$N_{\text{murein monomers}}(\lambda) \approx \frac{\rho_{\text{pg}} w \eta \pi \left( \frac{\eta \pi}{4} - \frac{\pi}{12} \right)^{-2/3} V(\lambda)^{2/3}}{m_{\text{murein}}}, \quad (18)$$

1088 where  $\rho_{\text{pg}}$  is the density of peptidoglycan.

1089 **Complex Abundance Scaling With Number of Origins, and rRNA Synthesis**

1090 While the majority of our estimates hinge on the total cell volume or surface area, processes related to the central  
1091 dogma, namely DNA replication and synthesis of rRNA, depend on the number of chromosomes present in the  
1092 cell. As discussed in the main text, the ability of *E. coli* to parallelize the replication of its chromosome by having  
1093 multiple active origins of replication is critical to synthesize enough rRNA, especially at fast growth rates. Derived  
1094 in *Si et al. (2017)* and reproduced in the main text and Appendix Estimation of  $\langle \#ori \rangle / \langle \#ter \rangle$  and  $\langle \#ori \rangle$  below, the  
1095 average number of origins of replication at a given growth rate can be calculated as

$$\langle \#ori \rangle \approx 2^{t_{\text{cyc}} \lambda / \ln 2} \quad (19)$$

1096 where  $t_{\text{cyc}}$  is the total time of replication and division. We can make the approximation that  $t_{\text{cyc}} \approx 70$  min, which is  
1097 the time it takes two replisomes to copy an entire chromosome.

1098 In the case of rRNA synthesis, the majority of the rRNA operons are surrounding the origin of replication. Thus,  
1099 at a given growth rate  $\lambda$ , the average dosage of rRNA operons per cell  $D_{\text{rRNA}}$  is

$$D_{\text{rRNA}}(\lambda) \approx N_{\text{rRNA operons}} \times 2^{t_{\text{cyc}} \lambda / \ln 2}. \quad (20)$$

1100 This makes the approximation that *all* rRNA operons are localized around the origin. In reality, the operons  
1101 are some distance away from the origin, making **Equation 20** an approximation (*Dennis et al., 2004*).

1102 In the main text, we stated that at a growth rate of  $0.5 \text{ hr}^{-1}$ , there is  $\approx 1$  chromosome per cell. While a fair  
1103 approximation, **Equation 19** illustrates that is not precisely true, even at slow growth rates. In estimating the  
1104 number of RNA polymerases as a function of growth rate, we consider that regardless of the number of rRNA  
1105 operons, they are all sufficiently loaded with RNA polymerase such that each operon produces one rRNA per  
1106 second. Thus, the total number of RNA polymerase as a function of the growth rate can be calculated as

$$N_{\text{RNA polymerase}}(\lambda) \approx L_{\text{operon}} D_{\text{rRNA}} \rho_{\text{RNA polymerase}}, \quad (21)$$

1107 where  $L_{\text{operon}}$  is the total length of an rRNA operon ( $\approx 4500$  bp) and  $\rho_{\text{RNA polymerase}}$  is packing density of RNA poly-  
1108 merase on a given operon, taken to be 1 RNA polymerase per 80 nucleotides.

1109 **Calculation of active ribosomal fraction.**

1110 In the main text we used the active ribosomal fraction  $f_a$  that was reported in the work of *Dai et al. (2016)* to  
1111 estimate the active ribosomal mass fraction  $\Phi_R \times f_a$  across growth conditions. We lacked any specific model to  
1112 consider how  $f_a$  should vary with growth rate, and instead find that the data is well-approximated by fitting to an  
1113 exponential curve ( $f_a = -0.889 e^{4.6 \cdot \lambda} + 0.922$ ; dashed line in inset of **Figure 9(C)**). We use this function to estimate  $f_a$   
1114 for each of the data points shown in **Figure 9(C)**.

1115 **Estimation of  $\langle \#ori \rangle / \langle \#ter \rangle$  and  $\langle \#ori \rangle$ .**

1116 *E. coli* shows robust scaling of cell size with the average the number of origins  $\langle \#ori \rangle$  per cell (*Si et al., 2017*). Since  
1117 protein makes up a majority of the cell's dry mass, the change in cell size is also a reflection of the changes in  
1118 proteomic composition and total abundance across growth conditions. Given the potential constraints on rRNA  
1119 synthesis and changes in ribosomal copy number with  $\langle \#ori \rangle$ , it becomes important to also consider how pro-  
1120 tein copy numbers vary with the state of chromosomal replication. This is particularly true when trying to make  
1121 sense of the changes in ribosomal fraction and growth-rate dependent changes in proteomic composition at a  
1122 mechanistic level. As considered in the main text, it is becoming increasingly apparent that regulation through  
1123 the secondary messengers (p)ppGpp may act to limit DNA replication and also reduce ribosomal activity in poorer  
1124 nutrient conditions. In this context, both  $\langle \#ori \rangle$ , as well as the  $\langle \#ori \rangle / \langle \#ter \rangle$  ratio become important parameters  
1125 to consider and keep tract of. An increase in  $\langle \#ori \rangle / \langle \#ter \rangle$  ratio in particular, causes a relatively higher gene  
1126 dosage in rRNA and r-protein genes due to skew in genes near the origin, where the majority of these are located

1127 In the main text we estimated the change in  $\langle \#ori \rangle$  with growth rate using the nutrient-limited wild-type cell  
1128 data from *Si et al. (2017)*. We consider their measurements of DNA replication time ( $t_C$ , 'C' period of cell division),  
1129 total cell cycle time ( $t_{\text{cyc}}$ , 'C' + 'D' period of cell division), and doubling time  $\tau$  from wild-type *E. coli* growing across  
1130 a range of growth conditions. Here we show how we estimate this parameter, as well as the  $\langle \#ori \rangle / \langle \#ter \rangle$  ratio

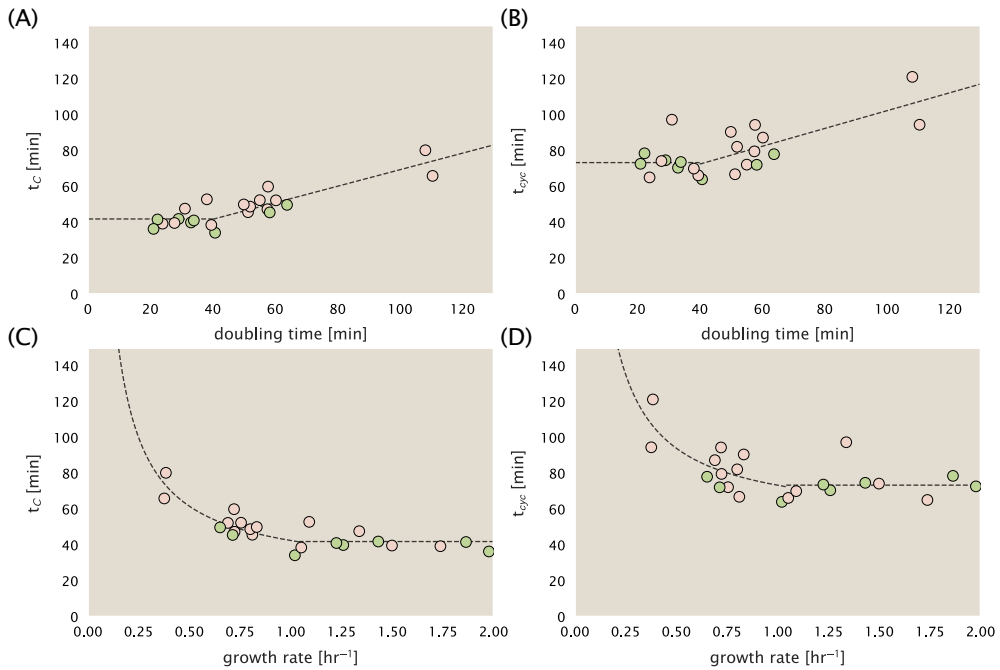


**Figure 21. Estimation of  $\langle \#ori \rangle / \langle \# ter \rangle$  and  $\langle \#ori \rangle$  using data from Si et al. (2017).** (A) and (B) plot the reported  $t_C$  and  $t_{cyc}$  as a function of cell doubling time  $\tau$ , respectively. The dashed lines show a piecewise fit to the data. For short doubling times (rich media),  $t_C$  and  $t_{cyc}$  are assumed constant ( $t_C = 42$  minutes,  $t_{cyc} = 73$  minutes). At the transition, taken to occur at 40 minutes, the dashed line corresponds to an assumed proportional increase in each parameter as a function of the doubling time ( $t_C = 0.46\tau + 23.3$  minutes,  $t_{cyc} = 0.50\tau + 52.7$  minutes). (C) and (D) plot the same data as in (A) and (B), but as a function of growth rate, given by  $\lambda = \ln(2)/\tau$ .

from their data. We begin by considering  $\langle \#ori \rangle$ . If the cell cycle time takes longer than the time of cell division, the cell will need to initiate DNA replication more often than its rate of division,  $2^{\lambda t} = 2^{\ln(2)\cdot t/\tau}$  to maintain steady state growth. Cells will need to do this in proportion to the ratio  $\lambda_{cyc}/\lambda = t_{cyc}/\tau$ , and the number of origins per cell (on average) is then given by  $2^{t_{cyc}/\tau}$ . The average number of termini will in contrast depend on the lag time between DNA replication and cell division,  $t_D$ , with  $\langle \#ori \rangle / \langle \# ter \rangle$  ratio =  $2^{t_{cyc}/\tau - t_D/\tau} = 2^{t_C/\tau}$ .

In Figure 21(A) and (B) we plot the measured  $t_C$  and  $t_{cyc}$  values versus the doubling time from Si et al. (2017). The authors estimated  $t_C$  by marker frequency analysis using qPCR, while  $t_{cyc} = t_C + t_D$  were inferred from  $t_C$  and  $\tau$ . In the plots we see that both  $t_C$  and  $t_{cyc}$  reach a minimum at around 40 and 75 minutes, respectively. For a C period of 40 minutes, this would correspond to a maximum rate of elongation of about 1,000 bp/sec. Since we lacked a specific model to describe how each of these parameters vary with growth condition, we assumed that they were linearly dependent on the doubling time. For each parameter,  $t_C$  and  $t_{cyc}$ , we split them up into two domains corresponding to poorer nutrient conditions and rich nutrient conditions (cut off at  $\tau \approx 40$  minutes where chromosomal replication becomes nearly constant). The fit lines are shown as solid black lines. In Figure 21(C) and (D) we also show  $t_C$  and  $t_{cyc}$  as a function of growth rate  $\lambda$  along with our piecewise linear fits, which match the plots in the main text.

1146 **References**

- 1147 Aidelberg, G., Towbin, B. D., Rothschild, D., Dekel, E., Bren, A., and Alon, U. (2014). Hierarchy of non-glucose sugars in *Escherichia coli*. *BMC Systems Biology*, 8(1):133.
- 1149 Antonenko, Y. N., Pohl, P., and Denisov, G. A. (1997). Permeation of ammonia across bilayer lipid membranes studied by ammonium ion selective microelectrodes. *Biophysical Journal*, 72(5):2187–2195.
- 1151 Ashburner, M., Ball, C. A., Blake, J. A., Botstein, D., Butler, H., Cherry, J. M., Davis, A. P., Dolinski, K., Dwight, S. S., Eppig, J. T., Harris, M. A., Hill, D. P., Issel-Tarver, L., Kasarskis, A., Lewis, S., Matese, J. C., Richardson, J. E., Ringwald, M., Rubin, G. M., and Sherlock, G. (2000). Gene Ontology: tool for the unification of biology. *Nature Genetics*, 25(1):25–29.
- 1154 Ason, B., Bertram, J. G., Hingorani, M. M., Beechem, J. M., O'Donnell, M., Goodman, M. F., and Bloom, L. B. (2000). A Model for *Escherichia coli* DNA Polymerase III Holoenzyme Assembly at Primer/Template Ends: DNA Triggers A Change In Binding Specificity of the  $\gamma$  Complex Clamp Loader. *Journal of Biological Chemistry*, 275(4):3006–3015.
- 1157 Assentoft, M., Kaptan, S., Schneider, H.-P., Deitmer, J. W., de Groot, B. L., and MacAulay, N. (2016). Aquaporin 4 as a NH<sub>3</sub> Channel. *Journal of Biological Chemistry*, 291(36):19184–19195.
- 1159 Baba, T., Ara, T., Hasegawa, M., Takai, Y., Okumura, Y., Baba, M., Datsenko, K. A., Tomita, M., Wanner, B. L., and Mori, H. (2006). Construction of *Escherichia coli*K-12 in-frame, single-gene knockout mutants: the Keio collection. *Molecular Systems Biology*, 2(1):2460.
- 1162 Basan, M., Zhu, M., Dai, X., Warren, M., Sévin, D., Wang, Y.-P., and Hwa, T. (2015). Inflating bacterial cells by increased protein synthesis. *Molecular Systems Biology*, 11(10):836.
- 1164 Bauer, S. and Ziv, E. (1976). Dense growth of aerobic bacteria in a bench-scale fermentor. *Biotechnology and Bioengineering*, 18(1):81–94. \_eprint: <https://onlinelibrary.wiley.com/doi/pdf/10.1002/bit.260180107>.
- 1166 Belliveau, N. M., Barnes, S. L., Ireland, W. T., Jones, D. L., Sweredoski, M. J., Moradian, A., Hess, S., Kinney, J. B., and Phillips, R. (2018). Systematic approach for dissecting the molecular mechanisms of transcriptional regulation in bacteria. *Proceedings of the National Academy of Sciences*, 115(21):E4796–E4805.
- 1169 Bremer, H. and Dennis, P. P. (2008). Modulation of Chemical Composition and Other Parameters of the Cell at Different Exponential Growth Rates. *EcoSal Plus*, 3(1).
- 1171 Browning, D. F. and Busby, S. J. W. (2016). Local and global regulation of transcription initiation in bacteria. *Nature Reviews Microbiology*, 14(10):638–650.
- 1173 Büke, F., Grilli, J., Lagomarsino, M. C., Bokinsky, G., and Tans, S. (2020). ppGpp is a bacterial cell size regulator. *bioRxiv*, 266:2020.06.16.154187.
- 1175 Catherwood, A. C., Lloyd, A. J., Tod, J. A., Chauhan, S., Slade, S. E., Walkowiak, G. P., Galley, N. F., Punekar, A. S., Smart, K., Rea, D., Evans, N. D., Chappell, M. J., Roper, D. I., and Dowson, C. G. (2020). Substrate and Stereochemical Control of Peptidoglycan Cross-Linking by Transpeptidation by *Escherichia coli* PBP1B. *Journal of the American Chemical Society*, 142(11):5034–5048.
- 1178 Cox, G. B., Newton, N. A., Gibson, F., Snoswell, A. M., and Hamilton, J. A. (1970). The function of ubiquinone in *Escherichia coli*. *Biochemical Journal*, 117(3):551–562.
- 1180 Dai, X., Zhu, M., Warren, M., Balakrishnan, R., Okano, H., Williamson, J. R., Fredrick, K., and Hwa, T. (2018). Slowdown of Translational Elongation in *Escherichia coli* under Hyperosmotic Stress. - PubMed - NCBI. *mBio*, 9(1):281.
- 1182 Dai, X., Zhu, M., Warren, M., Balakrishnan, R., Patsalo, V., Okano, H., Williamson, J. R., Fredrick, K., Wang, Y.-P., and Hwa, T. (2016). Reduction of translating ribosomes enables *Escherichia coli* to maintain elongation rates during slow growth. *Nature Microbiology*, 2(2):16231.
- 1185 Datsenko, K. A. and Wanner, B. L. (2000). One-step inactivation of chromosomal genes in *Escherichia coli* K-12 using PCR products. *Proceedings of the National Academy of Sciences*, 97(12):6640–6645.
- 1187 Dennis, P. P., Ehrenberg, M., and Bremer, H. (2004). Control of rRNA Synthesis in *Escherichia coli*: a Systems Biology Approach. *Microbiology and Molecular Biology Reviews*, 68(4):639–668.
- 1189 Dill, K. A., Ghosh, K., and Schmit, J. D. (2011). Physical limits of cells and proteomes. *Proceedings of the National Academy of Sciences*, 108(44):17876–17882.
- 1191 Erickson, D. W., Schink, S. J., Patsalo, V., Williamson, J. R., Gerland, U., and Hwa, T. (2017). A global resource allocation strategy governs growth transition kinetics of *Escherichia coli*. *Nature*, 551(7678):119–123.

- 1193 Escalante, A., Salinas Cervantes, A., Gosset, G., and Bolívar, F. (2012). Current knowledge of the *Escherichia coli* phosphoenolpyruvate-carbohydrate phosphotransferase system: Peculiarities of regulation and impact on growth and product formation. *Applied Microbiology and Biotechnology*, 94(6):1483–1494.
- 1196 Fernández-Coll, L., Maciąg-Dorszynska, M., Tailor, K., Vadia, S., Levin, P. A., Szalewska-Palasz, A., Cashel, M., and Dunny, G. M. (2020). The Absence of (p)ppGpp Renders Initiation of *Escherichia coli* Chromosomal DNA Synthesis Independent of Growth Rates. *mBio*, 11(2):45.
- 1199 Fijalkowska, I. J., Schaaper, R. M., and Jonczyk, P. (2012). DNA replication fidelity in *Escherichia coli*: A multi-DNA polymerase affair. *FEMS Microbiology Reviews*, 36(6):1105–1121.
- 1201 Finkelstein, I. J. and Greene, E. C. (2013). Molecular Traffic Jams on DNA. *Annual Review of Biophysics*, 42(1):241–263.
- 1202 Gallagher, L. A., Bailey, J., and Manoil, C. (2020). Ranking essential bacterial processes by speed of mutant death. *Proceedings of the National Academy of Sciences*.
- 1204 Gama-Castro, S., Salgado, H., Santos-Zavaleta, A., Ledezma-Tejeida, D., Muñiz-Rascado, L., García-Sotelo, J. S., Alquicira-Hernández, K., Martínez-Flores, I., Pannier, L., Castro-Mondragón, J. A., Medina-Rivera, A., Solano-Lira, H., Bonavides-Martínez, C., Pérez-Rueda, E., Alquicira-Hernández, S., Porrón-Sotelo, L., López-Fuentes, A., Hernández-Koutoucheva, A., Moral-Chávez, V. D., Rinaldi, F., and Collado-Vides, J. (2016). RegulonDB version 9.0: High-level integration of gene regulation, coexpression, motif clustering and beyond. *Nucleic Acids Research*, 44(D1):D133–D143.
- 1209 Godin, M., Delgado, F. F., Son, S., Grover, W. H., Bryan, A. K., Tzur, A., Jorgensen, P., Payer, K., Grossman, A. D., Kirschner, M. W., and Manalis, S. R. (2010). Using buoyant mass to measure the growth of single cells. *Nature Methods*, 7(5):387–390.
- 1211 Guo, Y., Li, D., Zhang, S., Yang, Y., Liu, J.-J., Wang, X., Liu, C., Milkie, D. E., Moore, R. P., Tulu, U. S., Kiehart, D. P., Hu, J., Lippincott-Schwartz, J., Betzig, E., and Li, D. (2018). Visualizing Intracellular Organelle and Cytoskeletal Interactions at Nanoscale Resolution on Millisecond Timescales. *Cell*, 175(5):1430–1442.e17.
- 1214 Harris, L. K. and Theriot, J. A. (2018). Surface Area to Volume Ratio: A Natural Variable for Bacterial Morphogenesis. *Trends in microbiology*, 26(10):815–832.
- 1216 Hauryliuk, V., Atkinson, G. C., Murakami, K. S., Tenson, T., and Gerdes, K. (2015). Recent functional insights into the role of (p)ppGpp in bacterial physiology. *Nature Reviews Microbiology*, 13(5):298–309.
- 1218 Heldal, M., Norland, S., and Tumyr, O. (1985). X-ray microanalytic method for measurement of dry matter and elemental content of individual bacteria. *Applied and Environmental Microbiology*, 50(5):1251–1257.
- 1220 Henkel, S. G., Beek, A. T., Steinsiek, S., Stagge, S., Bettenbrock, K., de Mattos, M. J. T., Sauter, T., Sawodny, O., and Ederer, M. (2014). Basic Regulatory Principles of *Escherichia coli*'s Electron Transport Chain for Varying Oxygen Conditions. *PLoS ONE*, 9(9):e107640.
- 1223 Hui, S., Silverman, J. M., Chen, S. S., Erickson, D. W., Basan, M., Wang, J., Hwa, T., and Williamson, J. R. (2015). Quantitative proteomic analysis reveals a simple strategy of global resource allocation in bacteria. *Molecular Systems Biology*, 11(2):e784–e784.
- 1226 Ingledew, W. J. and Poole, R. K. (1984). The respiratory chains of *Escherichia coli*. *Microbiological Reviews*, 48(3):222–271.
- 1227 Ireland, W. T., Beeler, S. M., Flores-Bautista, E., Belliveau, N. M., Sweredoski, M. J., Moradian, A., Kinney, J. B., and Phillips, R. (2020). Deciphering the regulatory genome of *Escherichia coli*, one hundred promoters at a time. *bioRxiv*.
- 1229 Jensen, R. B., Wang, S. C., and Shapiro, L. (2001). A moving DNA replication factory in *Caulobacter crescentus*. *The EMBO journal*, 20(17):4952–4963.
- 1231 Jun, S., Si, F., Pugatch, R., and Scott, M. (2018). Fundamental principles in bacterial physiology - history, recent progress, and the future with focus on cell size control: A review. *Reports on Progress in Physics*, 81(5):056601.
- 1233 Karp, P. D., Billington, R., Caspi, R., Fulcher, C. A., Latendresse, M., Kothari, A., Keseler, I. M., Krummenacker, M., Midford, P. E., Ong, Q., Ong, W. K., Paley, S. M., and Subhraveti, P. (2019). The BioCyc collection of microbial genomes and metabolic pathways. *Briefings in Bioinformatics*, 20(4):1085–1093.
- 1236 Karr, J. R., Sanghvi, J. C., Macklin, D. N., Gutschow, M. V., Jacobs, J. M., Bolival, B., Assad-Garcia, N., Glass, J. I., and Covert, M. W. (2012). A Whole-Cell Computational Model Predicts Phenotype from Genotype. *Cell*, 150(2):389–401.
- 1238 Keseler, I. M., Mackie, A., Santos-Zavaleta, A., Billington, R., Bonavides-Martínez, C., Caspi, R., Fulcher, C., Gama-Castro, S., Kothari, A., Krummenacker, M., Latendresse, M., Muñiz-Rascado, L., Ong, Q., Paley, S., Peralta-Gil, M., Subhraveti, P., Velázquez-Ramírez, D. A., Weaver, D., Collado-Vides, J., Paulsen, I., and Karp, P. D. (2017). The EcoCyc database: reflecting new knowledge about *Escherichia coli*K-12. *Nucleic Acids Research*, 45(D1):D543–D550.

- 1242 Khademian, M. and Imlay, J. A. (2017). *Escherichia coli* cytochrome c peroxidase is a respiratory oxidase that enables the use of  
1243 hydrogen peroxide as a terminal electron acceptor. *Proceedings of the National Academy of Sciences*, 114(33):E6922–E6931.
- 1244 Klumpp, S. and Hwa, T. (2014). Bacterial growth: Global effects on gene expression, growth feedback and proteome partition.  
1245 *Current Opinion in Biotechnology*, 28:96–102.
- 1246 Klumpp, S., Zhang, Z., and Hwa, T. (2009). Growth Rate-Dependent Global Effects on Gene Expression in Bacteria. *Cell*,  
1247 139(7):1366–1375.
- 1248 Kostinski, S. and Reuveni, S. (2020). Ribosome Composition Maximizes Cellular Growth Rates in *E. coli*. *Physical Review Letters*,  
1249 125(2):028103.
- 1250 Kraemer, J. A., Sanderlin, A. G., and Laub, M. T. (2019). The Stringent Response Inhibits DNA Replication Initiation in *E. coli* by  
1251 Modulating Supercoiling of oriC. *mBio*, 10(4):822.
- 1252 Lascu, I. and Gonin, P. (2000). The Catalytic Mechanism of Nucleoside Diphosphate Kinases. *Journal of Bioenergetics and Biomem-  
1253 branes*, 32(3):237–246.
- 1254 Laxhuber, K. S., Morrison, M. J., Chure, G., Belliveau, N. M., Strandkvist, C., Naughton, K. L., and Phillips, R. (2020). Theoretical  
1255 investigation of a genetic switch for metabolic adaptation. *PLOS ONE*, 15(5):e0226453.
- 1256 Lex, A., Gehlenborg, N., Strobelt, H., Vuillemot, R., and Pfister, H. (2014). UpSet: visualization of intersecting sets. *IEEE Transactions  
1257 on Visualization and Computer Graphics*, 20(12):1983–1992.
- 1258 Li, G.-W., Burkhardt, D., Gross, C., and Weissman, J. S. (2014). Quantifying absolute protein synthesis rates reveals principles  
1259 underlying allocation of cellular resources. *Cell*, 157(3):624–635.
- 1260 Liebermeister, W., Noor, E., Flamholz, A., Davidi, D., Bernhardt, J., and Milo, R. (2014). Visual account of protein investment in  
1261 cellular functions. *Proceedings of the National Academy of Sciences*, 111(23):8488–8493.
- 1262 Liu, M., Durfee, T., Cabrera, J. E., Zhao, K., Jin, D. J., and Blattner, F. R. (2005). Global Transcriptional Programs Reveal a Carbon  
1263 Source Foraging Strategy by *Escherichia coli*. *Journal of Biological Chemistry*, 280(16):15921–15927.
- 1264 Lu, D., Grayson, P., and Schulten, K. (2003). Glycerol Conductance and Physical Asymmetry of the *Escherichia coli* Glycerol Facili-  
1265 tator GlpF. *Biophysical Journal*, 85(5):2977–2987.
- 1266 Lynch, M. and Marinov, G. K. (2015). The bioenergetic costs of a gene. *Proceedings of the National Academy of Sciences*,  
1267 112(51):15690–15695.
- 1268 Maaløe, O. (1979). *Regulation of the Protein-Synthesizing Machinery—Ribosomes, tRNA, Factors, and So On*. Gene Expression.  
1269 Springer.
- 1270 Metzl-Raz, E., Kafri, M., Yaakov, G., Soifer, I., Gurvich, Y., and Barkai, N. (2017). Principles of cellular resource allocation revealed  
1271 by condition-dependent proteome profiling. *eLife*, 6:e03528.
- 1272 Mikucki, J. A., Pearson, A., Johnston, D. T., Turchyn, A. V., Farquhar, J., Schrag, D. P., Anbar, A. D., Priscu, J. C., and Lee, P. A. (2009).  
1273 A Contemporary Microbially Maintained Subglacial Ferrous "Ocean". *Science*, 324(5925):397–400.
- 1274 Milo, R., Jorgensen, P., Moran, U., Weber, G., and Springer, M. (2010). BioNumbers—the database of key numbers in molecular  
1275 and cell biology. *Nucleic Acids Research*, 38(suppl\_1):D750–D753.
- 1276 Monod, J. (1947). The phenomenon of enzymatic adaptation and its bearings on problems of genetics and cellular differentiation.  
1277 *Growth Symposium*, 9:223–289.
- 1278 Monod, J. (1949). The Growth of Bacterial Cultures. *Annual Review of Microbiology*, 3(1):371–394.
- 1279 Morgenstein, R. M., Bratton, B. P., Nguyen, J. P., Ouzounov, N., Shaevitz, J. W., and Gitai, Z. (2015). RodZ links MreB to cell wall  
1280 synthesis to mediate MreB rotation and robust morphogenesis. *Proceedings of the National Academy of Sciences*, 112(40):12510–  
1281 12515.
- 1282 Neidhardt, F. C., Ingraham, J., and Schaechter, M. (1991). *Physiology of the Bacterial Cell - A Molecular Approach*, volume 1. Elsevier.
- 1283 Ojkic, N., Serbanescu, D., and Banerjee, S. (2019). Surface-to-volume scaling and aspect ratio preservation in rod-shaped bacteria.  
1284 *eLife*, 8:642.
- 1285 Patrick, M., Dennis, P. P., Ehrenberg, M., and Bremer, H. (2015). Free RNA polymerase in *Escherichia coli*. *Biochimie*, 119:80–91.

- 1286 Peebo, K., Valgepea, K., Maser, A., Nahku, R., Adamberg, K., and Vilu, R. (2015). Proteome reallocation in *Escherichia coli* with  
1287 increasing specific growth rate. *Molecular BioSystems*, 11(4):1184–1193.
- 1288 Phillips, R. (2018). Membranes by the Numbers. In *Physics of Biological Membranes*, pages 73–105. Springer, Cham, Cham.
- 1289 Ranganathan, S., Tee, T. W., Chowdhury, A., Zomorodi, A. R., Yoon, J. M., Fu, Y., Shanks, J. V., and Maranas, C. D. (2012). An  
1290 integrated computational and experimental study for overproducing fatty acids in *Escherichia coli*. *Metabolic Engineering*,  
1291 14(6):687–704.
- 1292 Rogers, H., Perkins, H., and Ward, J. (1980). *Microbial Cell Walls and Membranes*. Chapman and Hall, London.
- 1293 Roller, B. R. K., Stoddard, S. F., and Schmidt, T. M. (2016). Exploiting rRNA operon copy number to investigate bacterial reproduc-  
1294 tive strategies. *Nature microbiology*, 1(11):1–7.
- 1295 Rosenberg, H., Gerdes, R. G., and Chegwidden, K. (1977). Two systems for the uptake of phosphate in *Escherichia coli*. *Journal of*  
1296 *Bacteriology*, 131(2):505–511.
- 1297 Ruppe, A. and Fox, J. M. (2018). Analysis of Interdependent Kinetic Controls of Fatty Acid Synthases. *ACS Catalysis*, 8(12):11722–  
1298 11734.
- 1299 Schaechter, M., Maaløe, O., and Kjeldgaard, N. O. (1958). Dependency on Medium and Temperature of Cell Size and Chemical  
1300 Composition during Balanced Growth of *Salmonella typhimurium*. *Microbiology*, 19(3):592–606.
- 1301 Schmidt, A., Kochanowski, K., Vedelaar, S., Ahrné, E., Volkmer, B., Callipo, L., Knoops, K., Bauer, M., Aebersold, R., and Heinemann,  
1302 M. (2016). The quantitative and condition-dependent *Escherichia coli* proteome. *Nature Biotechnology*, 34(1):104–110.
- 1303 Scott, M., Gunderson, C. W., Mateescu, E. M., Zhang, Z., and Hwa, T. (2010). Interdependence of cell growth and gene expression:  
1304 origins and consequences. *Science*, 330(6007):1099–1102.
- 1305 Shi, H., Bratton, B. P., Gitai, Z., and Huang, K. C. (2018). How to Build a Bacterial Cell: MreB as the Foreman of *E. coli* Construction.  
1306 *Cell*, 172(6):1294–1305.
- 1307 Si, F., Le Treut, G., Sauls, J. T., Vadia, S., Levin, P. A., and Jun, S. (2019). Mechanistic Origin of Cell-Size Control and Homeostasis in  
1308 Bacteria. *Current Biology*, 29(11):1760–1770.e7.
- 1309 Si, F., Li, D., Cox, S. E., Sauls, J. T., Azizi, O., Sou, C., Schwartz, A. B., Erickstad, M. J., Jun, Y., Li, X., and Jun, S. (2017). Invariance of  
1310 Initiation Mass and Predictability of Cell Size in *Escherichia coli*. *Current Biology*, 27(9):1278–1287.
- 1311 Sohlenkamp, C. and Geiger, O. (2016). Bacterial membrane lipids: Diversity in structures and pathways. *FEMS Microbiology*  
1312 *Reviews*, 40(1):133–159.
- 1313 Soufi, B., Krug, K., Harst, A., and Macek, B. (2015). Characterization of the *E. coli* proteome and its modifications during growth  
1314 and ethanol stress. *Frontiers in Microbiology*, 6:198.
- 1315 Stasi, R., Neves, H. I., and Spira, B. (2019). Phosphate uptake by the phosphonate transport system PhnCDE. *BMC Microbiology*,  
1316 19.
- 1317 Stouthamer, A. H. (1973). A theoretical study on the amount of ATP required for synthesis of microbial cell material. *Antonie van*  
1318 *Leeuwenhoek*, 39(1):545–565.
- 1319 Stouthamer, A. H. and Bettenhausen, C. W. (1977). A continuous culture study of an ATPase-negative mutant of *Escherichia coli*.  
1320 *Archives of Microbiology*, 113(3):185–189.
- 1321 Szenk, M., Dill, K. A., and de Graff, A. M. R. (2017). Why Do Fast-Growing Bacteria Enter Overflow Metabolism? Testing the  
1322 Membrane Real Estate Hypothesis. *Cell Systems*, 5(2):95–104.
- 1323 Taheri-Araghi, S., Bradde, S., Sauls, J. T., Hill, N. S., Levin, P. A., Paulsson, J., Vergassola, M., and Jun, S. (2015). Cell-size control  
1324 and homeostasis in bacteria. - PubMed - NCBI. *Current Biology*, 25(3):385–391.
- 1325 Taniguchi, Y., Choi, P. J., Li, G.-W., Chen, H., Babu, M., Hearn, J., Emili, A., and Xie, X. S. (2010). Quantifying *E. coli* proteome and  
1326 transcriptome with single-molecule sensitivity in single cells. *Science (New York, N.Y.)*, 329(5991):533–538.
- 1327 Tatusov, R. L., Galperin, M. Y., Natale, D. A., and Koonin, E. V. (2000). The COG database: a tool for genome-scale analysis of  
1328 protein functions and evolution. *Nucleic Acids Research*, 28(1):33–36.
- 1329 Taymaz-Nikerel, H., Borujeni, A. E., Verheijen, P. J. T., Heijnen, J. J., and van Gulik, W. M. (2010). Genome-derived minimal metabolic  
1330 models for *Escherichia coli* mg1655 with estimated in vivo respiratory ATP stoichiometry. *Biotechnology and Bioengineering*,  
1331 107(2):369–381. \_eprint: <https://onlinelibrary.wiley.com/doi/10.1002/bit.22802>.

- <sup>1332</sup> The Gene Ontology Consortium (2018). The Gene Ontology Resource: 20 years and still GOing strong. *Nucleic Acids Research*,  
<sup>1333</sup> 47(D1):D330–D338.
- <sup>1334</sup> Valgepea, K., Adamberg, K., Seiman, A., and Vilu, R. (2013). *Escherichia coli* achieves faster growth by increasing catalytic and  
<sup>1335</sup> translation rates of proteins. *Molecular BioSystems*, 9(9):2344.
- <sup>1336</sup> Virtanen, P., Gommers, R., Oliphant, T. E., Haberland, M., Reddy, T., Cournapeau, D., Burovski, E., Peterson, P., Weckesser, W.,  
<sup>1337</sup> Bright, J., van der Walt, S. J., Brett, M., Wilson, J., Jarrod Millman, K., Mayorov, N., Nelson, A. R. J., Jones, E., Kern, R., Larson,  
<sup>1338</sup> E., Carey, C., Polat, İ., Feng, Y., Moore, E. W., Vand erPlas, J., Laxalde, D., Perktold, J., Cimrman, R., Henriksen, I., Quintero,  
<sup>1339</sup> E. A., Harris, C. R., Archibald, A. M., Ribeiro, A. H., Pedregosa, F., van Mulbregt, P., and Contributors, S. . . (2020). SciPy 1.0:  
<sup>1340</sup> Fundamental Algorithms for Scientific Computing in Python. *Nature Methods*, 17:261–272.
- <sup>1341</sup> Volkmer, B. and Heinemann, M. (2011). Condition-Dependent Cell Volume and Concentration of *Escherichia coli* to Facilitate  
<sup>1342</sup> Data Conversion for Systems Biology Modeling. *PLOS ONE*, 6(7):e23126.
- <sup>1343</sup> Vollmer, W., Blanot, D., and De Pedro, M. A. (2008). Peptidoglycan structure and architecture. *FEMS Microbiology Reviews*,  
<sup>1344</sup> 32(2):149–167.
- <sup>1345</sup> Weber, J. and Senior, A. E. (2003). ATP synthesis driven by proton transport in F1F0-ATP synthase. *FEBS Letters*, 545(1):61–70.
- <sup>1346</sup> Willsky, G. R., Bennett, R. L., and Malamy, M. H. (1973). Inorganic Phosphate Transport in *Escherichia coli*: Involvement of Two  
<sup>1347</sup> Genes Which Play a Role in Alkaline Phosphatase Regulation. *Journal of Bacteriology*, 113(2):529–539.
- <sup>1348</sup> You, C., Okano, H., Hui, S., Zhang, Z., Kim, M., Gunderson, C. W., Wang, Y.-P., Lenz, P., Yan, D., and Hwa, T. (2013). Coordination  
<sup>1349</sup> of bacterial proteome with metabolism by cyclic AMP signalling. *Nature*, 500(7462):301–306.
- <sup>1350</sup> Yu, X., Liu, T., Zhu, F., and Khosla, C. (2011). In vitro reconstitution and steady-state analysis of the fatty acid synthase from  
<sup>1351</sup> *Escherichia coli*. *Proceedings of the National Academy of Sciences*, 108(46):18643–18648.
- <sup>1352</sup> Zhang, Z., Aboulwafa, M., and Saier, M. H. (2014). Regulation of crp gene expression by the catabolite repressor/activator, cra,  
<sup>1353</sup> in *Escherichia coli*. *Journal of Molecular Microbiology and Biotechnology*, 24(3):135–141.
- <sup>1354</sup> Zhu, M. and Dai, X. (2019). Growth suppression by altered (p)ppGpp levels results from non-optimal resource allocation in  
<sup>1355</sup> *Escherichia coli*. *Nucleic Acids Research*, 47(9):4684–4693.

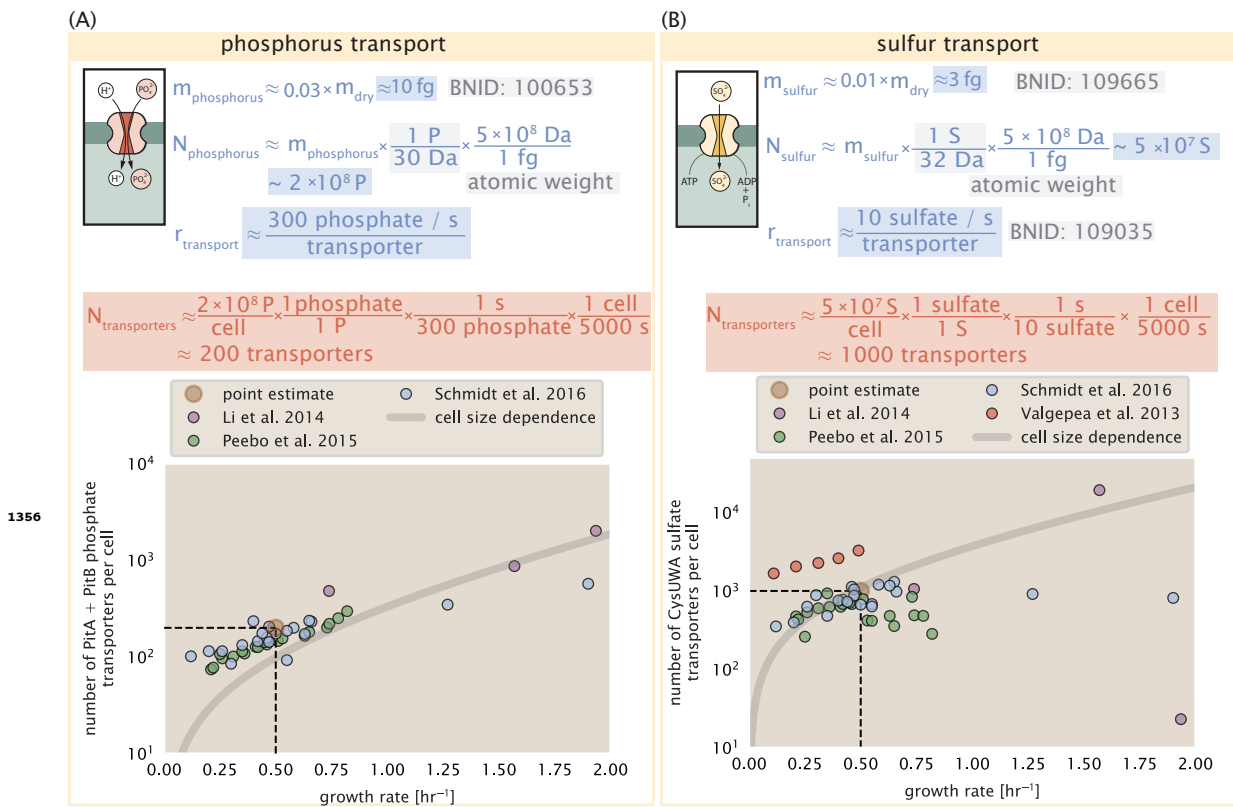


**Figure 2-Figure supplement 1.** (A) Estimate for the number of PitA phosphate transport systems needed to maintain a 3% phosphorus *E. coli* dry mass. Points in plot correspond to the total number of PitA transporters per cell. (B) Estimate of the number of CysUWA complexes necessary to maintain a 1% sulfur *E. coli* dry mass. Points in plot correspond to average number of CysUWA transporter complexes that can be formed given the transporter stoichiometry [CysA]<sub>2</sub>[CysU][CysW][Sbp/CysP]. Grey line in (A) and (B) represents the estimated number of transporters per cell at a continuum of growth rates.

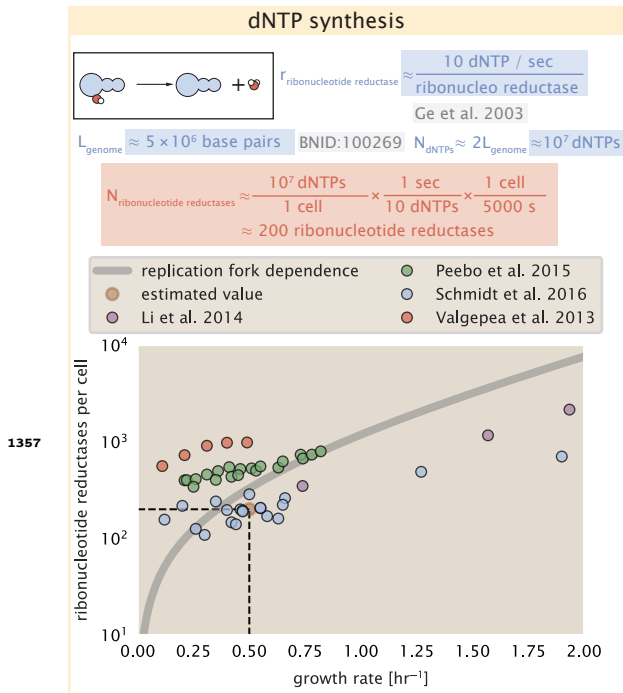


**Figure 6–Figure supplement 1.** Estimate of the number of ribonucleotide reductase enzymes needed to facilitate the synthesis of  $\approx 10^7$  dNTPs over the course of a 5000 second generation time. Points in the plot correspond to the total number of ribonucleotide reductase I ( $[\text{NrdA}]_2[\text{NrdB}]_2$ ) and ribonucleotide reductase II ( $[\text{NrdE}]_2[\text{NrdF}]_2$ ) complexes. Grey lines in top panel show the estimated number of complexes needed as a function of growth, the details of which are described in the Appendix.

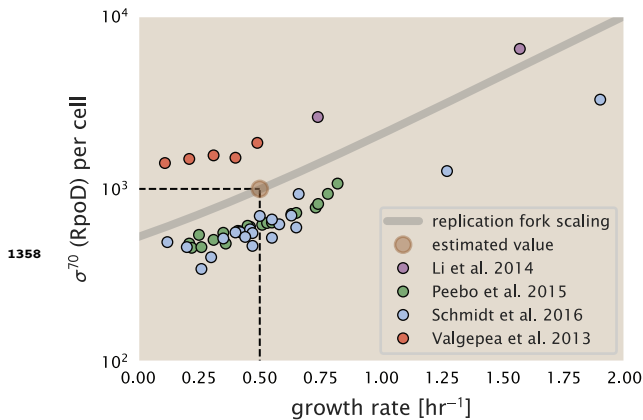


**Figure 7–Figure supplement 1.** The abundance of  $\sigma^{70}$  as a function of growth rate. Estimated value for the number of RNAP is shown as a translucent brown point and grey line.

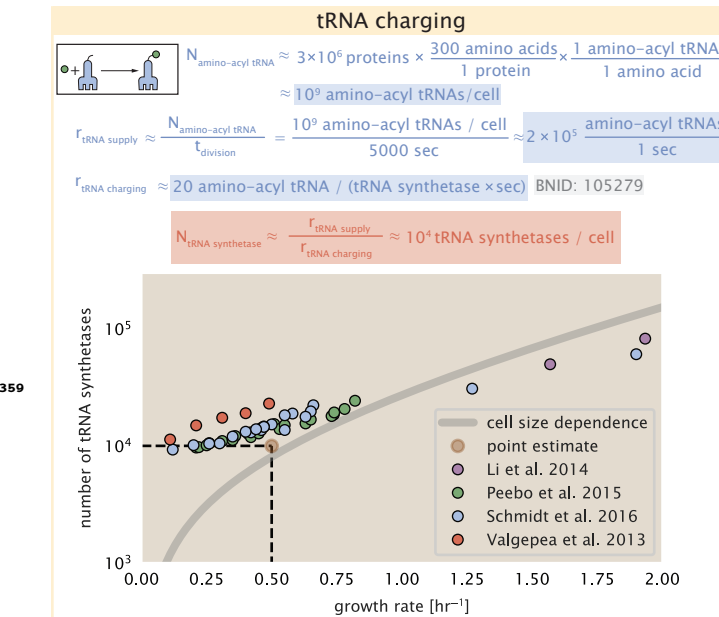


**Figure 8-Figure supplement 1.** Estimation for the number of tRNA synthetases that will supply the required amino acid demand. The sum of all tRNA synthetases copy numbers are plotted as a function of growth rate ([ArgS], [CysS], [GlnS], [GltX], [IleS], [LeuS], [ValS], [AlaS]<sub>2</sub>, [AsnS]<sub>2</sub>, [AspS]<sub>2</sub>, [TyrS]<sub>2</sub>, [TrpS]<sub>2</sub>, [ThrS]<sub>2</sub>, [SerS]<sub>2</sub>, [ProS]<sub>2</sub>, [PheS]<sub>2</sub>[PheT]<sub>2</sub>, [MetG]<sub>2</sub>, [lysS]<sub>2</sub>, [HisS]<sub>2</sub>, [GlyS]<sub>2</sub>[GlyQ]<sub>2</sub>).

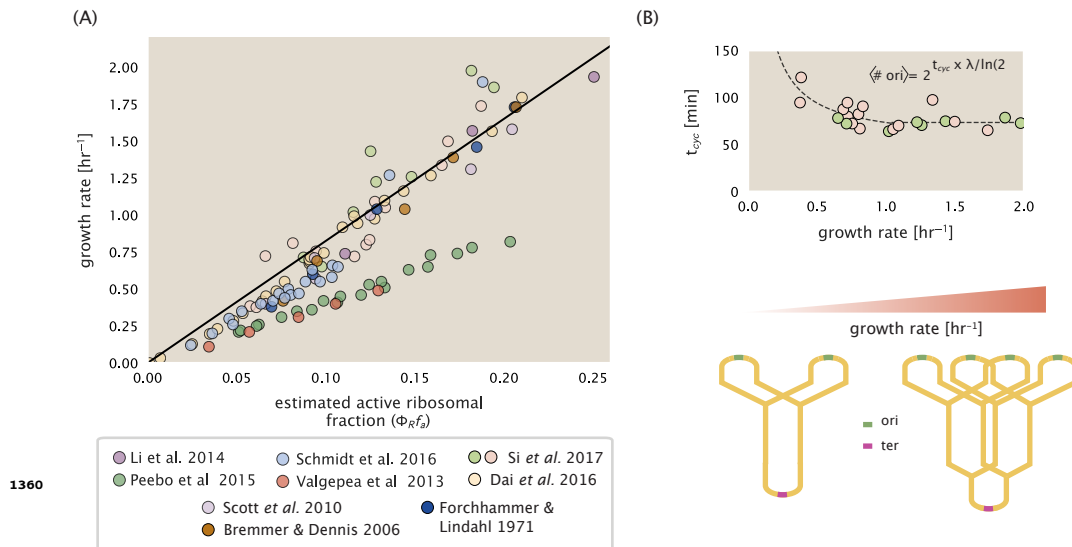


**Figure 9-Figure supplement 1.** (A) Actively translating ribosomal fraction versus growth rate. The actively translating ribosomal fraction is calculated using the estimated values of  $f_a$  from [Dai et al. \(2016\)](#) (shown in inset; see Appendix Calculation of active ribosomal fraction for additional detail). Additional measurements in addition to the proteomic measurements are based on measurements of cellular RNA to protein ratio, with  $\Phi_R \approx$  the cellular RNA to protein ratio divided by 2.1 ([Dai et al., 2016](#)). (B) Experimental measurements of the cell doubling time  $\tau$  and cell cycle time  $t_{\text{cyc}}$  from [Si et al. \(2017\)](#). Dashed line shows fit to the data, which were used to estimate  $\langle \# \text{ori} \rangle$ .  $t_{\text{cyc}}$  was assumed to vary in proportion to  $\tau$  for doubling times greater than 40 minutes, and reach a minimum value of 73 minutes. See Appendix Estimation of  $\langle \# \text{ori} \rangle / \langle \# \text{ter} \rangle$  and  $\langle \# \text{ori} \rangle$  for additional details exact estimation of rRNA copy number. Red data points correspond to measurements in strain MG1655, while light green points are for strain NCM3722. Schematic shows the expected increase in replication forks (or number of ori regions) as *E. coli* cells grow faster.